

# Master thesis

on

## Simulation of temperature and dose distribution of a proposed minimally invasive treatment of early-stage breast cancer by combining thermal ablation and LDR brachytherapy using $^{103}\text{Pd}$ -SPIO nanoparticles

### Final report

Modelling of a newly proposed minimally invasive therapy for early-stage breast cancer to gain more knowledge of the behaviour of the treatment material in tissue. The simulations to investigate the effectiveness and limitations of the combined therapy allowed for the prediction of the treatment results, by calculating the temperature distribution and dose distribution over time. The sensitivity of the results to the relevant variables was analyzed, resulting in a recommended optimization approach for treatment planning.

Keywords: Proposed combined single interference treatment; thermal ablation; LDR brachytherapy; early-stage breast cancer; thermo-radioactive nanoparticles; Palladium-103 superparamagnetic iron-oxide nanoparticles; Finite Element Method; Matlab simulations; temperature, concentration and dose distribution profiles; sensitivity analysis; treatment optimization

by

E.W.E. van Krimpen 4448782

#### Thesis committee

Dr. Z. Perko	Associate Professor
Dr. ir. A.G. Denkova	Associate Professor
Dr. K. Djanashvili	Associate Professor
Dr. ir. M.C. Goorden	Assistant Professor
Dr. ir. D. Lathouwers	Associate Professor

#### Additional supervisor

R. van Oossanen	PhD candidate
-----------------	---------------

#### MSc Chemical Engineering

ChemE - Faculty of Applied Sciences  
Delft University of Technology

Start project: 14-02-2022

Report issued: 23-09-2022

Defense date: 06-10-2022



# Abstract

Treatment of early stage breast cancer is generally invasive to a patient's daily life while being treated. Therefore, to diminish the physical and psychological impact during and after recovery, a newly proposed minimally invasive therapy for early-stage breast cancer treatment is proposed. Within this study, this proposed treatment is modelled to gain more knowledge of the behaviour of the treatment material in tissue. The treatment includes magnetic thermal ablation, which is combined with permanent Low Dose Rate brachytherapy, both performed simultaneously. The goal of the treatment is to diminish the physical and psychological impact during treatment and after recovery, since it requires only a single medical intervention. The treatment material consists of radioactive palladium-103 superparamagnetic iron-oxide nanoparticles ( $^{103}\text{Pd}$  SPIONs) incorporated in a solid gel, forming a seed that is implanted into the tumor. To investigate the effectiveness and limitations of the combined therapy, computational simulations were performed in Matlab using the Finite Element Method (FEM). These simulations allowed for the prediction of the treatment results, by calculating the temperature distribution based on Pennes' bioheat equation, the nanoparticle concentration distribution and the dose distribution over time. The sensitivity of the results to the relevant physical properties and optimization parameters was analyzed. The latter resulted in a recommended optimization approach that ultimately could be used for treatment planning. First, an initial simulation was performed using property values from literature. Then, the temperature and dose results were tested on their sensitivity to model parameter changes. The temperature model was found to be most sensitive to changes in the nanoparticle heat source value  $Q_{NP}$ , to an increased heat conduction coefficient  $k$  and to a decreased blood perfusion rate  $\omega_b$ . The cumulative dose results are sensitive to both the initial concentration  $c_i$  and to a decreased diffusion coefficient  $D$ . It is concluded that accurate values for these temperature and concentration model parameters are necessary to perform relevant simulations. Furthermore, the possible optimization parameters were identified. For dose optimization, these parameters are the activity of the nanoparticles  $A$ , which is not easily modified, and the initial nanoparticle concentration in the seeds  $c_i$ , which affects the temperature distribution as well. The temperature distribution specific variables that were found, are the strength of the magnetic field  $H$  and the time  $t$  of magnetic field application, which both can be adjusted during the treatment. The seed location and number of seeds are two additional adjustable variables used for optimization of both temperature and dose distribution. Lastly, it was concluded that the internal radiation part of the treatment is limiting in the reaching treatment goals and in number of optimization possibilities, compared to the thermal ablation part. Therefore, treatment optimization should be performed on the dose distribution first. Because most limitations of the models are a result of the 2D representation and because these limitations strongly affect the outcomes of the models, it is recommended to transform these models to 3D. These limitations make it impossible to do proper treatment planning with the 2D model, which requires a 3D view of the results. With all these findings, this study has contributed by providing basic knowledge of the state-of-the-art early stage breast cancer combined therapy, bringing it one step closer to clinical implementation.

# Acknowledgments

It can be said that during my master thesis project, I have gained a lot of knowledge and skills, especially in the computational field. Despite the little experience I had with modeling, I got the chance to improve that skill greatly. However, I do not think my supervisors expected my computational knowledge to be this little, when agreeing to let me work on the project. I remember that during one of the first meetings I encountered a problem with my script, thinking it was 'broken' since it took longer than two minutes to run. Starting from that bottom line, I at least did not think I would be able to finish my project with what it is now. I am very glad that I got the chance to do this project and that I have been able to lose myself in a scientific field that kept exciting me every day.

Firstly, I would like to greatly thank dr. Zoltan Perkó for being my supervisor, as he is a supervisor I would wish for everyone to have. He has guided me through the project with a lot of patience, enthusiasm and time. The clear expectations set at the beginning gave a kick start to my project. Also, his limitless knowledge not only helped me with the content of my project, but helped me with understanding the real meaning of scientific thinking. The feedback was always helpful and constructive, while not holding a compliment if he had one. I have learned that this way of supervision really fits my way of working. I felt confident at the end of every meeting, even though I was left with a list of things to do I felt were impossible. If there is one thing that I learned during my thesis, it is that if you can think of it, you can model it.

Secondly, a big thanks to Rogier Oossanen, for always taking the time to help me. Also, I really appreciated him for helping not only with subject related questions, but also for advising me on how to manage my project in general and on my future plans. His enthusiasm inspired me, from brewing his own beer to doing research in the medical field. I hope to have contributed a little to his research too, as he contributed to mine greatly. I also want to thank dr. Kristina Djanashvili and dr. Antonia Denkova for their sharp questions and ability to interpret my results on a different level.

Lastly, I need to thank my friends and family for listening to my endless bursts of enthusiasm for the subject and my project. Especially those who simply got with me on my train of thoughts if I was stuck on it and was not able to get off before lunch or dinner. I had a great time doing my thesis and I hope my work not only contributed in finishing my masters degree, but also contributed slightly with the outcomes to the knowledge of the proposed treatment.

# Contents

<b>List of Figures</b>	<b>1</b>
<b>List of Tables</b>	<b>4</b>
<b>1 Introduction</b>	<b>5</b>
<b>2 Background Information</b>	<b>7</b>
2.1 Early Stage Breast Cancer . . . . .	7
2.2 Tumor Tissue and Structure . . . . .	8
2.3 Breast Cancer Treatments . . . . .	9
2.3.1 Thermal Ablation . . . . .	9
2.3.2 Brachytherapy . . . . .	9
2.4 Proposed Multi-Modal Thermal Brachytherapy . . . . .	10
2.4.1 Thermo- and Radioactive Nanoparticles . . . . .	11
2.4.2 Treatment Procedure . . . . .	12
2.5 Physical Processes Underlying the Proposed Treatment . . . . .	13
2.5.1 Heat Transfer in Tissue . . . . .	13
2.5.2 Nanoparticle Transport in Tissue . . . . .	15
2.5.3 Radiation Transport in Tissue . . . . .	16
<b>3 Methodology</b>	<b>18</b>
3.1 Finite Element Method as Numerical Approach . . . . .	18
3.2 Main Simulation Steps of Built Models . . . . .	20
3.2.1 Defining Geometry and Subdomains . . . . .	20
3.2.2 Temperature Distribution Calculation . . . . .	22
3.2.3 Nanoparticle Concentration Distribution Calculation . . . . .	23
3.2.4 Dose calculation . . . . .	24
3.3 Physical Properties and Variables . . . . .	25
<b>4 Results and Discussion</b>	<b>26</b>
4.1 Reference Results using Default Parameters . . . . .	27
4.1.1 Default Temperature Distribution . . . . .	27
4.1.2 Default Cumulative Delivered Dose Distribution . . . . .	27
4.2 Sensitivity Analysis . . . . .	29
4.2.1 Sensitivity of Temperature to Model Parameters . . . . .	29
4.2.2 Sensitivity of Concentration and Dose Results to Model Parameters . . . . .	35
4.2.3 Sensitivity of Temperature and Dose to Optimization Variables . . . . .	38
4.3 Treatment Planning Optimization . . . . .	39
4.4 Critical Notes . . . . .	40
<b>Conclusion and Further Recommendations</b>	<b>42</b>
<b>List of Abbreviations</b>	<b>43</b>
<b>Reference list</b>	<b>45</b>
<b>Appendices</b>	
<b>A Minima, Maxima of Parameters and Model Variables</b>	<b>i</b>
<b>B Additional Temperature Model Results</b>	<b>ii</b>
<b>C Concentration Model Results</b>	<b>iii</b>

# List of Figures

2.1	Anatomy of the female breast: front (left) and side (right) view. . . . .	7
2.2	Schematic image of IDC cancer, the most common breast cancer type. It shows DCIS being a precursor to IDC [1]. . . . .	8
2.3	Schematic overview of the different tumor volumes that are identified during treatment planning. It includes the Gross Tumor Volume (GTV), the Clinical Target Volume (CTV) and the Planning Target Volume (PTV). . . . .	8
2.4	Schematic overview of therapies of interest. These are the therapies on which the newly proposed therapy is based. . . . .	9
2.5	Schematic overview of the result of the newly proposed thermo-brachytherapy. First, the magnetic field heats up the nanoparticles that burn the core of the tumor, followed by irradiation by the nanoparticles to the outskirts of the tumor. . . . .	10
2.6	Overview of the composition of Pd-103 superparamagnetic iron oxide nanoparticles and the seeds they are incorporated in. The nanoparticles consist of multiple layers, namely: 1. Radioactive Pd-103 core; 2. Thermoactive SPIO layer; 3. Silica layer for biocompatibility and leak prevention. These nanoparticles are incorporated in a solid gel, forming the brachyseeds that are injected into the tumor. . . . .	11
2.7	Overview of the proposed therapy from the diagnosis of the sick patient to the end of the therapy. The treatment timeline is visible at the bottom, showing that the two thermal ablation (orange) and the radiation (green) happen simultaneously at the start. It is also visible that after the alternating magnetic field is switched off no more medical intervention is required. . . . .	12
2.8	This graph shows three different relations between the relative blood perfusion rate and the tissue temperature. The red line represents the constant blood perfusion rate assumed in Pennes' bioheat equation (Equation 2.2). The green line shows the relation where blood perfusion decreases linearly to zero above $T_{cr}$ (2.4). The black line gives the relation where the blood perfusion rate increases for $T < T_{critical}$ and decrease above $T_{critical}$ (2.5) [2]. The blood perfusion rate is described as the relative difference between the proposed blood perfusion rate compared to the initial blood perfusion rate $\omega_{bi}$ . . . . .	14
2.9	The radial dose distribution of combined radiation of a single nanoparticle with a 5 nm palladium core and 20 nm iron oxide shell. It uses the simulated results of the energy spectra of the electrons and photons leaving the nanoparticle. On the y-axis the relative delivered dose rate $\dot{D}_{ij}$ by $\sim 100.000$ Palladium-103 decays per hour is given for different distances from the centre of the nanoparticle $r_{ij}$ [3]. . . . .	17
3.1	Block scheme of the Finite Element Method. It shows on the left the variables that are required input to solve the problem. On the right hand side it is shown that the results are the output of the solved problem. . . . .	18
3.2	General overview of the process steps of the built temperature and concentration models. The phases are based on the required steps for the FEM approach described in Section 3.1. . . . .	18
3.3	One dimensional representation of a test function $\phi_i$ , showing it has a non-zero value at $x_i$ , resulting in a linear relation over $x$ between $x_{i-1}$ and $x_{i+1}$ . . . . .	19
3.4	Overview of different geometries of a breast with in 3D, 2D and a cut-out of the 2D geometry. Also the discretized mesh of the geometry in 3.4c is given. . . . .	20
3.5	(a) The brachytherapy template is used for implantation of the seeds. The grid of holes determine the seed locations in X and Z directions. The seeds are implanted within the tumor with needles that fit the holes in the template. (b) A nanoparticle seed including XZ and YZ planes; (c) The nanoparticle seed including its sizes in diameter and length. . . . .	21
3.6	Default seed locations for (a) the XZ plane and (b) the YZ plane in 2D. (c) The 3D seed locations in a spherical tumor. The seeds are positioned inside the GTV (smallest circle), which is surrounded by the PTV (larger circle) and the breast tissue. . . . .	21
3.7	Voxelized 2D dose rate distribution of a single nanoparticle. Based on the radial dose distribution in Figure 2.9, which is first interpolated to 2D and then converted into a voxel mesh grid of size 0.05 by 0.05 cm. . . . .	24
4.1	Temperature results of default settings. Temperature distribution profiles after 20 minutes (a) in XZ direction and (b) YZ direction. (c) Temperature intersection profile through the centre of the tumor, for the XZ (blue) and YZ (orange) planes. The vertical lines indicate the outer shell of the GTV and PTV. The dotted horizontal lines indicate the limits to fulfill the treatment requirements. (d) Maximum, minimum and average temperatures in the GTV over time for both XZ and YZ planes. . . . .	26

4.2	Cumulative dose results of default settings. Dose distribution profiles after 85 days (a) in XZ direction and (b) YZ direction. (c) Cumulative dose intersection profile through the centre of the tumor, for the XZ (blue) and YZ (orange) planes. The vertical lines indicate the outer shell of the GTV and PTV. The dotted horizontal line indicates the minimum required dose inside the PTV and the maximum dose outside the PTV. (d) Maximum, minimum and average dose in the GTV over time for both XZ and YZ planes. The maximum dose represents the centre seed, the minimum the edge of the GTV furthest away from a seed and the average is taken over the whole GTV. . . . .	28
4.3	Temperature profiles in XZ plane after 20 minutes of all tested necrotic core diameters (0 cm, 1 cm, 2 cm, 3 cm and 4 cm). The colormap axis is the same for all diameters, its maximum being equal to the maximum temperature reached for a necrotic core of 4 cm diameter (119°C). The profiles show that the profiles differ and also the temperatures reached are higher, due to a lack of blood perfusion. . . . .	30
4.4	Temperature over time for different necrotic core diameters, being 0 cm, 1 cm, 2 cm, 3 cm and 4 cm. A larger necrotic core means a larger part of the tumor without blood perfusion and thus leads to a higher temperature and wider spread. . . . .	30
4.5	The vertical lines indicate the outer shell of the GTV and PTV. (a) Overview of the intersection through the centre of the tumor for different necrotic core diameters (0 cm, 1 cm, 2 cm, 3 cm and 4 cm) after 20 minutes. It shows that higher temperatures are reached in the necrotic areas, where no heat is removed. (b) Overview of the intersection through the centre of the tumor for different blood perfusion relations. The linear relation (Equation 2.4; blue) and scaling function (Equation 2.5; yellow) give the same results. The default blood perfusion relation is constant (Equation 2.3; red) . . . . .	31
4.6	Temperature over time for different blood perfusion relations: constant (blue), linear (red) and scaling function $F(T)$ (yellow). The temperature increases more strongly for the linear and $F(T)$ functions, because after reaching 48°C there is no more blood perfusion. Also, after the AMF is switched off at $t = 20$ min, the temperature decreases more slowly, because no heat is removed in the areas that have been heated above 48°C. . . . .	31
4.7	(a) Temperature over time for different blood perfusion rates: minimum (red), default (blue) and maximum (yellow). For a smaller blood perfusion rate, higher temperatures are reached. Also, the temperature is removed slower from the system with smaller blood perfusion. (b) The investigated relation between temperature and blood perfusion rate suggests an exponential relation, where the maximum temperature decreases with increasing blood perfusion rate. The blood perfusion rate is assumed constant over temperature and time. . . . .	32
4.8	(a) Intersection through the centre of the tumor for different blood perfusion rates after 20 minutes of heating, showing wider temperature distribution for smaller blood perfusion rate. (b) Intersection through the centre of the tumor of different heat conduction rates. A smaller heat conduction coefficient means slower spread of heat. It results in higher local temperatures and a smaller distribution. . . . .	33
4.9	Temperature over time for different heat conduction coefficients. A larger heat conduction coefficient leads to lower maximum temperatures and faster removal and results in a wider spread of heat, and thus a higher minimum temperature in the GTV. . . . .	33
4.10	Different $Q_{NP}$ values: minimum (blue), default (red) and maximum (yellow). A higher $Q_{NP}$ leads to higher temperatures, with no change in profile. . . . .	34
4.11	Intersection through the centre of the tumor after 17 days for different initial nanoparticle concentrations in the seeds. It shows a higher overall dose for higher initial concentration with no change in distribution. The tested initial concentrations were increased with a factor $10^2$ . This exact difference is visible in the intersection graph. . . . .	35
4.12	Dose distribution profiles in XZ plane after 17 days for different initial nanoparticle concentrations. The profiles show that the dose increases with increasing concentration, while the relative dose distribution remains the same. . . . .	36
4.13	Concentration of nanoparticles over time for different initial concentration in the seeds: minimum (blue), default (red) and maximum (yellow). A higher initial condition leads to a higher concentration and thus a higher dose. The relation is linear and does not influence the dose distribution. . . . .	36
4.14	Effect of different diffusion coefficients: minimum (blue), default (red), maximum (yellow) and $D$ is zero (green). (a) Intersection through the centre of the tumor after 17 days for different diffusion coefficients with logarithmic axis representing the cumulative dose; (b) Maximum dose over time; (c) Maximum dose over time. Higher diffusion coefficient leads to faster spread of nanoparticles through tissue, resulting in lower overall dose, but wider distribution. . . . .	37
4.15	Dose distribution profiles in XZ plane after 17 days for different diffusion coefficients. The profiles show that the distributions differ strongly, especially for large $D$ . . . . .	37
4.16	Temperature over time for different AMF times. The temperatures increase when the AMF is switched on for a longer time. . . . .	38

B.1	Intersection through the centre of the tumor. Temperature taken over time right after switching off the AMF, showing that the temperature gradient between the centre seed and its neighbours decreases over time, resulting in a parabolic temperature distribution. . . . .	ii
C.1	Nanoparticle concentration results of default settings. Concentration profiles after 17 days (a) in XZ direction and (b) YZ direction. (c) Cumulative dose intersection profile through the centre of the tumor, for the XZ (blue) and YZ (orange) planes. The vertical lines indicate the outer shell of the GTV and PTV. (d) Maximum, minimum and average concentration in the GTV over time for both XZ and YZ planes. The maximum concentration represents the centre seed, the minimum the edge of the GTV furthest away from a seed and the average is taken over the whole GTV. . . . .	iii
C.2	Nanoparticle concentration distribution after 60 minutes. The NP concentration profile after 60 minutes shows a similar distribution as the profile at $t = 0$ minutes. This suggests that the NP diffusion can be neglected for the thermal ablation part of the treatment. . . . .	iii
C.3	Concentration and dose distribution profiles resulting from a diffusion coefficient of 0. If the NPs are unable to diffuse through the tumor tissue, the radioactive NPs still deliver radioactive dose to the tissue. . . . .	iii

# List of Tables

3.1	Default parameter values for temperature model. All parameters extracted from temperature properties review executed by Camilleri <i>et al.</i> [4]. Specific absorption rate, concentration fraction and nanoparticle heat source determined during project execution. . . . .	25
3.2	Default parameter values for concentration model . . . . .	25
4.1	Results of default coefficients and parameters for temperature at t = 20 min and delivered dose at t = 85 days. It gives the maximum, average and minimum values of the parameters of interest within the GTV, PTV area around the GTV and the area of 1 cm outside the PTV. . . . .	29
4.2	Temperature results of sensitivity analysis of parameters evaluated using minimum, default and maximum values. For each parameter the maximum, minimum and average concentrations are found for the GTV, PTV area around the GTV and the area of 1 cm outside the PTV. [2, 4] . . . . .	34
4.3	Sensitivity index of every parameter in the temperature model. It shows the relation between the tested parameter and the effect on the minimum temperature in the GTV (left) and the maximum temperature in the area surrounding the PTV (right). These temperatures are the values of interest to check whether the temperature requirements are met. The parameters are ranked from large impact to small impact. . . . .	35
4.4	Concentration results of sensitivity analysis of parameters evaluated using minimum, default and maximum values. For each parameter the maximum, minimum and average cumulative dose is found for the GTV, PTV area around the GTV and the area of 1 cm outside the PTV. [5, 6] . . . . .	37
4.5	Sensitivity index of every parameter in the concentration model to the cumulative delivered dose distribution. It shows the relation between the tested parameter and the effect on the minimum dose in the PTV and the maximum dose in the area surrounding the PTV. These delivered doses are the values of interest to check whether the delivered cumulative dose requirements are met. The parameters are ranked from large impact to small impact for both results of interest separately. . . . .	38
4.6	Sensitivity index of adjustable variables for treatment optimization. It shows that only two variables influence the dose, with the same sensitivity index, and three variables affect the temperature. The nanoparticle concentration affects both temperature and dose distribution. . . . .	39
4.7	Overview of the possible solutions to tackle a specific optimization problem in an attempt to meet the requirements. It also describes the consequences of the solution to the results it affects. . . . .	40
A.1	Minimum and maximum values used during sensitivity analysis for parameters of temperature model. Values for bloodperfusion rate and conduction rate extracted from temperature properties review executed by Camilleri <i>et al.</i> [4] Other variables determined during project execution. . . . .	i
A.2	Minimum and maximum values used during sensitivity analysis for parameters of concentration model. Diffusion coefficient range found in literature [5, 6] and initial concentration is determined within project. . . . .	i
A.3	Table includes the model specific variables that are used in both temperature and concentration PDE solving models. . . . .	ii
C.1	Concentration results of sensitivity analysis of parameters evaluated using minimum, default and maximum values. For each parameter the maximum, minimum and average concentrations are found the GTV, PTV area around the GTV and the area of 1 cm outside the PTV. . . . .	iii

# 1

## Introduction

Breast cancer is the most prevalent cancer in women worldwide, accounting for 12% of all new annual cancer cases in 2021 [7, 8]. In 2020 the countries with the highest rate of breast cancer were Belgium and the Netherlands [8]. It is suggested that in the Netherlands approximately 1 in 8 women will develop breast cancer during their life [9]. This high number of cancer cases is associated with several risk factors, such as but not limited to family history, alcohol consumption, physical inactivity and obesity. [7–9] The average age at which the cancer is diagnosed is around 61 years [10]. As a response to these statistics, many European countries introduced a national breast cancer screening programme [11]. In the Netherlands this programme is designed for women between 50 and 75 years of age, in which they are invited every 2 years for a mammogram [12]. The reason for this is to diagnose breast cancer at an early stage, when the cancer is still localized in the breast (stage I) or has only spread to regional axillary lymph nodes (stage II) [13]. In the U.S.A., 64% of the female breast cancer cases are diagnosed when still contained in the breast and 29% when spread only to the regional lymph nodes. The 5-year relative survival rates for these categories are 99.1% and 86.1%, respectively [14].

The reported survival rates are realized due to the availability of an extensive number of treatment possibilities. Most treatment plans for early stage breast cancer include a combination of two separate therapies, for both the bulk of the tumor and the peripheral part [15]. The most common treatment for bulk removal is surgery [16]. Even though surgery is effective, it is an invasive treatment with serious side effects, such as functional and cosmetic damage due to removal of large parts of breast tissue [17]. As an alternative, the interest in thermal therapy has grown significantly, where cancerous tissue is heated up to induce irreversible cell damage, without removing large lumps of breast tissue [18].

For the peripheral part of the tumor, the remaining cancer cells are treated with radiotherapy [3]. Generally, the chosen treatment is external beam radiation, being either whole breast irradiation (WBI) or accelerated partial breast irradiation (APBI). Even though external beam radiation is effective, a large part of healthy tissue is affected too, causing significant side effects, such as skin toxicity and fibrosis [19]. An alternative treatment is low dose rate (LDR) brachytherapy, where the tumor is irradiated internally by implanting radioactive seeds in the tumor. This way the healthy tissue exposure is reduced, decreasing the radiation side effects [20].

Notwithstanding, in addition to the long term side effects, early stage breast cancer treatment is invasive to a patient's daily life while being treated. The actual treatment duration and time between treatments is long, because the treatment consists of two separately performed therapies. Therefore, even though the survival rates of early stage breast cancer are high, it is relevant to diminish the physical and psychological impact during and after recovery. To accomplish this, a novel minimally invasive treatment of early-stage breast cancer is proposed in which magnetic thermal ablation is combined with permanent LDR brachytherapy, performed simultaneously. Research on the treatment is done by research groups from both the Technical University Delft and the Erasmus Medical Centre [21]. The material used consists of rigid gel seeds containing dual-functional radioactive and superparamagnetic nanoparticles (NPs) [3]. The nanoparticles consist of a core of the radioactive isotope palladium-103 covered with a shell of superparamagnetic iron oxide. The iron-oxide can be made thermo-active using a magnetic field to heat up the nanoparticles. The synthesis of this treatment material has been proven successful [3].

The treatment is performed in a single day, where the seeds are implanted in a similar procedure as with conventional LDR brachytherapy. Immediately after, the tumor is thermally ablated using an alternating magnetic field (AMF) to heat up the nanoparticles. The goal of this part of the treatment is to eradicate the bulk of the tumor, by heating it up above 48°C. The internal radiation is delivered without clinical interference afterwards [21]. It is expected that the nanoparticles will diffuse out of the seed after implantation, even though the diffusion rate in tissue is still unknown [3]. As a result the nanoparticles will spread through the tumor tissue, irradiating not only the tissue surrounding the seed, but also the outskirts of the tumor by delivering a minimum cumulative dose of 60 Gy [22, 23]. The diffusion of nanoparticles will improve the uneven radioactive dose distribution of conventional brachyseeds [3].

Currently, there is no knowledge available yet on the behaviour of the treatment material in tissue or on the outcomes of the proposed treatment. However, this information is necessary to assess the effectiveness of the treatment and to identify the relevant physical properties and optimization parameters. This research project introduces treatment simulations to model the physical processes of both the thermal ablation and the internal radiation using the finite element

method (FEM) in Matlab. The models provide temperature, nanoparticle concentration and dose distributions over time and can ultimately be used to optimize the treatment. First, background information is provided in Chapter 2 followed by explanation on the methodology on building the models in Chapter 3. Chapter 4 gives the evaluated results obtained, including a sensitivity analysis of all parameters and an optimization strategy. The conclusion evaluates the research goal and provides recommendations to improve scientific relevance to contribute to bringing the proposed combined treatment to the clinic.

# 2

## Background Information

This Chapter provides background information on the project, including early stage breast cancer types, tumor tissue structure and available breast cancer treatments. Next, an explanation on the proposed treatment is given, followed by the physical processes relevant for the simulation of the treatment. These processes are heat, nanoparticle and radiation transport in tissue.

### 2.1. Early Stage Breast Cancer

The proposed therapy is focused on early stage breast cancer. As stated in Chapter 1, the five year survival rates for early diagnosed breast cancer are high, making it important to make the treatment as minimally invasive as possible. Early stage breast cancer means that the cancer has not spread beyond the breast tissue or the axillary lymph nodes. The cancer types this includes are non-invasive ductal carcinoma in situ (DCIS) and stage I, IIA, IIB or IIIA invasive breast cancers [13]. At later stages, the tumor has either grown into the muscles of the chest wall/the skin or has spread to multiple axillary or internal mammary lymph nodes and beyond [24]. In Figure 2.1 the anatomy of a female breast is shown. Breast cancer arises most commonly in the lining cells of the ducts (85% of tissue) or lobules (15% of tissue) in the glandular tissue of the breast [25, 26].

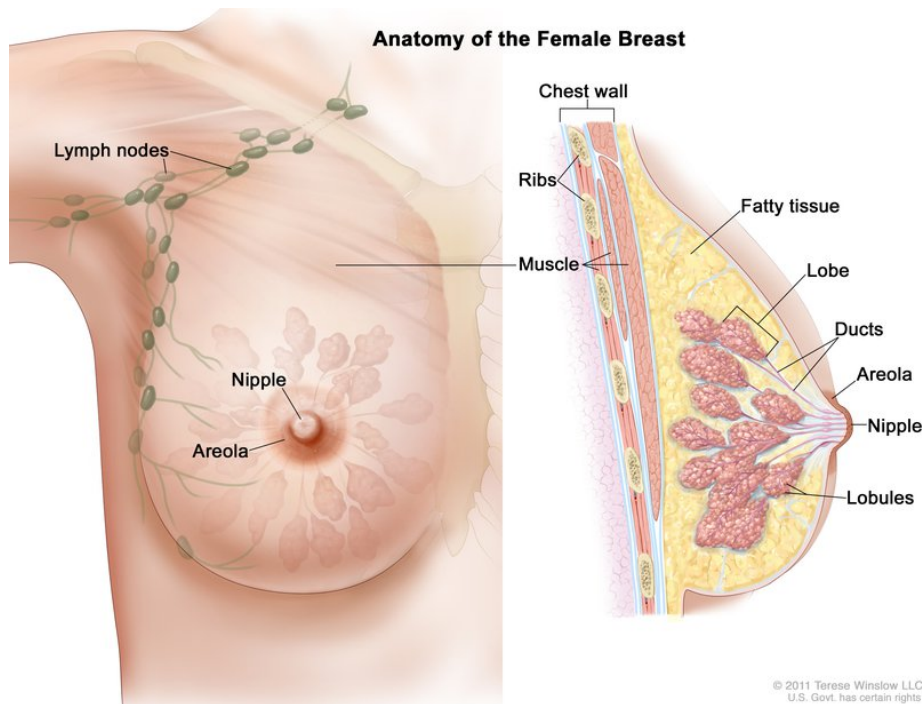


Figure 2.1: Anatomy of the female breast: front (left) and side (right) view.

#### Non-Invasive Cancer

Non-invasive (or in situ) means that the cancer has not spread beyond the breast tissue where it started. A ductal carcinoma in situ is a non-invasive breast cancer that has not spread outside the milk ducts (see Figure 2.1), the tubes that carry milk from the lobules to the nipple. DCIS is a precursor to invasive ductal carcinomas and about 16% of all breast cancer diagnoses are DCIS [25].

#### Invasive Cancer

An invasive breast cancer refers to a type that has spread into the surrounding breast tissue. The two most common types are invasive ductal carcinoma (IDC) and invasive lobular carcinoma (ILC). The first starts in the milk ducts and is most common, since about 80% of all breast cancer diagnoses are IDCs. ILC is invasive breast cancer that starts in the lobules,

the glands in the breast that produce milk. About 10% of all invasive breast cancers are invasive lobular carcinomas. Other less common invasive breast cancers are triple-negative and inflammatory breast cancers [25]. In Figure 2.2 the a schematic overview of IDC is shown. It explains the difference between the non-invasive phase of the cancer towards the invasive phase.

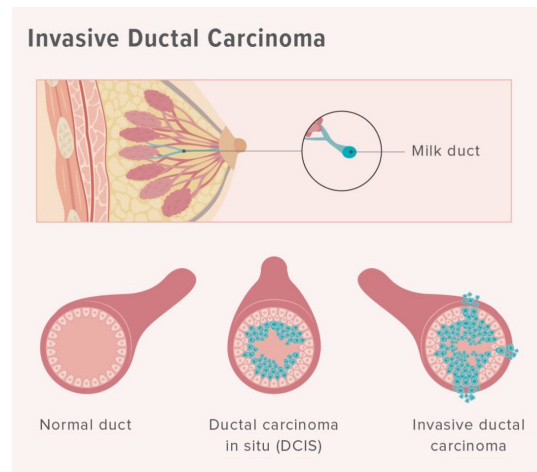


Figure 2.2: Schematic image of IDC cancer, the most common breast cancer type. It shows DCIS being a precursor to IDC [1].

## 2.2. Tumor Tissue and Structure

Most tumors are rapidly growing solid masses of tissue that mimic the structure of healthy tissue [27]. Solid tumor tissue has a cellular distribution that is heterogeneous [28]. Depending on different aspects, i.e. on tumor size and growth rate, the core of a tumor lacks proper vascular structure, resulting in a shortage of oxygen and other vital material to continue cell growth. This area of a tumor is called hypoxic and mainly occurs in the core of the tumor. In time this leads to having a necrotic core with dormant cells. Dormant cells are characterised by staying viable, but having stopped proliferating [29]. The shell of the tumor remains viable with rapidly proliferating cells surrounded by healthy tissue. The biggest factor in the rapid cell proliferation at the outskirts of the tumor, is the high permeability of microvessels in a tumor. This is a result of tumor angiogenesis, which is the growth of new blood vessels [28]. Different techniques depending on tumor and tissue type are used to form this extended fluid network.

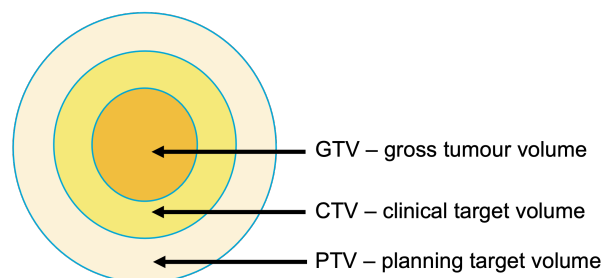


Figure 2.3: Schematic overview of the different tumor volumes that are identified during treatment planning. It includes the Gross Tumor Volume (GTV), the Clinical Target Volume (CTV) and the Planning Target Volume (PTV).

The first diagnosis of a potential breast tumor is mostly done by the patient itself or a general practitioner, noticing an anomaly in the breast. Breast cancer is then formally diagnosed via various techniques, e.g. by laboratory test or breast images. A tumor mass can be identified on the scans by a physician and radiologist. This area is called the Gross Tumor Volume (GTV) [30]. However, the visible tumor is only a part of the cancer cells. In the area surrounding the GTV, there exists a mixed shell layer of both cancerous and healthy cells, which is not visible on scans, partly due to limiting imaging resolution [31]. Additionally, the tissue surrounding the dense visible tumor core is microscopically composed for a large part healthy tissue, resulting in the cancer cell density being too low to show up on an image [32]. The edges of the imaged tumor are therefore not clearly defined and are more difficult to identify. If these cancer cells are not removed from the body too, there is a high chance of recurrence of the disease. Therefore a second area is defined, being the GTV plus a margin for sub-clinical disease spread, called the Clinical Target Volume (CTV). The correct removal of cancer cells within the CTV is important, because this volume must be adequately treated if a patient is to be cured [30]. Once these two volumes are identified, the third volume, the Planning Target Volume (PTV) is constructed. This volume takes

uncertainties in treatment planning and delivery into account. In literature, this is in the order of 10 mm approximately, to account for example for uncertainties as a result of the setup and respiratory motion [33]. In Figure 2.3 a schematic overview of the different tumor volumes is displayed.

## 2.3. Breast Cancer Treatments

There are many different treatment possibilities for early stage breast cancer. The decision on the best course of treatment, is case specific and requires information, including, but not limited to the stage, tumor size and shape, patient preference and cancer type specifics [1]. Since early stage breast cancer has high survival rates and considering it is relatively easy to treat locally when it has not spread, systemic treatments, such as hormone therapy or chemotherapy, are mostly only used as an adjuvant therapy if strictly necessary [15]. Current main treatments for early stage breast cancer include:

- Surgery: Removal of the bulk tumor and its surrounding tissue by performing a mastectomy (entire breast removal) or a lumpectomy (partial breast removal) [16]
- Radiation therapy: All treatments that use ionizing radiation to destroy cancer cells. The three types are external-beam radiation therapy (most common), intra-operative radiation therapy (radiation with probe during surgery) and brachytherapy (placing radioactive sources inside the tumor) [34].
- Thermal therapy: Heating of tumor tissue to treat cancer cells. Two types can be distinguished, the first being hyperthermia therapy, where sustained temperatures above 42 °C alter structural and functional proteins within cells [17]. It induces radiosensitizing effects, such as DNA repair blocking and reoxygenation, that improve the tumor destruction when combined with radiotherapy [35, 36]. The second therapy is thermal ablation, where tissue is heated above 46 °C to induce immediate cell death [17, 18].

For both DCIS and early-stage invasive breast cancer, doctors generally recommend surgery to remove the tumor, mostly combined with radiotherapy. Although the goal of surgery is to remove the entire tumor in the breast, microscopic cells can be left behind [15]. Another disadvantage of surgery is that it is an invasive treatment, as removed tissue can result in functional and cosmetic damage. For better local treatment, the use of radiotherapy and thermal therapy have grown [21]. The two therapies of interest for this study are thermal ablation and brachytherapy.

### 2.3.1. Thermal Ablation

Thermal ablation (TA) is a therapy where cancerous tissue is heated up above a minimum temperature of 46 °C to induce irreversible fatal cell damage to a cellular level [18]. For temperatures sustained only above 42 °C during hyperthermia treatment, only radiosensitivity is increased, not directly causing necrosis [17]. Thermal ablation is performed using nanoparticles that are injected, mostly directly, into the tumor when the patient is under full or local anaesthesia. Examples of different techniques are radio-frequency ablation, microwave ablation, laser ablation, cryotherapy, electroporation and magnetic thermal ablation [18, 37]. This research focuses on magnetic thermal ablation, where the heat is produced by oscillating magnetic nanoparticles due to an alternating magnetic field. The electromagnetic energy of the nanoparticles is transformed into heat, increasing the temperature of the nanoparticles and indirectly also the tissue surrounding the nanoparticles is heated up. Thermal ablation is very effective in cancer cell death, but unfortunately the healthy cells will be killed as well, which is a big disadvantage. As the heat distribution is determined by the location of an individual nanoparticle, it is difficult to treat only locally if the nanoparticles are not contained at their initial injection site, which gives a high chance of damaging healthy tissue in the outer parts of the tumor [21]. In Figure 2.4a a schematic overview of thermal ablation treatment to a tumor is given.

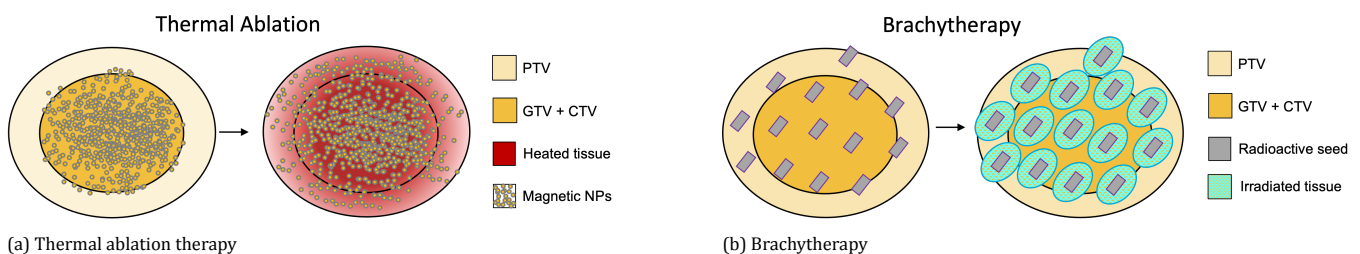


Figure 2.4: Schematic overview of therapies of interest. These are the therapies on which the newly proposed therapy is based.

### 2.3.2. Brachytherapy

Brachytherapy is a form of internal radiotherapy where radioactive rigid 'seeds' are implanted inside the tumor. The surrounding tissue is then irradiated, resulting in DNA damage [20]. Cancer cells have a broken DNA repair mechanism, which is why the cells keep reproducing without repairing or stopping themselves. However, some DNA compromised cancer cells are more vulnerable, because if damaged badly enough, their DNA is not strong enough to repair themselves

and they will die [34, 38]. Healthy cells are better able to repair damaged DNA, making radioactive irradiation (in general) a good treatment to have a high healthy tissue survival rate, while effectively killing cancer cells [38]. A big advantage of brachytherapy is that it has a high accuracy level, due to the short penetration depth of the ionizing radiation and due to the possibility to plant the seeds at a specific location in the tumor using a brachytherapy template and imaging. This high accuracy results in proper local treatment, sparing more healthy tissue compared to external beam radiation [20]. However, the local treatment can also be a disadvantage since the seeds become radiation 'hot spots'. Radiation hot spots are the regions within an area of interest where the level of radiation is significantly higher than in neighboring regions [39]. This concept is shown in Figure 2.4b, where it is visible that only a part of the tumor tissue is irradiated by the radioactive seeds. Additionally, the treatment procedure is argued to be more invasive, because of the brachyneedles puncture the breast [40].

Brachytherapy can be performed in two ways, either with high dose rate (HDR) temporary irradiation or with low dose rate (LDR) permanent implants that remain in the patient after recovery. The number and location of seeds are patient specific as they depend for example on the size and shape of the tumor. The size and location are determined by a computer-generated treatment plan [41]. For prostate cancer, on average between 40-150 seeds are implanted inside the tumor [42]. Since the goal of the newly proposed therapy is to reduce clinical interventions for the patient, the LDR permanent implants are most suitable. This way the patient is not required to visit the hospital for every radiation fraction, as is the case for HDR brachytherapy. The most commonly used LDR radioactive isotopes are iodine 125 (I-125) and palladium 103 (Pd-103) [20].

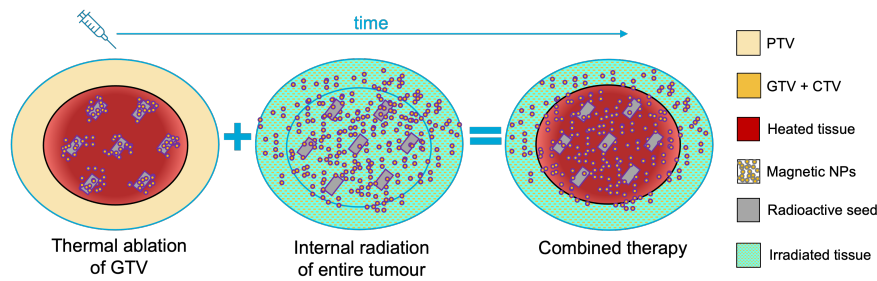


Figure 2.5: Schematic overview of the result of the newly proposed thermo-brachytherapy. First, the magnetic field heats up the nanoparticles that burn the core of the tumor, followed by irradiation by the nanoparticles to the outskirts of the tumor.

## 2.4. Proposed Multi-Modal Thermal Brachytherapy

There is only little published research on performing both thermal ablation and brachytherapy for tumor treatment [2, 43–45], none of which reports on combining both therapies together as a single treatment. The therapies are either performed sequentially (on patients with liver carcinomas) [44] or they are combined with chemotherapy [45]. This research, however, proposes a new treatment for early-stage breast cancer combining brachytherapy and magnetic thermal ablation by using radio- and thermo-active nanoparticles as treatment material.

The goal of the therapy is to treat the tumor with a single medical intervention, by killing the cancerous cells with heat and radioactive radiation. Firstly, heat is produced during the thermal ablation part of the treatment. The objective is to kill all cancerous cells within the GTV part of the tumor, within about 20 minutes, by heating it above 48°C. As described in Section 2.5.1, temperatures above 48°C kill cells. However, high temperatures outside the GTV harm the healthy cells in the outskirts of the tumor and are therefore undesired. To prevent this, it is desired that the tissue outside of the GTV is not heated above 45°C [21]. Secondly, the radioactive properties of the nanoparticles are used to irradiate the tumor tissue to kill the cancerous cells and spare the healthy ones. It is expected that, to achieve homogeneously delivered cumulative dose to the entire PTV volume, it is necessary for the nanoparticles to diffuse out of the seeds and spread throughout the PTV area. This should happen within the first few half-lives of the Pd-103 isotopes ( $t_{1/2} = 17$  days [46]), seeing that the activity of the isotopes decreases over time. The half-life of a radioisotope is the time it takes for the activity to half of its initial value, where activity is determined by the number of unstable atomic nuclei that decay per second. The minimally required concentration of nanoparticles and their distribution depends on the radioactive dose delivered by the nanoparticles and is yet to be determined. The minimum cumulative dose required to determine the minimally required concentration of nanoparticles in the PTV is 60 Gy [22, 23]. Another condition is that the nanoparticles must not have spread outside of the PTV into the healthy tissue above a yet undetermined maximum concentration, to ensure the cumulative dose does not reach higher values than acceptable for healthy tissue. Within this project the maximum cumulative dose to healthy tissue outside the PTV is taken to be 60 Gy. Radiation outside the PTV is undesirable, because it is assumed that the area surrounding the PTV only consists of healthy cells. This can potentially be dangerous if the cells are damaged beyond repair.

The combined treatment will have smaller physical impact, because a larger part of the breast tissue is spared if not removed during surgery. Additionally, it is psychologically and socially less difficult during the course of the entire treatment, when not being obliged to follow the intensive fractionated treatment [21]. This is possible because the seeds are implanted permanently and because the patient is exposed to the magnetic radiation only once and directly after implantation. The biggest advantage is that the radioactive material can irradiate the tumor from the inside immediately after the thermal ablation part, meaning that the material carries out the rest of the treatment without further interference with the hospital.

### 2.4.1. Thermo- and Radioactive Nanoparticles

The combined treatment relies on nanoparticles incorporated in brachyseeds, namely Pd-103 super-paramagnetic iron oxide (Pd-103 SPIO) nanoparticles. The nanoparticles consist of multiple layers:

1. A core of radioactive Palladium-103;
2. A shell of super-paramagnetic iron oxide;
3. An outer silica layer for biocompatibility.

These nanoparticles are then incorporated into a rigid gel which forms the seed material. The seeds are implanted into the tumor similar to a standard LDR brachytherapy procedure. A schematic overview of the composition of the nanoparticles is visible in Figure 2.6.

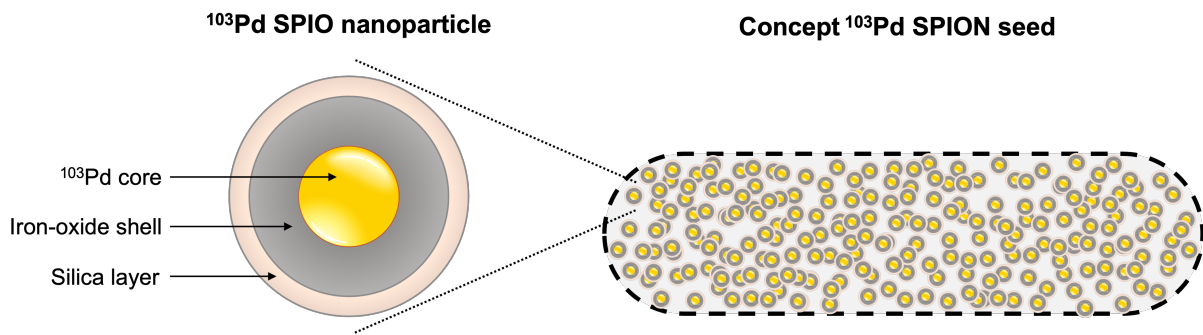


Figure 2.6: Overview of the composition of Pd-103 superparamagnetic iron oxide nanoparticles and the seeds they are incorporated in. The nanoparticles consist of multiple layers, namely: 1. Radioactive Pd-103 core; 2. Thermoactive SPIO layer; 3. Silica layer for biocompatibility and leak prevention. These nanoparticles are incorporated in a solid gel, forming the brachyseeds that are injected into the tumor.

#### Palladium-103 Core

The used radioisotope is palladium-103, which is an X-ray source due to electron capture. In literature, both iodine-125 and palladium-103 are widely used for LDR brachytherapy [47]. Both are favoured as radioisotopes, because of multiple favourable physical properties. Firstly, because the seeds will be implanted permanently, a low energy source is preferred [48]. The energy of a radioactive source determines the penetration depth of the particles emitted from the source [47]. If the radiation energy of an implanted source is too high, the source deposits energy too deep into the tissue causing too much healthy cells to be damaged over time [47]. The energy of the X-rays of Pd-103 is 21 keV and 28 keV for I-125. HDR isotopes have energies between 380-1250 keV [48]. Secondly, the half life of Pd-103 is relatively short, 17 days, compared to I-125, 60 days [46]. The strength of a radiation source decays exponentially. For permanent implants a short half life is desired, partly because it can reduce the risks of radiation exposure of the patient's partner [49]. Moreover, if activity is equal, radioisotopes with short half lives have a higher initial dose rate compared to radioisotopes with long half lives. It is suggested that a higher dose rate returns a larger biological effect on cancer cells [50]. It is expected that several thousands of Pd atoms will be loaded into the nanoparticles, which makes the radiation dose per Pd SPIO nanoparticle higher than in conventional therapies. The diameter of the core of the nanoparticle will be 5 nm [21].

#### Superparamagnetic Iron-oxide (SPIO) Layer

The Pd-103 radioisotopes are covered with a layer of SPIO material. In literature it is found that single iron oxide nanoparticles have great potential due to their biocompatibility and biodegradability. These magnetic nanoparticles (MNPs) can be used for a wide range of applications [17]. However, forming a shell of this material is more difficult, because it has to be formed around the Pd core. For the shell, ferrous salts will be used with tetramethylammonium hydroxide to synthesize  $\text{Fe}_3\text{O}_4$  nanoparticles as described by Cheng *et al.* [51]. The iron oxide will exhibit super-paramagnetic behavior; when the material is subjected to an alternating magnetic field and when the diameter is less than approximately 20 nm. [17]. Also, the superparamagnetic behavior is temperature dependent within a minimum and maximum range. When a temperature below the so called blocking temperature is reached, the nanoparticle will lose its superparamagnetic behaviour as it is blocked in its initial state where no magnetization flip is possible [52]. The blocking temperature for

the Pd-103 SPIO nanoparticle is not yet known, but the nanoparticles do show superparamagnetic behavior above 37°C, assuming it is lower than body temperature. Likewise, at temperatures above the Curie temperature certain magnetic materials undergo a sharp change in their magnetic properties. The Curie temperature is not yet known for the treatment material, however, experiments have proved that the superparamagnetic behaviour is sustained at temperatures up to 80°C. The treatment material can be imaged with MRI to track the diffusion of the nanoparticles. The layer will be of 10 nm thickness [21].

### Silica Layer

The third layer of the nanoparticle is a silica shell. This is added to the nanoparticle to minimize leaks of metal-ions and to ensure biocompatibility. It also helps to prevent aggregation of the nanoparticles and to increase the long-term stability [21]. However, coating the MNPs reduces the outflow of heat, which results in decreased heating efficiency [53]. The synthesis of the inorganic silica layer is done through the reaction with tetraethyl orthosilicate in ethanol with ammonia. The thickness of the silica layer is controlled by the rate of addition of the reactants and since the reaction time is not yet determined, it is still unknown [21].

### Seed Material

The nanoparticles will be embedded into a solid gel that forms the seed. It is necessary to have a solid solvent material to be able to implant it into the tumor using brachyneedles. A possible seed material is alginate gel that has a very low viscosity and is let to thicken for 24 hours before the Pd-SPIO nanoparticles are added [21, 40]. However, it is not yet decided what material is will be used. The desired size of the seeds is 2 mm in diameter and 5 mm in length.

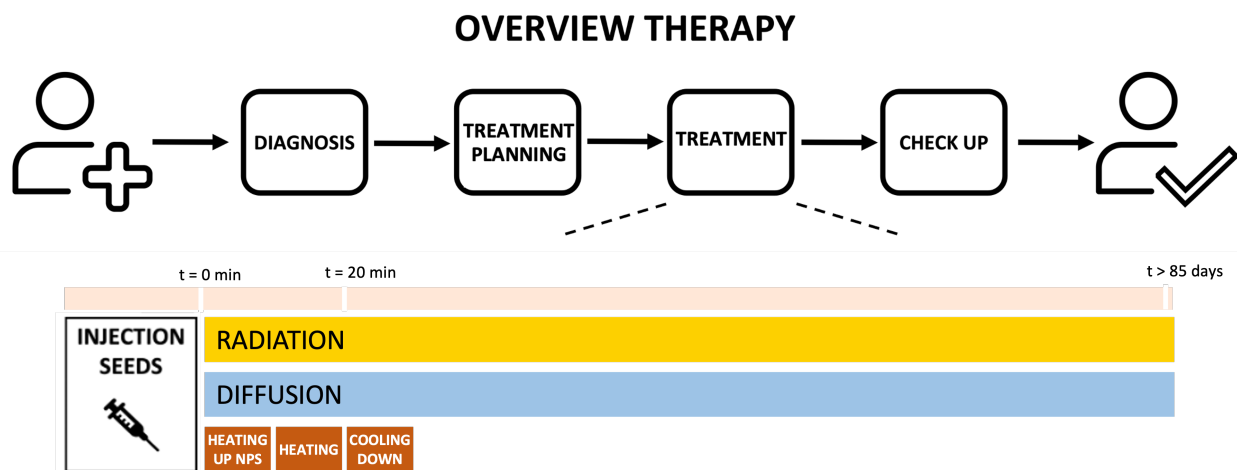


Figure 2.7: Overview of the proposed therapy from the diagnosis of the sick patient to the end of the therapy. The treatment timeline is visible at the bottom, showing that the two thermal ablation (orange) and the radiation (green) happen simultaneously at the start. It is also visible that after the alternating magnetic field is switched off no more medical intervention is required.

### 2.4.2. Treatment Procedure

The treatment procedure of the proposed therapy is described in this section and is visible in Figure 2.7. After the synthesis of the nanoparticle filled seeds and thorough treatment planning, the seeds are injected into the tumor similarly to a conventional brachytherapy procedure, using needles and a standard template. Subsequently, an alternating magnetic field (AMF) is applied to induce heat by radiofrequency (RF) induction coils. The AMF does deposit energy indiscriminately to tissues of which the extent of the damage to tissue is not yet known [36]. When magnetic nanoparticles are exposed to an alternating magnetic field, four different mechanisms can generate heat within the therapeutic system: 1. Hysteresis loss, 2. Eddy current, 3. Néel relaxation and 4. Brownian relaxation [36, 53, 54].

Magnetic hysteresis occurs when the magnetizing force of a magnetic field is reversed in the opposite direction and internal friction of the aligned magnetic material opposes this reversal. This phenomenon is induced by an alternating magnetic field. This friction is overcome by using the magnetising force, losing part of the magnetic energy in the form of heat, called hysteresis loss [54, 55]. Eddy currents are loops of electrical current induced by a changing magnetic field, that lose energy in the form of heat due to the resistance of the material [54]. The SPIO nanoparticles have a layer of iron oxide. Since oxides have a high electrical resistivity compared to pure metals, the Eddy currents are assumed less significant for magnetic nanoparticle heating [36]. Additionally, Eddy currents are only significant in materials at larger scale (>cm) [54]. Because the nanoparticles are significantly smaller in size, the Eddy currents are limited further. Therefore the heating effects due to Eddy currents are assumed negligible [36].

Néel and Brownian relaxation only occur in single-domain magnets [36], i.e. the SPIO nanoparticles. Upon switching the direction of the alternating magnetic field, the magnetic Néel and Brownian moments rotate due to different thermal relaxation mechanisms. Néel relaxation is the mechanism where only the individual magnetic moment inside the magnetic core is re-orientated while the particle remains fixed. The thermal energy is dissipated by rearrangement of atomic dipole moments [54]. Brownian relaxation refers to the rotation of the entire nanoparticle itself in the carrier liquid, including the magnetic moment around their axis [36, 56]. This mechanism generates thermal energy through shear stress between the nanoparticle and the surrounding material [54]. The heat generated by these mechanisms is transferred to surrounding cells, not being selective to only cancerous cells. However, since the seeds are injected into the gross tumor volume, it is expected that the nanoparticles will solely heat the tumor cells. The goal is to heat up the entire GTV above 48°C, killing the tumor cells due to immediate fatal damage [2].

The heat produced can be controlled by the size, concentration and injection location of the nanoparticles, or by the settings of the applied magnetic field, such as strength, frequency and time it is applied. Currently, it is suggested that after about 20 minutes of thermal ablation, the magnetic field is switched off and no more heat is produced by the nanoparticles. The heat is removed from the tumor site by blood perfusion and by heat diffusion [57]. Then the thermal ablation part of the treatment is finished. It is assumed that, directly after implementation of the seeds, the radioactive Pd-SPIO nanoparticles start diffusing simultaneously out of the seeds into the surrounding tissue. Because the diffusion coefficient is suggested to be small (order of magnitude  $10^{-8}$  [5, 58]), it is expected that this diffusion process will be slow, resulting in the nanoparticles only having travelled a very small distance during the TA procedure. Therefore it is assumed that the diffusion of nanoparticles has no influence on the spread of the heat.

The second part of the treatment is the LDR brachytherapy, that happens internally in the tumor meaning the patient does not have to be present in the hospital anymore. The Pd-103 isotopes in the core of the nanoparticles decay over time releasing X-rays and Auger electrons, irradiating the tissue within a 10 cm range and  $\sim 0.1$  mm range, respectively. (see Section 2.5.3). The iron-oxide layer does not influence the dose distribution significantly. The shielding effect of the iron oxide shell has proven to be negligible on the dose profile [3]. Over time, the nanoparticles diffuse to the outskirts of the tumor too, where the radioactive isotopes damage the still viable cells in the outer layer of the tumor. By damaging rather than killing the healthy cells, a large part of the healthy tissue is spared [38]. The goal is to have the nanoparticles diffused sufficiently through the PTV to still deliver a significant radiation dose to the outskirts of the tumor. The diffusive radioactive nanoparticles improve the uneven radioactive dose distribution of the conventional brachyseeds, because they will spread through the tumor instead of being stationed at their initial location [21]. The radioactive nanoparticles decay over time to a negligible activity and are slowly removed from the tumor site through the blood vessels. The killed cells and the nanoparticles are cleared from the blood by the reticuloendothelial system by macrophages [17]. An overview of the proposed treatment is shown in Figure 2.5.

## 2.5. Physical Processes Underlying the Proposed Treatment

To gain knowledge of the behaviour of the material in the body and to find out the impact of the treatment to the tumor destruction, it is necessary to understand the mass and heat transfer processes in the human body. First the temperature distribution by heating of the nanoparticles is described, followed by the diffusive behaviour of the material through (tumor) tissue coupled with the radioactive dose distribution.

### 2.5.1. Heat Transfer in Tissue

To find the temperature distribution over time, a governing energy equation must be found to describe the heat transfer system. The general energy balance is given by:

$$\rho c_p \frac{\partial T(\vec{r}, t)}{\partial t} + \vec{\nabla}(\vec{v}(\vec{r}) \cdot T(\vec{r}, t)) = \vec{\nabla}(k(\vec{r}) \cdot \vec{\nabla}T(\vec{r}, t)) + Q(\vec{r}, t), \quad (2.1)$$

including the material specific density  $\rho$ , the specific heat  $c_p$  and the time and space dependent temperature  $T(\vec{r}, t)$ . The second term describes the convection of heat, depending on fluid flow velocity  $\vec{v}(\vec{r})$ . The third term describes the heat conduction that depends on the heat conduction coefficient  $k(\vec{r})$ . Conduction is the spontaneous process where heat flows from a hotter to a colder body and is continuous. The last term represents all heat sources  $Q(\vec{r}, t)$  within the system. To specify the energy balance for body tissue, the generally accepted equation in literature is Pennes' bioheat transfer equation (Equation 2.2) [57]. In this Equation convective blood flow is included as a heat sink instead of a heat convection term. This removal of heat is due to blood perfusion. Pennes' equation is described by:

$$\rho c_p \frac{\partial T(\vec{r}, t)}{\partial t} = k \cdot \vec{\nabla}^2 T(\vec{r}, t) + \omega_b(\vec{r}, T, t) \cdot c_b \cdot (T_b - T(\vec{r}, t)) + Q_m(\vec{r}), \quad (2.2)$$

where  $\rho$  is the density [kg/m<sup>3</sup>],  $c_p$  is the specific heat [J/(kg °C)] and  $k$  is the thermal conductivity [W/(m °C)], all of

which are tissue specific and assumed constant. In Equation 2.2,  $\omega_b$  is the blood perfusion rate [ $\text{kg}/(\text{s m}^3)$ ],  $c_b$  represents the specific heat of blood [ $\text{J}/(\text{kg } ^\circ\text{C})$ ],  $T_b$  is the blood temperature [ $^\circ\text{C}$ ] and  $Q_m$  is the metabolic heat generation per unit volume [ $\text{W}/\text{m}^3$ ]. The first term of the Equation is the time dependent term, the second the conduction term and the third term represents the blood perfusion. Blood perfusion refers to the blood passing through vessels in biological tissues, in order to provide oxygen, deliver important nutrients to tissues and remove waste substances [59]. By multiplying the blood perfusion rate  $\omega_b$  with the specific heat of blood  $c_b$  and the temperature gradient between the incoming temperature  $T_b$  and local tissue temperature  $T$ , the amount of heat removed from or added to the system is calculated per unit time [ $\text{W}/\text{m}^3$ ].

Even though Pennes' bioheat equation is widely accepted, there are several limitations to the equation. Pennes made some assumptions and simplifications, which make Equation 2.2 not completely accurate to the real physical processes. First, the blood velocity field is not taken into account in all directions, but only in the direction that removes heat from the system. This way, the convection is added as a heat sink, with the driving term being the temperature difference [57]. This simplifies the equation strongly, as it disregards the Navier-Stokes relation describing the convective flow, which would increase the temperature distribution. However, by including this blood perfusion term, Pennes' equation does consider heat removal partly, describing the physical process more accurately.

Secondly, he assumed that metabolic heat  $Q_m$  is constant throughout the human body. However, it is known that metabolic heat not only strongly differs between individuals, it also changes throughout the body. Due to muscle activity and atmospheric conditions, among other reasons, the metabolic heat generated is not constant. The metabolic heat produced by exercising muscles is transported by the circulating blood flow to the surface of the body and released to the environment [60]. Furthermore, in the equation, the thermal properties per tissue type are assumed constant, as well as the blood temperature [61]. By assuming a fixed value for the baseline temperature of blood, the temperature difference is only dependent on the temperature variable [62]. Additionally, the equation does not take other thermoregulation factors into account, such as shivering and regulatory sweating [63]. By neglecting these factors, blood perfusion is assumed the only temperature regulating term.

The local blood perfusion rate is also assumed constant in Pennes' equation [61]. However, it is proven that the blood perfusion rate depends on tissue, temperature and time [2, 64], although there is no consensus yet in literature on the absolute relation. The blood perfusion rate dependence on tissue is a result of the vascular network of a tissue type. As explained in Section 2.2, the vascular structure of a tumor is heterogeneous, having a necrotic core with no convective fluid flow and a viable shell around it with increased fluid flow compared to surrounding healthy tissue. However, the size of the necrotic core of a tumor is case specific. The blood perfusion rate also differs per healthy tissue type.

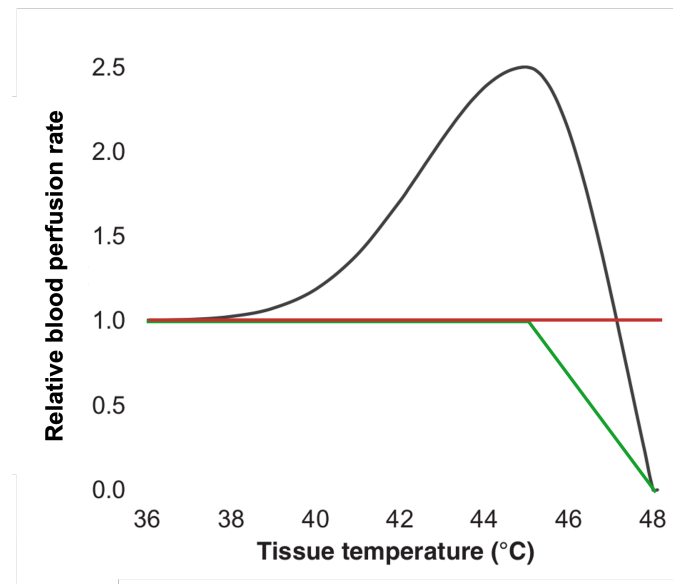


Figure 2.8: This graph shows three different relations between the relative blood perfusion rate and the tissue temperature. The red line represents the constant blood perfusion rate assumed in Pennes' bioheat equation (Equation 2.2). The green line shows the relation where blood perfusion decreases linearly to zero above  $T_{cr}$  (2.4). The black line gives the relation where the blood perfusion rate increases for  $T < T_{critical}$  and decrease above  $T_{critical}$  (2.5) [2]. The blood perfusion rate is described as the relative difference between the proposed blood perfusion rate compared to the initial blood perfusion rate  $\omega_{bi}$ .

In addition, the thermal ablation treatment itself strongly effects the blood perfusion rate  $\omega_b$ , as it is argued that blood perfusion is also dependent on tissue temperature and time. It is known that a cell is destroyed if it is heated above a certain temperature. This does not only apply to tumor cells, but also to the vascular cells. *Stauffer et al.* suggest this effect is induced for cells heated above 48°C [2]. Above this temperature, the vascular structure is said to be destroyed and the blood perfusion rate becomes zero. Additionally, it has been proven experimentally that the blood perfusion rate first increases with increasing temperature, up to a certain critical temperature  $T_{cr}$ . Above this temperature the blood perfusion rate decreases to zero [2, 64]. Pennes' bioheat equation assumes a constant blood perfusion, independent of temperature. In literature alternative relations between the blood perfusion rate and temperature are proposed. Three different blood perfusion relations are introduced to describe the effect of temperature to blood perfusion, which are given in Figure 2.8. The first and default expression is a constant blood perfusion rate (Equation 2.3), used in Pennes' bioheat equation [57]. It assumes no decrease in perfusion rate at higher temperatures, i.e. no dependence on temperature and time, resulting in  $\omega_b$  being equal to the initial blood perfusion rate  $\omega_{bi}$ :

$$\omega_b(T) = \omega_{bi}. \quad (2.3)$$

The decrease of blood perfusion above the critical temperature of 45°C is taken into account in the second relation that is tested, Equation 2.4. It assumes a constant  $\omega_b$  below  $T_{cr}$  and a linear decrease in blood perfusion to zero above  $T_{cr}$ :

$$\omega_b(T) = \begin{cases} \omega_{bi} & \text{for } T \leq T_{cr} \\ \omega_{bi} * (1 - 0.33(T - T_{cr})) & \text{for } T_{cr} < T < 48^\circ\text{C} \\ 0 & \text{for } T > 48^\circ\text{C} \end{cases}. \quad (2.4)$$

The third equation is proposed by *Stauffer et al.* In literature it is suggested that the blood perfusion rate is first increased for a small increase in temperature before the vascular system is damaged [2, 64]. This means that blood flow is increased to remove the excess heat. The relation proposed is:

$$\omega_b(T) = \omega_{bi} * F(T) = \begin{cases} \omega_{bi} * (1 + \alpha * e^{-\frac{(T-T_{cr})^2}{\beta}}) & \text{for } T \leq T_{cr} \\ \omega_{bi} * ((1 + \alpha)(1 - \gamma) + \gamma(1 + \alpha) * e^{-\frac{(T-T_{cr})^2}{\beta}}) & \text{for } T_{cr} < T < 48^\circ\text{C} \\ 0 & \text{for } T > 48^\circ\text{C} \end{cases}, \quad (2.5)$$

with the assumptions  $\alpha = 1.5$ ,  $\beta = 12$  and  $\gamma = 3.1588$  [2]. The last two blood perfusion rate equations also depend on time, because the temperature is time dependent. Figure 2.8 shows the difference between a constant blood perfusion rate, a linearly temperature dependent blood perfusion rate and a proposed relation, where the blood perfusion rate increases up to a critical temperature, before linearly decreasing to zero. The impact of these different relations on the temperature distribution are tested within this study.

In spite of the limitations, Pennes' equation is simple, with a small number of physical parameters, lending itself to applications such as this project. Equation 2.2 describes the heat distribution through biological tissue during a normal state. However, during the proposed treatment, an additional local heat source is added to the system, namely the heated nanoparticles. The nanoparticle heat  $Q_{NP}$  is calculated using:

$$Q_{NP} = \text{SAR}_{NP} \cdot \text{mass\%} \cdot \rho, \quad (2.6)$$

where SAR (Specific Absorption Rate) of the nanoparticles is the power absorbed per unit mass by tissue [W/g] and  $\rho$  the density of the tissue material [kg/m<sup>3</sup>]. The mass fraction accounts for the concentration of nanoparticles in the seed [mass%]. Adding this to Equation 2.2, results in:

$$\rho c_p \frac{\partial T(\vec{r}, t)}{\partial t} = k \cdot \vec{\nabla}^2 T(\vec{r}, t) + \omega_b(\vec{r}, T, t) \cdot c_b \cdot (T_b - T(\vec{r}, t)) + Q_m(\vec{r}) + Q_{NP}, \quad (2.7)$$

with  $Q_{NP}$  being the nanoparticle heat source added to the system when the AMF is turned on [W/m<sup>3</sup>]. Generally in literature, the  $Q_m$  term is ignored, because the magnitude of the metabolic heat is substantially smaller than other terms in the equation, such as the nanoparticle heat generation [65]. Equation 2.7 is the final equation used in the computational model to investigate the temperature distribution over time.

### 2.5.2. Nanoparticle Transport in Tissue

The physical processes that influence the transport of the nanoparticles over time are included in the convection-diffusion equation, that is adjusted as a result of simplifications and assumptions. The general governing equation for the nanoparticles, assuming spatially constant diffusion coefficient  $D$  [m<sup>2</sup>/s], is:

$$\frac{\partial c(\vec{r}, t)}{\partial t} + \nabla(\vec{v}(\vec{r}) \cdot c(\vec{r}, t)) = D \cdot \nabla^2 c(\vec{r}, t) + J_{\text{source}}(\vec{r}, t) + J_{\text{sink}}(\vec{r}, t), \quad (2.8)$$

where the first term represents the time dependency of the equation with  $c(\vec{r},t)$  defined as the quantity of interest, being the time and space dependent nanoparticle concentration [#NP/m<sup>3</sup>]. When applying the material balance to the human body, the second term is the convective flow of the material through tissue, with  $\vec{v}(\vec{r})$  being the fluid flow velocity [m/s] driven by the blood vascular system and lymphatic system, described in Equation 2.9. The blood vascular system acts as a fluid source where blood fluid is transported across the vessel walls into the tissue,  $\phi_V$ , and the lymphatic system removes the interstitial fluid from the tissue,  $\phi_L$ . The third term in Equation 2.8 describes diffusion, which is the phenomenon of nanoparticles moving from a higher concentration to an area of lower concentration. Coefficient  $D$  is the diffusion coefficient [m<sup>2</sup>/s]. The last two terms on the right hand side of Equation 2.8 form the source of material added to the system, due to transvascular fluid exchange by blood  $J_{\text{source}}(\vec{r},t)$  and the sink of material being removed from the system due to lymphatic vessels  $J_{\text{sink}}(\vec{r},t)$ . The addition of the nanoparticles to the system during the injection, are handled as the initial condition.

The convective term includes the fluid velocity  $\vec{v}(\vec{r})$ , which is not constant through the different tissue types. In the necrotic core region of the tumor, there will not be any fluid transport due to the absence of micro blood vessels and the lymphatic systems. In the viable tumor region, there is transvascular transport of fluid by the microvessels, but an absence of a functional lymphatic system is reported. In normal tissues, the fluid is transported via both blood extravasation, the leakage of fluids from the vein into the surrounding tissue, and lymphatic drainage, where the interstitial fluid is drained from the tissue into the lymph vessels [28]. Equation 2.9 shows the transvascular fluid velocity for two different tumor areas and the normal breast tissue.

$$\nabla \vec{v}(\vec{r}) = \begin{cases} 0 & , \text{ for necrotic tumor} \\ \phi_V & , \text{ for viable tumor} \\ \phi_V - \phi_L & , \text{ for healthy tissue} \end{cases} \quad (2.9)$$

with  $\phi_V$  being the transvascular fluids source term by blood vessels [1/s] and  $\phi_L$  the fluids sink term by lymphatic drainage [1/s]. Both are driven by interstitial fluid pressure. The equations for  $\phi_V$  and  $\phi_L$  are derived by Mahesh *et al.*

Diffusion of the nanoparticles through tissue is the main driving force of the nanoparticle distribution and the rate at which a material diffuses through a surface is defined by the diffusion coefficient  $D$ . In this case, the diffusion coefficient represents the rate at which the nanoparticles diffuse through the tumor and healthy tissue. The values can be found in Table 3.2.

The nanoparticle source  $J_{\text{source}}(\vec{r},t)$  and sink  $J_{\text{sink}}(\vec{r},t)$  terms represent the transvascular exchange which takes place through the capillary walls. It is assumed that the walls are semipermeable membranes [28]. The source is described by the transcapillary exchange through blood vessels  $J_V(\vec{r},t)$  and the sink by the exchange through lymphatic vessel walls  $J_L(\vec{r},t)$ :

$$J_V(\vec{r},t) = \begin{cases} 0 & , \text{ for necrotic tumor} \\ -P \frac{S}{V} \frac{Pe}{e^{Pe}-1} c(\vec{r},t) & , \text{ for viable tumor and healthy tissue} \end{cases} \quad (2.10)$$

$$J_L(\vec{r},t) = \begin{cases} 0 & , \text{ for necrotic and viable tumor} \\ \phi_L c(\vec{r},t) & , \text{ for healthy tissue} \end{cases} \quad (2.11)$$

with concentration of nanoparticles  $c(\vec{r},t)$  [#NPs/m<sup>3</sup>], Peclet number  $Pe$ , permeability coefficient  $P$  [m/s] and the surface area of microvessels per unit volume of the tissue  $\frac{S}{V}$  [1/m] [28]. Equations 2.10 and 2.11 and their corresponding parameters are derived by Mahesh *et al.* [28]. Due to the thermal ablation at the start of the treatment, all tissue cells are destroyed, including the vascular structure of the tumor. This means there is no more transport of fluid through microvessels in the ablated area and its surroundings. This has great influence on the convection of nanoparticles and the transvascular exchange.

### 2.5.3. Radiation Transport in Tissue

The goal of the internal radiation of the cancerous cells is to kill all cancerous cells within the PTV. To achieve this, the dose absorbed by the tumor tissue must be sufficient. The general prescription for breast cancer radiation therapy ranges between a total cumulative dose of 40 to 60 Gy [22, 23]. The concentration distribution provides information on the number of nanoparticles at each location for different points in time. To give meaning to this concentration distribution and to the minimum and maximum concentrations mentioned in Section 2.4, it is necessary to assess what delivered dose has accumulated at each location.

The nanoparticles are radioactive due to their core of radioactive Palladium-103. Palladium-103 decays to Rhodium-103 by electron capture, emitting X-rays and electrons [66]. The dose distribution calculated in this project makes use of the

relation between the dose rate and the radial distance from the centre of the radioactive nanoparticle. Dose rate describes the delivered dose per unit of time for a specified time step, in this study in unit of Gray per hour [Gy/h]. The radial dose distribution used is provided by van Oossanen *et al.* [3]. By performing Monte Carlo simulations, the spherical radiation dose distribution for a single nanoparticle was characterized, defining the nanoparticle as a point source. The dose rate is found by calculating the total delivered dose per hour in the shell at a specific radial distance from the centre. This dose is expressed as the spherical dose rate delivered at a radial distance by a single nanoparticle with a Palladium-103 decay rate of  $\sim 100,000$  decays per hour. The radial dose distribution is given in Figure 2.9. This Figure shows on a double logarithmic scale the dose delivered by the electrons, which are more dominant at shorter distance, and the dose delivered by X-rays, which are more dominant at larger distances. The influence of the iron-oxide shell shielding the radiation is included in these simulations [3]. It is assumed that each nanoparticle contains the same number of Palladium-103 nuclei in the core, meaning the dose distribution of Figure 2.9 applies to every nanoparticle.

The radioactive delivered dose rate over time is calculated by calculating the location specific delivered dose over time  $\dot{D}_i(r_i,t)$ . The delivered dose at a specific location  $r_i$  equals the sum of the delivered dose rate of each nanoparticle in the system  $n$ . The distance  $\bar{r}_{ij}$  between the location of interest  $r_i$  and the centre of a nanoparticle  $r_j$  determines the dose rate by that specific nanoparticle  $\dot{D}_{ij}(\bar{r}_{ij})$ . The dose rate at a specific location is described by equation:

$$\dot{D}_i(r_i,t) = e^{-\lambda t} \sum_{j=1}^n \dot{D}_{ij}(\bar{r}_{ij}), \quad (2.12)$$

where  $\dot{D}_i(r_i,t)$  is the cumulative dose rate at a specific time at point  $i$  in [Gy/h].  $\dot{D}_{ij}(\bar{r}_{ij})$  is the dose rate at location  $i$  delivered by a single nanoparticle  $j$  in [Gy/(h-NP)]. The exponential term represents the radioactive decay factor, which corrects for the relative decrease in activity of the nanoparticle over time. A decrease in activity results in lower dose rate. By calculating the dose at a specific location over time, the cumulative delivered dose per location is found. Lastly, these local cumulative doses are used to get the total cumulative dose distribution. By comparing the dose distribution to the maximum acceptable dose to human cells, it can be evaluated whether the delivered dose is sufficient to kill all cancer cells in the PTV.

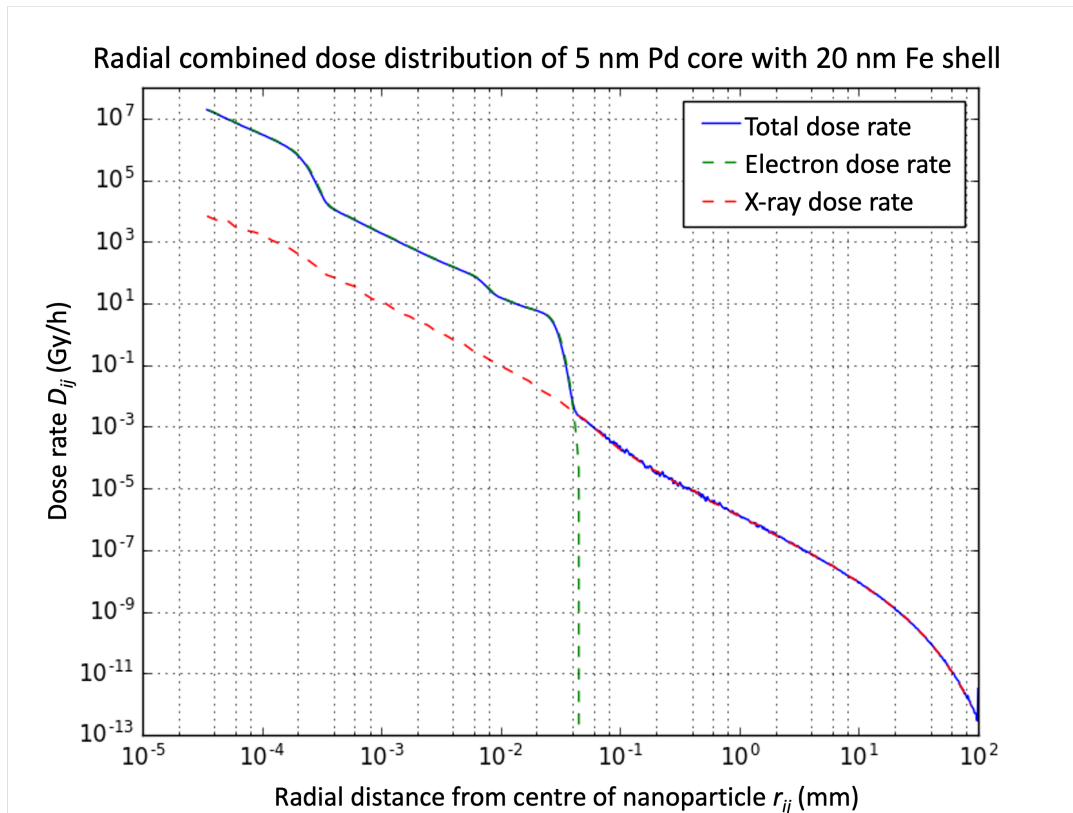


Figure 2.9: The radial dose distribution of combined radiation of a single nanoparticle with a 5 nm palladium core and 20 nm iron oxide shell. It uses the simulated results of the energy spectra of the electrons and photons leaving the nanoparticle. On the y-axis the relative delivered dose rate  $\dot{D}_{ij}$  by  $\sim 100,000$  Palladium-103 decays per hour is given for different distances from the centre of the nanoparticle  $r_{ij}$  [3].

# 3

## Methodology

This chapter covers the method used to perform the research and includes the required information of the design of the built models. First, the numerical method is described, followed by the step-by-step description of the built temperature model, concentration model and dose distribution model, including assumptions and simplifications. Lastly, all physical properties and variables are specified.

### 3.1. Finite Element Method as Numerical Approach

The software program used to build and run the diffusion and temperature models for the project is Matlab (by 'The MathWorks, Inc.'). It is a programming and numeric computing software used to analyze data, develop algorithms and create models [67]. Within the software the 'Partial Differential Equation Toolbox' (PDE Toolbox) is included, which is the main package used for the project. The PDE Toolbox is a solver for partial differential equations (PDEs) in both 2D and 3D using the Finite Element Method (FEM) [68]. In Figure 3.1 a block scheme of the FEM approach is given.

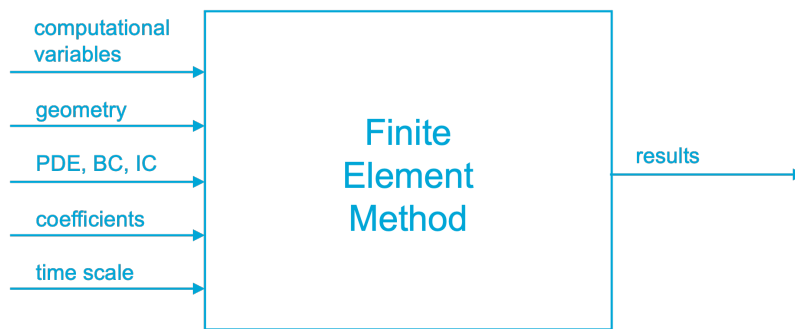


Figure 3.1: Block scheme of the Finite Element Method. It shows on the left the variables that are required input to solve the problem. On the right hand side it is shown that the results are the output of the solved problem.

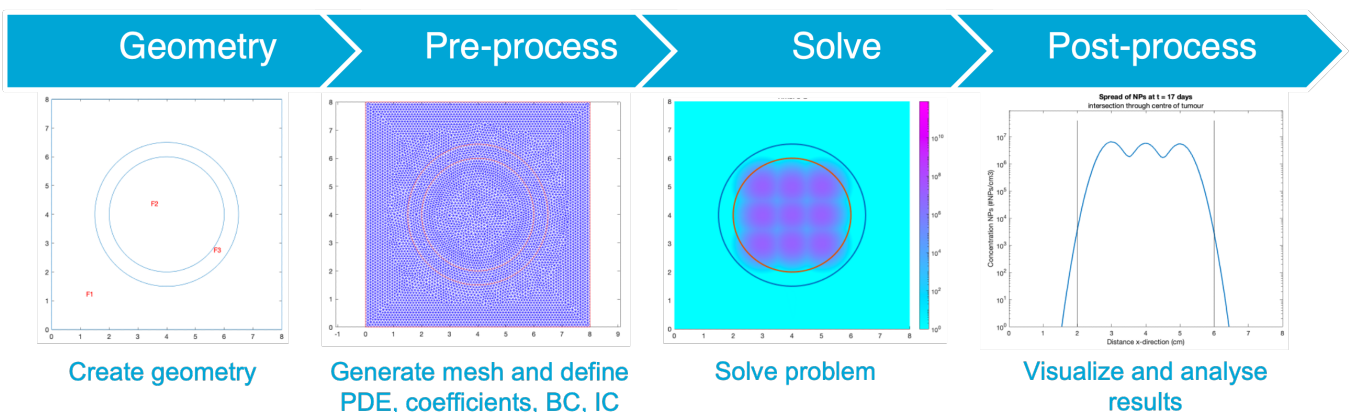


Figure 3.2: General overview of the process steps of the built temperature and concentration models. The phases are based on the required steps for the FEM approach described in Section 3.1.

The Finite Element Method can be used to calculate static and time dependent problems of systems of PDEs, e.g. diffusion and heat transfer problems. An overview of the process of the FEM approach is given in Figure 3.2. These process steps are based on the numerical steps taken within the FEM approach to solve a time dependent problem are:

1. Create a geometry in 2D or 3D, forming the computational domain representing the control volume;

2. Create a mesh: divide the geometry into smaller elements, mesh elements. Each element is described by its mesh vertices (X, Y, (Z) coordinates of element nodes);
3. Set up a general PDE for the system and define the coefficients for each element. The coefficients depend on the problem type and terms included in the PDE.
4. Formulate boundary conditions (BCs) and initial conditions (ICs) for each element;
5. Define the time scale over which the problem must be calculated and solve the system of PDEs for each time step.
6. Interpret the outcomes visually by plotting the results of the PDEs.

To solve a system of PDEs over the domain of interest, the Matlab built-in function 'solvepde' is used. First, a geometry is created, computational domain  $\Omega$ , which is then divided into triangles (2D) or tetrahedra (3D), which will form a mesh of smaller triangular subdomains. Simple PDEs on complex geometries must be discretized on the mesh elements to find discrete solutions. The toolbox starts with the time-dependent equation in the form:

$$d \frac{\partial u}{\partial t} - \nabla(c \nabla u) + a \cdot u = f, \quad (3.1)$$

with  $d$ ,  $c$ ,  $a$  and  $f$  being problem specific coefficients. The first term is the first order time derivative of the quantity of interest and the second term represents the second-order space derivative. The right hand side of the equation represents the source term. The definition of the terms in Equation 3.1 depends on the problem they describe. The coefficients  $d$ ,  $c$ ,  $a$  and  $f$  can be scalars, but also a function of  $u$  or partial derivative of  $u$ . Solving this partial differential equation mathematically in 2D would yield an equation for  $u(x,y,t)$ , which represents the quantity of interest as a function of time and space. For the heat problem, this quantity is temperature ( $T$ ), where for the diffusion problem, it is the concentration ( $c$ ). To numerically solve Equation 3.1, which is called the strong formulation, it is integrated to derive the weak formulation from it. This is done by multiplying both sides with the test function  $\phi_i$  and integrating over the domain  $\Omega$ . The test function  $\phi_i$  is a location specific function that has value 1 at location  $i$  and is 0 at all other locations. This concept is schematically visualized for a 1D situation in Figure 3.3. The weak formulation describes for each location a solution of  $u_i$ , which is only true at that location, because when multiplied by the location specific test function  $\phi_i$ , the solution is only defined at location  $i$ . The weak formulation of a PDE cannot be solved numerically over the whole domain  $\Omega$ . Therefore, it is required to define sub-domains called finite elements, by discretizing the domain. The solution per element  $u_h$  is then approximated with element-specific polynomials  $u_h^j$ , using linear basis functions  $\phi_h$ . The piecewise solution is approximated by:

$$u_h(x,y,t) = \sum_{j=1}^N u_h^j(t) \cdot \phi_h^j(x,y,t), \quad (3.2)$$

where  $h$  represents a specific sub-domain, i.e. a mesh element,  $j$  represents a mesh node of that element and  $N$  is the total number of mesh nodes per element [69].  $u_h^j$  is the solutions per mesh node, and  $\phi_h^j$  are the node specific basis functions, which have a specific value at node  $j$  and are 0 at all other nodes. The element specific solutions  $u_h$  are substituted into the weak formulation and projected on the test functions by interpolation, creating a system that can be expressed as matrix-vector system:

$$M \frac{dU}{dt} + KU = F, \quad (3.3)$$

where  $M$  is the mass matrix,  $\frac{dU}{dt}$  the time derivative of  $U$ ,  $K$  the stiffness matrix and  $F$  the load vector. This system is solved, resulting in the desired solution  $U$ . This matrix contains for each time step the coefficients  $u_h^j$  that correspond to the value of the approximate solution at mesh node  $j$  [68]. This method of numerically solving a PDE is used to determine the temperature and concentration profiles over time, which is more elaborately explained in Sections 3.2.2 and 3.2.3.

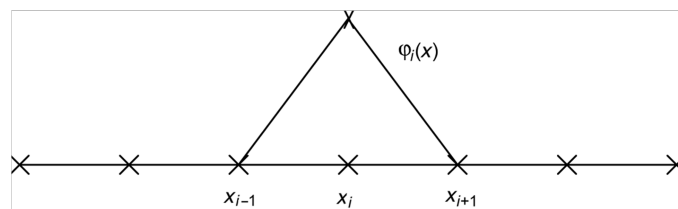


Figure 3.3: One dimensional representation of a test function  $\phi_i$ , showing it has a non-zero value at  $x_i$ , resulting in a linear relation over  $x$  between  $x_{i-1}$  and  $x_{i+1}$ .

## 3.2. Main Simulation Steps of Built Models

The structure of the built models is based on the steps required for the FEM approach described in Section 3.1. Steps 1 and 2 are similar for both the temperature and concentration model and thus described generally in Section 3.2.1. Steps 3 to 6 are model specific, due to the use of different quantities of interest ( $T$  and  $c$ ), PDEs, BCs, ICs and time scales. Therefore, both models are considered separately in Sections 3.2.2 and 3.2.3. Lastly, the dose calculations performed on the concentration results are described in Section 3.2.4. The design choices in the form of assumptions or simplifications are explained and justified in these sections.

### 3.2.1. Defining Geometry and Subdomains

The first two steps in the FEM approach are to create a geometry and to convert it into a mesh. The geometry is the total domain over which the problem is set up and must have the same dimensions and shape of the volume of interest. The goal is to apply the proposed treatment to human patients with early stage breast cancer, making the ultimate target geometry equal to a 3D breast image of a specific patient. However, at this stage of the computational simulation of the therapy, a simplified basic geometry is used, to be able to first build a general simplified model. The 3D basic geometry, visible in Figure 3.4a, is a hemisphere containing a spherical tumor of 4 cm diameter created in 'FreeCAD' and imported into Matlab. This geometry is then simplified by creating a 2D geometry (Figure 3.4b) in Matlab, after which a cutout is made of the breast including the tumor and a part of the surrounding breast tissue (Figure 3.4c). This is justified, seeing that the goal of the treatment is to not have temperature or nanoparticles spread (far) outside the tumor, making the breast tissue further outside the tumor unnecessary to include. The tumor is then divided into two subdomains. The first is the GTV (diameter  $d = 4$  cm), which is the area of interest for the thermal ablation part of the treatment, and the second the PTV (diameter  $d = 5$  cm), which is the area of interest for the radiation part. Since the simplified tumor is spherically symmetric, Figure 3.4c represents every intersection through the centre of the 3D tumor. Only this geometry is used throughout the project to generate the results found in Chapter 4.

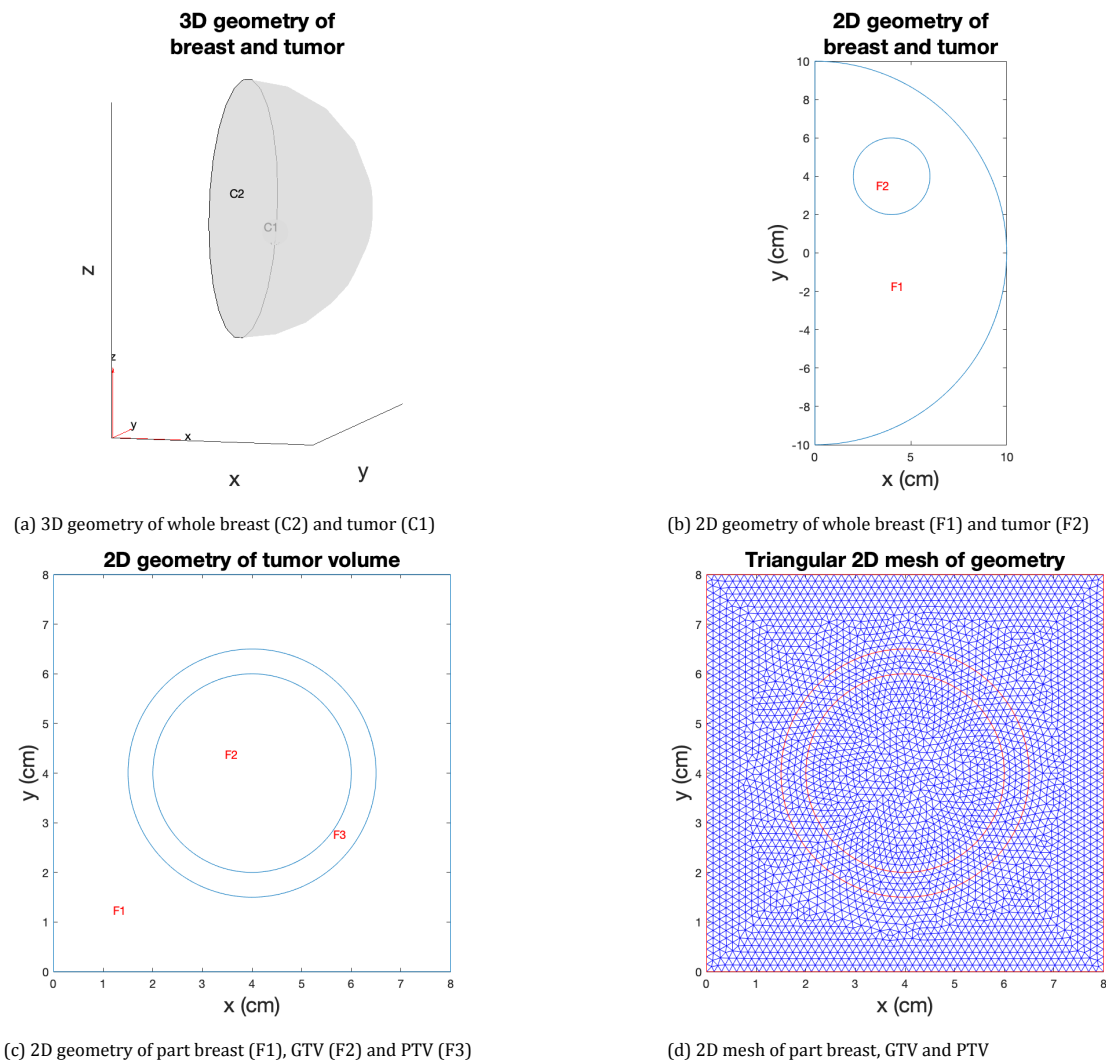


Figure 3.4: Overview of different geometries of a breast with in 3D, 2D and a cut-out of the 2D geometry. Also the discretized mesh of the geometry in 3.4c is given.

Figure 3.4c shows the domain over which the PDEs problems need to be solved using the FEM approach. This domain is divided into three subdomains, namely the GTV, the PTV and the breast tissue surrounding the tumor. These subdomains are discretized into smaller mesh elements. For 2D geometries these mesh elements are triangles of which the vertices are called mesh nodes. The size of the mesh elements can be fixed to a minimum or maximum. The size of the mesh elements determines the level of detail in the geometry, but also influences the running time of the model. The seeds are assumed to have a diameter  $d = 2$  mm and length  $l = 5$  mm, as previously described in Section 2.4.1 and visible in Figure 3.5c). Based on the size of the seeds and a sensitivity analysis on the running time, the maximum length of the sides of an element ( $h_{max}$ ) is set to be 0.5 cm. An example of the mesh grid of the used geometry (Figure 3.4c) is visible in Figure 3.4d).

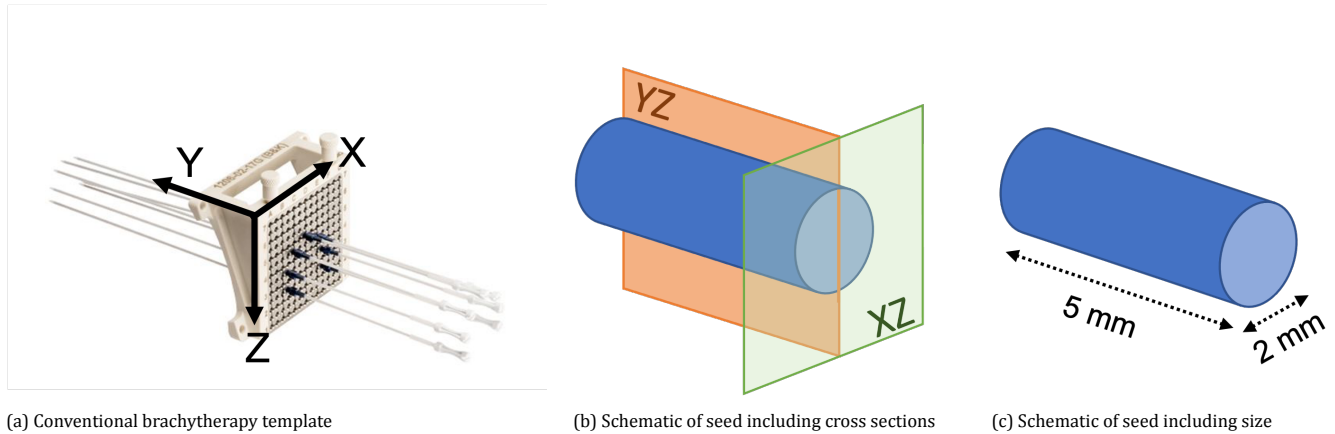


Figure 3.5: (a) The brachytherapy template is used for implantation of the seeds. The grid of holes determine the seed locations in X and Z directions. The seeds are implanted within the tumor with needles that fit the holes in the template. (b) A nanoparticle seed including XZ and YZ planes; (c) The nanoparticle seed including its sizes in diameter and length.

The implanted seeds containing the nanoparticles are not taken into account as subdomains of the geometry, but are defined as locations within the subdomains where certain properties are different. In the temperature model the seeds are implemented as location specific heat sources and in the concentration model the seeds are implemented by assigning an initial concentration of nanoparticles in the seeds to the seed locations as initial conditions. The seed locations are predefined during building the model and have been optimized for treatment planning to fulfill the goals described in Section 2.4. The locations of the seeds are defined in three dimensions. Due to the fact that the seeds are assumed cylindrical, the seed locations are not symmetric in all directions. Figure 3.5b shows the two intersection planes through a seed that are analysed within the project, namely the XZ and YZ planes. The locations where the seeds can be implemented in the XZ plane are limited by the grid of the brachytemplate used during the implantation procedure. This template has a fixed distance between the injection points, either 5 mm or 10 mm, meaning the distance between the seeds in X and Z direction is fixed. The seed injection points form the basis of default seed locations of the XZ plane, as the location possibilities are limited by the injection template, visible in Figure 3.5a).

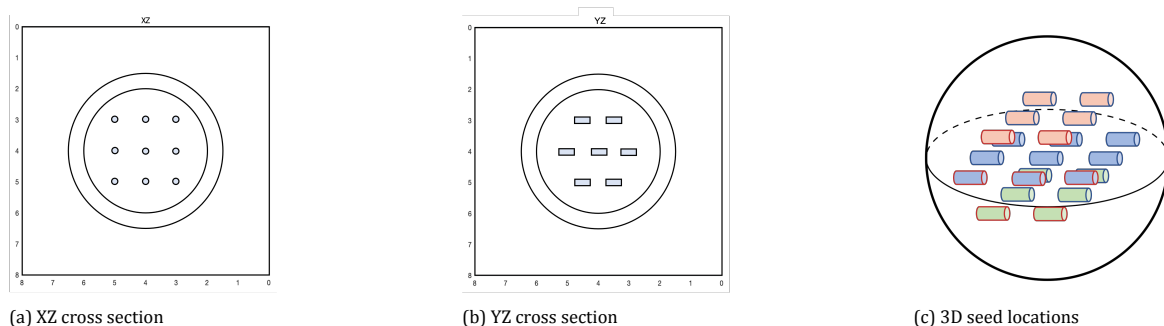


Figure 3.6: Default seed locations for (a) the XZ plane and (b) the YZ plane in 2D. (c) The 3D seed locations in a spherical tumor. The seeds are positioned inside the GTV (smallest circle), which is surrounded by the PTV (larger circle) and the breast tissue.

The seed locations for the YZ plane have more degrees of freedom, since the depth at which the seeds are implanted can be modified, meaning the the seeds are not fixed in the Y dimension. However, the distance between the seeds is fixed, because, to be able to separate the seeds, there is a spacer placed between the seed within the injection needle. This distance is equal to the length of the seeds (Figure 3.5c), making the distance between the seeds in the Y direction 5 mm [21]. The default seed locations with which the model is tested are shown in Figure 3.6b). The difference in depth between the neighbouring rows is to create a more homogeneous distribution of either temperature or concentration. To make sure the results of the models would be relevant, the seed locations were based on the concentration results.

It was investigated for what seed locations in both XZ and YZ planes the nanoparticles would spread through the tumor tissue, but would not diffuse too far out of it, within 17 days. This led to the default seed injection points in the XZ plane and YZ plane, shown in Figures 3.6a and 3.6b, respectively. Figure 3.6c shows the seed locations in 3D, but since the models are in 2D, the distributions are investigated for both XZ and YZ intersections of the tumor to gain knowledge on the distribution profiles in different directions.

### 3.2.2. Temperature Distribution Calculation

The 2D temperature model is built to find the temperature profile of the heated nanoparticles over time. The used PDE is based on the equation that describes the general energy balance (Equation 2.7), but is simplified to:

$$\rho c_p \frac{\partial T}{\partial t} - k \nabla^2 T = \omega_b c_b (T_b - T) + Q_{NP}, \quad (3.4)$$

where the metabolic heat is neglected. Connecting Equation 3.4 with Equation 3.1, the equation implemented into the model has the following structure:

$$d \frac{\partial u}{\partial t} - \nabla(c \nabla u) = f, \quad (3.5)$$

where  $d$  is the coefficient of the time dependent term being equal to  $\rho c_p$ . Coefficient  $c$  represents the tissue specific thermal conductivity  $k$ . The right hand side of Equation 3.4 is the sum of all heat sources, represented with  $f$ . As explained in Section 3.1, coefficient  $f$  can be a function of  $u$  and since the blood perfusion term is interpreted as a heat sink, source coefficient  $f$  includes the blood perfusion.  $Q_{NP}$  is the heat generated by the nanoparticles and is dependent on the Specific Absorption Rate (SAR) value of the nanoparticles and nanoparticle concentration in the seed (See Equation 2.6). Variables  $\rho$ ,  $c_p$ ,  $k$  and  $Q_{NP}$  are all assumed constant. For  $Q_{NP}$  this means the heating up and cooling down of the nanoparticles are neglected. The SAR value of the nanoparticles is assumed constant, because the magnetic field cannot be changed through the tumor volume. The whole tumour will have an equal amount of magnetic radiation, because the magnetic field is too wide and cannot be narrowed down to the order of magnitude of the tumor [70]. To have different heating power through tumor, either the concentration of nanoparticles must be changed or the magnetic field strength.

The blood perfusion term, however, is more complex. Within the term, the blood temperature  $T_b$  and blood specific heat  $c_b$  are assumed constant for each node, while the time dependent temperature is not constant. The exact relation between temperature and blood perfusion rate  $\omega_b$  is not known, except that it is not constant. It is tissue specific, with two different possible values for tumor tissue. It is assumed in the model that the tumor tissue is fully viable. This simplification is made, because the size of the necrotic core is patient specific and can therefore not be generalized. The influence of the necrotic tissue on the temperature distribution is investigated in Section 4.2.1, as well as the temperature and time dependence of the blood perfusion rate. The sensitivity analysis will show the influence of the different blood perfusion rate equations on the temperature results. Lastly, the convective term is neglected in Pennes' bioheat equation, as stated in Section 2.5.1.

To be able to use the Matlab PDEToolbox, only the boundaries at the outer edges of the geometry need to be defined. There are two types of boundaries, namely the boundaries between the interior and the exterior of the geometry and boundaries between subdomains. The latter is not specified for FEM, even though coefficients are discontinuous between subdomains [68]. In the case of the geometry in Figure 3.4c only the boundary conditions at the four sides of the healthy tissue need to be specified. There are two types of boundary conditions defined in Matlab, being the Dirichlet or generalized Neumann boundary conditions. The Dirichlet boundary condition specifies the value that the unknown function needs to maintain along the boundary of the domain. This means that the boundary has a fixed value. The second, the Neumann boundary condition, specifies the flux, i.e. the derivative of the unknown solution, over the boundary. Because heat is transferred through tissue and thus can also be transferred to tissue outside the control volume, the boundary condition can be described with an outgoing heat flux over the boundary. The boundary condition type for the temperature model is therefore specified as the Neumann boundary condition. Since convection is neglected within Pennes' bioheat equation, the boundary flux is described by the outgoing conductive flux  $\vec{q}_{out}''$  [W/cm<sup>2</sup>]. This flux can be described with, for example at the left boundary of geometry in Figure 3.4c at  $x = 0$ :

$$\vec{q}_{out}''(x,y,t) \Big|_{x=0} = -k \frac{dT(x,y,t)}{dx} \Big|_{x=0}, \quad (3.6)$$

where  $k$  is the conduction coefficient [W/(cm·°C)] and  $\frac{dT}{dx}$  the temperature gradient over the boundary at  $x = 0$  in the  $x$ -direction [°C/cm]. This boundary condition is specified for all four geometry boundaries of the 2D geometry.

In the next part of the model, the initial condition for each mesh node is defined. The initial condition must represent the initial body temperature at a specific location. The initial temperature of tissue is assumed 37°C for both tumor an

healthy tissues, which is equal to the generally accepted average normal body temperature [71].

The total time for which the temperature profile is simulated, is 60 minutes. This includes 20 minutes of heating with the alternating magnetic field and 40 minutes of cooling down of the system. To obtain accurate results within a reasonable running time, the influence of the time step size to the results was analysed, after which a step size of 0.1 minutes is selected. There was no significant difference found in results if a shorter time step was used, but it did have a longer running time. This time step means that the temperature is calculated every 6 seconds for a total length of 60 minutes.

Within the model, the spread of the nanoparticles before  $t = 0$  min and during the 60 minutes of investigation, is neglected. Even though the nanoparticles can already diffuse out of the seeds during implantation time ( $t < 0$  min) and during the thermal ablation treatment ( $0 < t < 60$  min), it is assumed that the nanoparticles remain at their initial locations. This can be explained by the small diffusion coefficient and these assumptions are supported by the concentration results after 60 minutes, given in Appendix C in Figure C.2b. Lastly, the warming up of the seeds is excluded from the process, meaning that at  $t = 0$  the heat spread by the seeds is already at its maximum. Finally, the model can start running to generate the results, being the temperature at each mesh node for each time step. The temperature results are then analysed, which can be found in Chapter 4.

### 3.2.3. Nanoparticle Concentration Distribution Calculation

The concentration model is built to find the concentration profile of the nanoparticles over time in 2D. The PDE used for the model is based on the equation that describes the general material balance (Equation 2.8), but is simplified to:

$$\frac{\partial c}{\partial t} - D \nabla^2 c = 0. \quad (3.7)$$

Equation 3.7 includes the time dependent term and diffusion term with  $D$  the diffusion coefficient [cm/s], but neglects the convection and source terms of the general PDE. The driving force of these last two terms is the vascular flow of blood and lymph fluid. As explained in Section 2.5.1, the vascular structure of the tumor tissue will be destroyed after thermal ablation. This results in a lack of convective flow of the nanoparticles in the ablated parts and lead to the removal of the convective and transvascular exchange terms in the PDE. For simplicity reasons this is done for the entire domain, so also for the viable tumor and healthy tissue. Translating these simplifications to Equation 3.1, the rearranged equation implemented into the model is:

$$d \frac{\partial u}{\partial t} - \nabla(c \nabla u) = 0, \quad (3.8)$$

where  $d$  is the time dependent coefficient being equal to 1. Coefficient  $c$  represents the diffusion coefficient  $D$ , which is assumed constant and is tissue specific. This means that the diffusion coefficient of each subdomain, being healthy tissue (F1), GTV (F2) and PTV (F3), is assigned to all mesh nodes within that domain. The values used for  $D$  can be found in Table 3.2. Furthermore, it is assumed that the nanoparticles diffuse uniformly through the tumor, resulting in a homogeneous spread of nanoparticles from the seed. However, Darvishi *et al.* argue that there are parameters that can influence this uniform spread of nanoparticles [72].

As explained in Section 3.2.2, only the boundaries at the outer edges of the geometry need to be defined. Again, only the boundary conditions at the four sides of the healthy tissue in Figure 3.4c need to be specified. For the concentration model the boundary conditions are of the Neumann type, because the concentration of the nanoparticles is not fixed but depends on the outward flux of nanoparticles  $J$  over the boundary. The concentration flux over the left boundary at  $x = 0$  can be described by:

$$\vec{J}_{\text{out}(x,y,t)} \Big|_{x=0} = -D \frac{dc(x,y,t)}{dx} \Big|_{x=0}, \quad (3.9)$$

where  $D$  is the diffusion coefficient and  $\frac{dc}{dx}$  is the concentration gradient over the boundary at  $x = 0$ . This boundary condition is specified for all four geometry boundaries of the 2D geometry.

In the next part of the model, the initial condition for each mesh node is defined. The initial condition must represent the initial concentration of nanoparticles at a specific location. The initial concentration of material is zero at all places except at the seed locations. The seeds are not included in the geometry, but are separately defined as explained in Section 3.2.1. The initial concentration is equal to the concentration of nanoparticles in the seed and is assigned to the mesh nodes that lay within the seed volume. For the XZ plane this means that all nodes within seed diameter distance from the predefined seed centre get assigned the initial concentration and for the YZ plane all nodes within the area of the intersection through the seeds get assigned the initial concentration. The seeds are implemented within the tumor by

the initial conditions.

Total time that the diffusive behaviour of the nanoparticles is checked is 17 days, which is equal one half live of Pd-103. To obtain accurate results within a reasonable running time, the influence of the time step size to the results was analysed, after which a step size of 1 hour is selected. The nanoparticle distribution is thus calculated per hour for a total length of 17 days. At  $t = 0$ , all seeds have already been implanted, and similar to the temperature model, the diffusion of nanoparticles during implantation time is neglected. Since the implantation procedure time is expected to be less than an hour and the diffusion of the nanoparticles is proven to be negligible for the first 60 minutes (See Figure C.2 in Appendix C), the change in outcome is assumed insignificant compared to the total time scale. After defining the time step and scale, the model can start running to generate the results, being the concentration at each mesh node for each time step. The results of the relevant concentration distribution can be found in Appendix C.

### 3.2.4. Dose calculation

The dose absorbed by the material is calculated using the dose rate at a specific location delivered by the nanoparticles surrounding it and is based on the radial dose distribution of a single radioactive nanoparticle (see Figure 2.9). This dose distribution is transformed into a 2D dose distribution for a single nanoparticle and is scaled to a nanoparticle activity relevant for this project, based on the activity of a brachyseed currently used in the clinic (70 MBq) [3]. This is done by circular interpolating of the radial dose distribution, taking the radial distance as the radius of the 2D interpolated circle. Subsequently, the interpolated 2D dose distribution of a single nanoparticle is converted to a voxel based grid of 0.05 by 0.05 cm, visible in Figure 3.7. Similarly, the results of the concentration model are converted from a triangular mesh grid to a voxel based grid of the same voxel size. The dose distribution is evaluated per time step, being one hour.

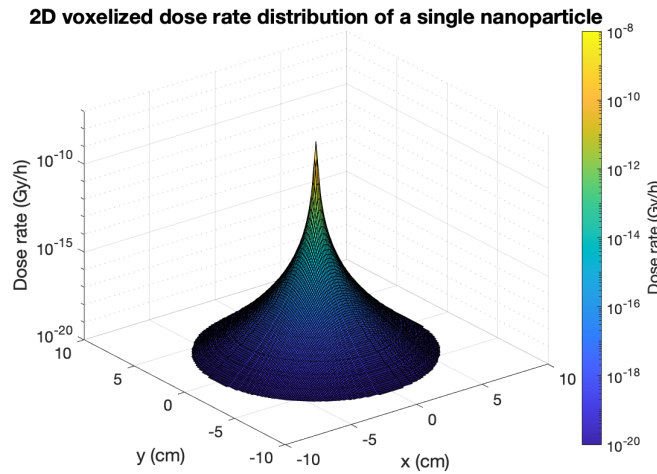


Figure 3.7: Voxelized 2D dose rate distribution of a single nanoparticle. Based on the radial dose distribution in Figure 2.9, which is first interpolated to 2D and then converted into a voxel mesh grid of size 0.05 by 0.05 cm.

Each concentration voxel with a concentration of nanoparticles higher than zero is taken as a radioactive point source. This way only the locations that deliver dose to their surroundings are included. Then for a specific voxel with centre  $r_i$ , the total dose received is calculated per time step,  $D_i(r_i, t, \Delta t)$ . This is done by evaluating the dose delivered by each concentration voxel with non-zero nanoparticle concentration with centre  $r_j$ , multiplied by the number of nanoparticles within that voxel and the exponential decay factor at time  $t$ . To ultimately calculate the delivered dose per time step, the sum over all voxels  $v$  delivering dose to location  $r_i$  is multiplied by the time step. This calculation is described by equation:

$$D_i(r_i, t, \Delta t) = e^{-\lambda t} \sum_{j=1}^v \dot{D}_{ij}(\vec{r}_{ij}) \cdot c_j(r_j, t) \cdot S \cdot \Delta t, \quad (3.10)$$

where  $\lambda$  is the decay factor [1/s],  $t$  is the time passed since  $t=0$  [s] and  $\Delta t$  is the time step size, being 1 h. The sum is taken over all voxels  $v$  having non-zero nanoparticle concentration. Per voxel the dose rate  $\dot{D}_{ij}(\vec{r}_{ij})$  [Gy/(h·NP)] is evaluated by calculating the distance between  $r_i$  and  $r_j$ . Because the used dose distribution is for a single nanoparticle, the dose rate is multiplied by the number of nanoparticles present in voxel  $j$ . This number is found by multiplying the nanoparticle concentration  $c_j(r_j, t)$  [#NP/cm<sup>2</sup>] with the 2D voxel volume  $S$  [cm<sup>2</sup>], which is equal for all voxels. The calculations in Equation 3.10 are done for each voxel and for each time step. Finally the dose is accumulated for every time step to find the total cumulative delivered dose.

The time between the radionuclide production, the synthesis of seeds, the injection procedure and the start of the treatment is not taken into account, meaning that the radio-isotopes have decayed for some time before the nanoparticles start to diffuse. This influences the decay factor and thus the radioactivity of the nanoparticles, but does not influence the dose distribution profile as it gives the relative dose and not the absolute.

The concentration distribution per time step is used to calculate the delivered dose per time step. By accumulating the delivered doses per time step, a total cumulative dose distribution through the tumor is obtained after 17 days. To reduce simulation time, the remaining dose, deposited in the period after the first half life, is calculated using the last concentration distribution of nanoparticles after 17 days. This is multiplied by the number of time steps up to 85 days, being the end of the fifth half life period. After five half lives the remaining activity is only 3.1%, adding negligible dose from that point on to the total cumulative dose. The delivered dose per region depends on the concentration of radioactive nanoparticles, the diffusion rate through the tissue and to the total activity of the nanoparticles. First, for a higher number of nanoparticles, i.e. a higher initial concentration or more seeds, the total cumulative dose will be higher. For higher diffusion rate, the nanoparticles are spread more homogeneously over the tissue, resulting in a more homogeneous dose distribution. This will not change the total cumulative dose over the whole volume, but only the local cumulative dose. The last parameter, the activity, determines the dose as a function of distance from the centre. The activity linearly increases or decreases the total dose.

### 3.3. Physical Properties and Variables

To describe the behaviour of the material during the treatment, several constants and material properties need to be known. These properties are found in literature and are assembled in Tables 3.1 and 3.2. The properties are divided into the mass transfer and the heat transfer. The table also includes variables required for the calculations. As described in Section 2.1, breast cancer most commonly starts in the glandular tissue instead of the fatty tissue. Therefore the values used for breast tissue properties are of glandular tissue.

Table 3.1: Default parameter values for temperature model. All parameters extracted from temperature properties review executed by Camilleri *et al.* [4]. Specific absorption rate, concentration fraction and nanoparticle heat source determined during project execution.

Heat coefficients and variables	Symbol	Unit	Breast		Tumor		Blood	NPs	NP seeds
			fat	gland	viable	necrotic			
Density	$\rho$	g/cm <sup>2</sup>	0.93	1.07	1.07	1.07	-	-	-
Specific heat capacity	$cp$	J/g·K	2.22	3.40	3.61	3.61	3.62	-	-
Thermal conductivity	$k$	W/cm·K	1.71E-3	3.28E-3	5.11E-3	5.11E-3	-	-	-
Blood perfusion	$\omega_b \cdot c_b$	W/cm <sup>2</sup> ·K	3.21E-3	3.21E-3	1.75E-2	0	-	-	-
Blood perfusion rate	$\omega_b$	g/s·cm <sup>2</sup>	8.86E-4	8.86E-4	4.83E-3	0	-	-	-
Specific absorption rate NP	$SAR_{NP}$	W/g	-	-	-	-	-	100	-
Concentration fraction NPs in seed	mass%	-	-	-	-	-	-	-	0.1
Heat NPs	$Q_{NP}$	W/cm <sup>2</sup>	9.32	10.66	10.66	10.66	-	-	-
Initial temperature	$T_i$	K	310.15	310.15	310.15	310.15	310.15	-	-

Table 3.2: Default parameter values for concentration model

Material coefficients and variables	Symbol	Unit	Breast		Tumor		NP seeds
			fat	gland	viable	necrotic	
Density [4]	$\rho$	g/cm <sup>2</sup>	0.93	1.07	1.07	1.07	-
Diffusion coefficient [6, 73]	$D$	cm/s	1.63E-5	1.63E-5	2.20E-8	2.20E-8	-
Initial concentration [3, 5, 58]	$c_i$	#NP/cm <sup>2</sup>	-	-	-	-	7.97E+9

# 4

## Results and Discussion

This chapter describes the results gained during the project. First the initial results from the temperature and concentration models are given in Section 4.1. The temperature, concentration and dose models are used to study the behaviour of the nanoparticles in the human body, using properties from literature. This includes the temperature and dose distribution results in the XZ and YZ planes. Secondly, a sensitivity analysis is done to evaluate the impact of the input variables to the outcome of the model for the XZ plane, included in Section 4.2. This is done for the physical properties and variables first. Subsequently, variables that are adjustable during treatment planning are analysed by finding the sensitivity of the treatment outcome to these variables. Lastly, treatment optimization is discussed. since the models can be used for optimization of the adjustable variables for treatment planning too. The sensitivity analysis is done for the XZ plane of the 2D geometry in Figure 3.4c and the optimisation for the YZ plane as well.

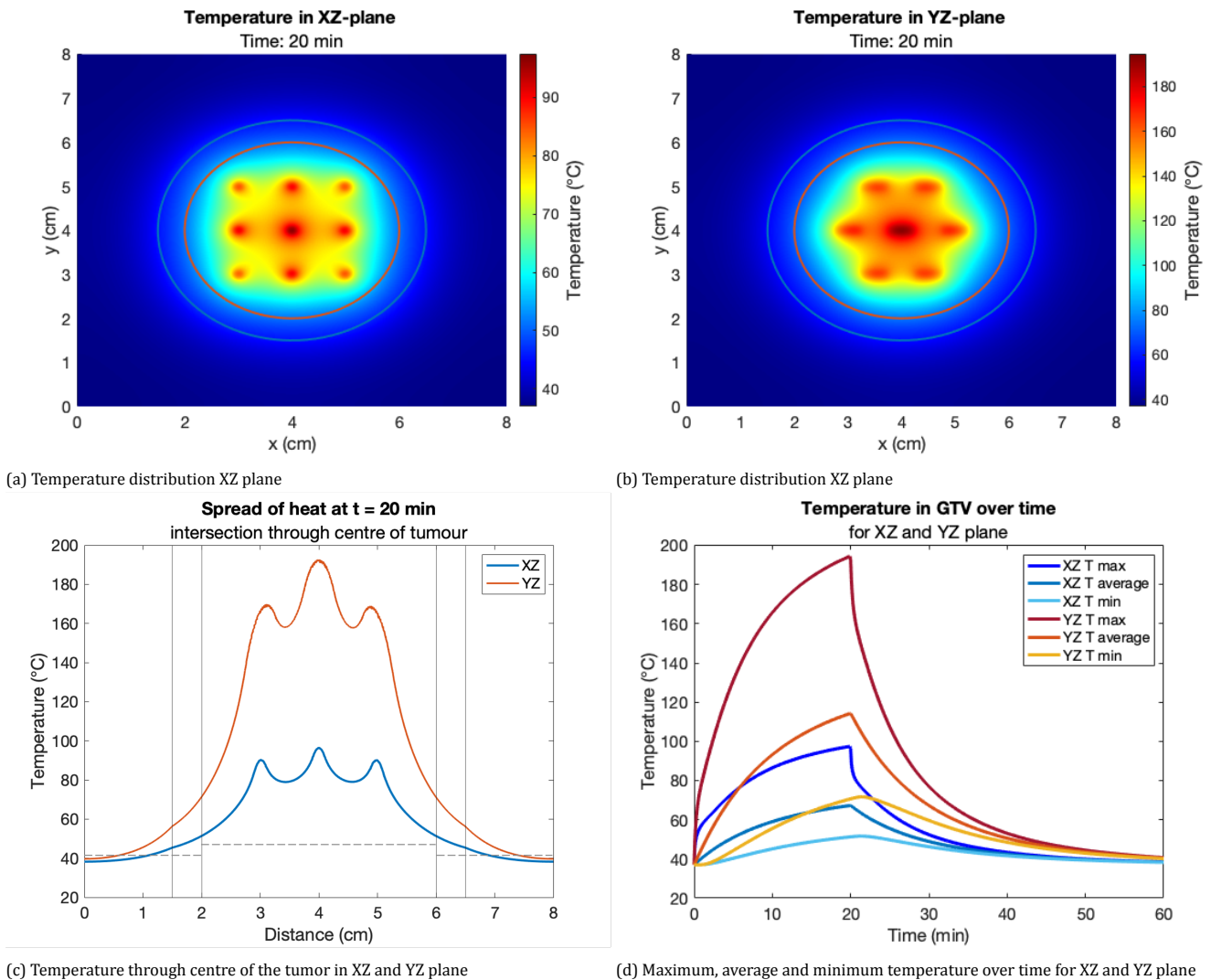


Figure 4.1: Temperature results of default settings. Temperature distribution profiles after 20 minutes (a) in XZ direction and (b) YZ direction. (c) Temperature intersection profile through the centre of the tumor, for the XZ (blue) and YZ (orange) planes. The vertical lines indicate the outer shell of the GTV and PTV. The dotted horizontal lines indicate the limits to fulfill the treatment requirements. (d) Maximum, minimum and average temperatures in the GTV over time for both XZ and YZ planes.

## 4.1. Reference Results using Default Parameters

The temperature and dose distribution are simulated using the default properties and variables given in Tables 3.1 and 3.2 and using the default seed locations given Figure 3.6. These results are considered the reference case, for the sensitivity analysis in Section 4.2.

### 4.1.1. Default Temperature Distribution

The temperature distribution results after 20 minutes of heating the nanoparticles are gained using the temperature model. For the thermal ablation to be successful, the temperature distribution must meet the following requirements:

1. The minimum temperature within the GTV must reach a temperature of 48°C,
2. The maximum temperature within the area surrounding the PTV must not reach temperatures higher than 45°C.

The default temperature profiles for the XZ and YZ planes are generated and visible in Figures 4.1a and 4.1b. The intersection graph of both the XZ and YZ planes is visible in Figure 4.1c and Table 4.1 gives the maximum, minimum and average values in three areas of interest. It is shown in the Figures 4.1a and 4.1b that the heat spreads homogeneously from the seeds, which can be explained seeing that the tumor tissue specific heat properties are assumed constant within the GTV and PTV. This is physically not the case, having influence on the homogeneity of the heat spread. In reality, the distribution would be influenced for example by part of the tumor being more dense or having a different blood perfusion. This can lead to a more heterogeneous distribution. However, the heat properties are different between tumor tissue and healthy tissue, explaining the discontinuities in temperature gradient at 1.5 cm and 6.5 cm in Figure 4.1c, both representing the interface between the PTV and the healthy tissue.

Furthermore, the temperature of the centre seed is higher than that of the surrounding seeds, visible in Figure 4.1c. This is because the centre seed cannot lose its heat properly to its surroundings, since it is surrounded by other seeds. The centre seed has a smaller temperature difference between its peak and the temperature sinks at 3.5 cm and 4.5 cm, than e.g. the left seed with the tissue at 2.5 cm. Figure 4.1d shows the maximum, minimum and average temperature in the GTV over time, for both XZ and YZ planes. The maximum temperatures over time represent the centre seeds. After switching off the AMF at 20 minutes, the temperature in the centre decreases fast at first to its surroundings. However, within one minute the temperature difference between the centre seed and the outer seeds is decreased, resulting in a smaller temperature difference at the centre with its surroundings and thus smaller temperature gradient driving heat conduction. From this time on, the temperature decreases slowly in the centre following the course of the parabolic temperature peak. This behaviour is visible in Figure B.1 in appendix B. This partly explains the anomaly in temperature gradient in Figure 4.1d between 20 min and 21 min. Another reason for this discontinuity is the time step. Because the temperature gradient decreases strongly within one minute and the time step is 6 seconds, the graph does not show a continuous line.

The requirements are tested using the calculated maximum, average and minimum temperature in the different areas, being the GTV core, the PTV surrounding it and in the area of 1 cm surrounding the PTV. The second requirement of the thermal treatment is not met when interpreting these results, even though the first requirement is. The XZ plane shows a minimum temperature in the GTV after 20 minutes of 51.2°C, which is higher than the required 48°C, meaning the temperature in the whole GTV is higher than 48°C in the XZ plane. This is also the case for the YZ plane. However, the maximum temperatures in the area of 1 cm surrounding the PTV show maximum temperatures of 46.9°C and 58.5°C in the XZ and YZ planes, respectively. These are higher than 43°C, meaning that the second requirement is not met.

### 4.1.2. Default Cumulative Delivered Dose Distribution

The dose distribution results after 84 days are gained using the concentration and dose calculation models. The required cumulative dose used to determine the minimum concentration of nanoparticles through the tumor is 60 Gy. The requirements for a successful treatment are the following, as it is essential that all cancerous cells are destroyed by the radiation:

1. The minimum cumulative dose within the PTV must reach a minimum of 60 Gy;
2. The maximum cumulative dose outside the PTV must not reach a dose higher than 60 Gy.

The reference dose distribution is calculated using the concentration distribution results for which the default properties stated in Table C.1 were used. The cumulative dose results are visualized in Figure 4.2. Figures 4.2a and 4.2b include contour lines of the 1 Gy, 15 Gy and 30 Gy dose received after 84 days, corresponding to 1.7%, 25% and 50% of the minimally required cumulative dose, respectively. As explained in Section 3.2.3, the concentration distribution is only calculated for the first half-life of Pd-103, being 17 days. This, however, includes only 50% of the radiation of the palladium-103 while the other 50% still will be emitted. Therefore, a rough estimate of the remaining dose is calculated, up to 85 days. This number represents the five half-lives, decreasing the activity to 3.1% of its initial value. For this calculation the concentration distribution at day 17 is used, neglecting the continuing diffusion of the nanoparticles. This estimate does provide a more accurate value for the total delivered dose, even though the dose distribution would in reality be spread wider.

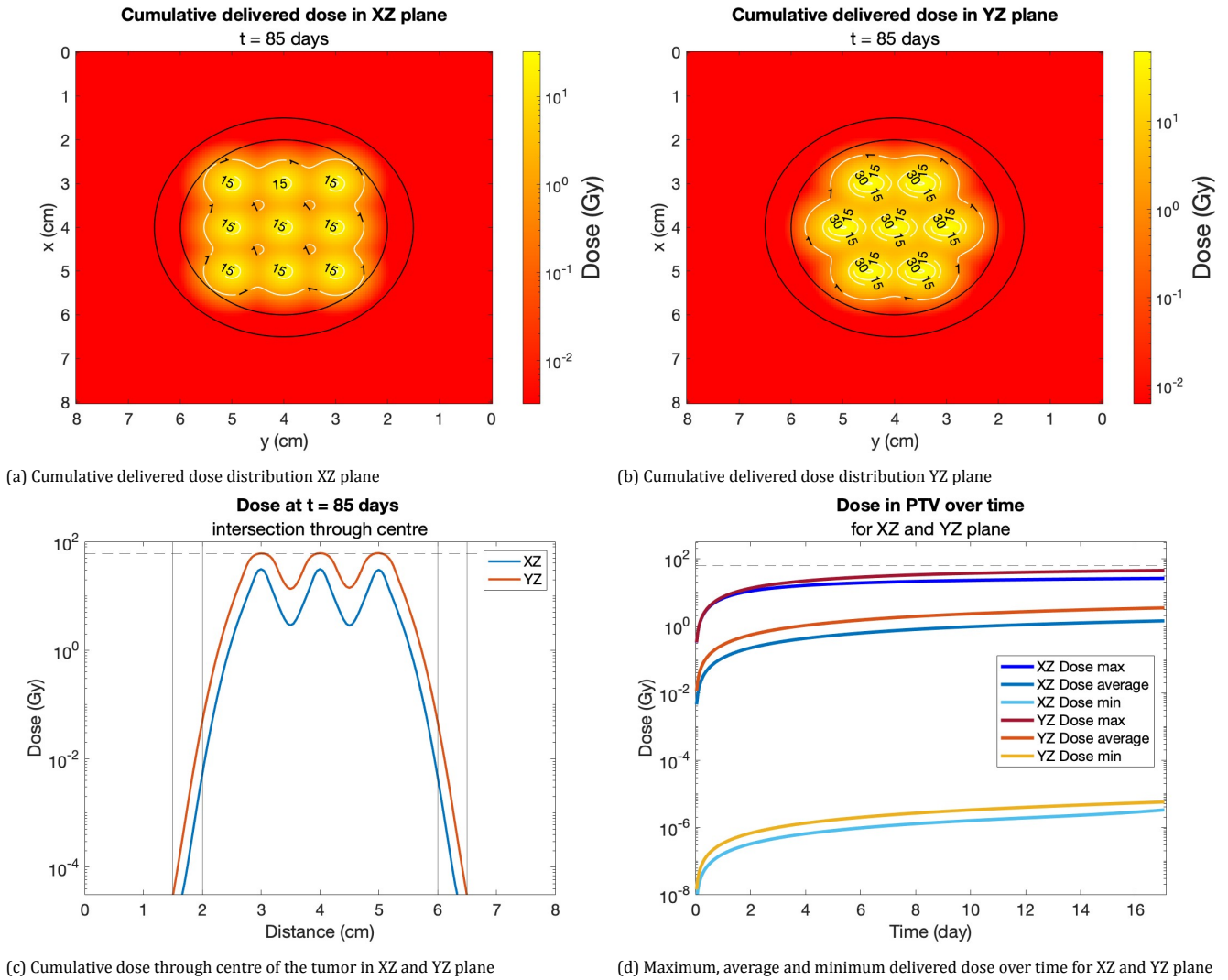


Figure 4.2: Cumulative dose results of default settings. Dose distribution profiles after 85 days (a) in XZ direction and (b) YZ direction. (c) Cumulative dose intersection profile through the centre of the tumor, for the XZ (blue) and YZ (orange) planes. The vertical lines indicate the outer shell of the GTV and PTV. The dotted horizontal line indicates the minimum required dose inside the PTV and the maximum dose outside the PTV. (d) Maximum, minimum and average dose in the GTV over time for both XZ and YZ planes. The maximum dose represents the centre seed, the minimum the edge of the GTV furthest away from a seed and the average is taken over the whole GTV.

The highest dose is delivered inside the seeds, reaching maximum doses up to 62.3 Gy in the YZ plane. This high dose compared to the dose delivered further away from the seed is mainly caused by the electrons that only have a range of a few micrometers [3]. For the XZ plane, the dose is spherically distributed around the seeds, resulting in a circular dose distribution per seed. In the YZ plane the cross-section of the cylindrical seeds is simulated, making the distribution in the tissue surrounding the seed slightly less spherical. Even though the dose delivered is not affected by neighboring nanoparticles, the concentration spread is influenced by nanoparticles surrounding it. Similar to the temperature distribution, the concentration gradient depends on the magnitude of the difference between two locations. This is the reason for the non-homogeneous dose distribution between seeds. Also, because the delivered dose at a specific location is a sum of all energy deposited at that location from its surrounding. The dose is higher at the locations closer to more seeds, for example between the seeds, as visible in Figure 4.2c. It is therefore suggested that the total cumulative dose distribution strongly depends on the seed locations.

Similar as in the temperature results, the difference in cumulative dose between the XZ and YZ plane is a result of the larger seed cross section in the YZ direction. The seeds contain more nanoparticles in the YZ direction than in the XZ direction, meaning more nanoparticles diffuse out and irradiate tissue in the YZ plane. This effect is observed in the maximum, minimum and average cumulative dose over time in Figure 4.2d, where the YZ dose is constantly higher than the XZ.

After 85 days the minimum delivered doses in the PTV area for XZ and YZ planes are  $1.37\text{E-}5$  Gy and  $1.38\text{E-}5$  Gy, respectively. Both values are a lot lower than the minimally required dose of 60 Gy, meaning that the first requirement is not met after 85 days. The maximum cumulative dose in the area surrounding the PTV after 85 days in the XZ and YZ planes, respectively, are  $3.75\text{E-}4$  Gy and  $5.52\text{E-}5$  Gy. This does meet the second requirement, though this requirement is meaningless if the first is not met. It is expected that, after optimization, the goal to create a perfect circular distribu-

tion around the seeds will not be achieved, especially in the YZ direction, which will lead to the maximum dose in the area surrounding the PTV being higher than the minimum inside the PTV. Considering this, it is suggested that the first requirement is identified as more important to satisfy, because total eradication of the cancer is essential to achieve full recovery and to decrease the chances of recurrence. Lastly, it is proven that by comparing both dose and temperature distributions, the dose part is limiting to the treatment. This can be concluded, because the temperature distribution is overshooting, while the dose distribution does not meet minimum dose requirement in the PTV.

Table 4.1: Results of default coefficients and parameters for temperature at  $t = 20$  min and delivered dose at  $t = 85$  days. It gives the maximum, average and minimum values of the parameters of interest within the GTV, PTV area around the GTV and the area of 1 cm outside the PTV.

Parameter of interest	Unit	GTV			PTV			PTV + 1 cm		
		max	av	min	max	av	min	max	av	min
XZ T	°C	97.4	67.2	<b>51.2</b>	54.9	48.9	45.3	<b>46.9</b>	41.3	38.8
YZ T	°C	194.4	114.2	<b>70.5</b>	75.1	63.8	56.2	<b>58.5</b>	46.6	40.6
XZ Dose	Gy	3.25E+1	4.17E+0	3.70E-3	6.35E-1	3.03E-2	<b>1.37E-5</b>	<b>3.75E-4</b>	1.93E-5	8.09E-6
YZ Dose	Gy	6.23E+1	1.02E+1	2.50E-3	9.19E-2	5.30E-3	<b>1.38E-5</b>	<b>5.52E-5</b>	4.79E-6	3.00E-7

## 4.2. Sensitivity Analysis

A sensitivity analysis is used to study uncertainties in model outputs as a result of uncertainties in model inputs. The aim of the sensitivity analysis is to investigate the influence of a parameter value of the models on the results. These parameters can be divided into physical properties and variables that cannot be adjusted and properties that can be adjusted to optimize the treatment. The sensitivity of the first category parameters is analysed by comparing the results to the minima and maxima of the properties found in literature or by switching on or off parts of the model. This way it is known what elements of the model or treatment have negligible impact and which properties need to be well known before starting the treatment. This is done for the temperature and concentration model separately. The second category parameters consists of the five adjustable variables that can be altered during treatment planning. Their effect on the results of both temperature and dose distribution are tested.

The sensitivity of the model to a certain variable is quantified using the sensitivity index (SI). The sensitivity index is calculated using the on-at-a-time method, where the results are a result of the change of a single parameter. The larger the sensitivity index, the larger the impact of change of the input variable on the results. It gives the percentage of change in the outcome variable as a result of the percentage of change in input variable:

$$SI = \frac{\Delta\%_{outcome}}{\Delta\%_{income}} \quad (4.1)$$

### 4.2.1. Sensitivity of Temperature to Model Parameters

As explained in Section 3.2.2, the temperature model is based on Pennes' bioheat equation (Equation 2.7). In this section the significance and effect of each term is evaluated. The first term in the equation is the time dependent term. Since the temperature changes over time, the system is time dependent and this term is required.

The default tissue types used in the model are homogeneous glandular breast tissue for the healthy tissue and fully viable tumor tissue. However, the tissues of interest differ per patient case. The breast tissue type depends on the original tissue where the cancer started growing. Breast cancer can start in the fatty tissue or glandular tissue, of which the last can be divided into lobular and ductal. Tumor tissue is split into viable and necrotic tissue, the main difference being blood perfusion rates. Additionally, the values found in literature (shown in Tables 3.1 and 3.2) vary, e.g. due to measurement inaccuracies and properties being patient specific. For breast tissue properties, the influence on the results of a variable is evaluated using the minimum and maximum values found in literature for all of the breast tissue types. This way the influence of the breast tissue type is tested. The influence of tumor tissue type is evaluated separately in the section of blood perfusion rate.

The impact of the variables are evaluated on the basis of influence on the temperature values and on the distribution of temperature. The first is investigated by calculating the maximum, average and minimum temperature in different areas of the geometry at 20 minutes and in the GTV over time. The first is used for calculating the sensitivity index. For the second criterion the distribution profile in 2D and the intersection through the centre of the tumor are used. The sensitivity analysis is executed only for the XZ plane.

#### Blood perfusion rate: Necrotic core

As explained in Section 2.5.1, the blood perfusion rate depends on tissue type, temperature and time. First, the tissue type dependence is evaluated. For different necrotic core sizes the temperature dependence is investigated, the diame-

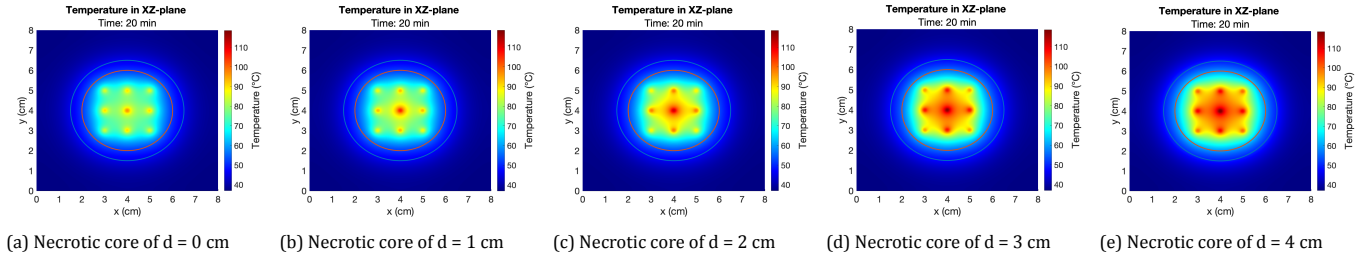


Figure 4.3: Temperature profiles in XZ plane after 20 minutes of all tested necrotic core diameters (0 cm, 1 cm, 2 cm, 3 cm and 4 cm). The colormap axis is the same for all diameters, its maximum being equal to the maximum temperature reached for a necrotic core of 4 cm diameter (119°C). The profiles show that the profiles differ and also the temperatures reached are higher, due to a lack of blood perfusion.

ters being 0 cm, 1 cm, 2 cm, 3 cm, 4 cm. The blood perfusion rate is held constant over time. The results are shown in Figure 4.4. It is clearly visible that the temperature in the GTV increases with a larger necrotic core for the maximum, minimum and average temperatures. Also, the amount of temperature difference changes with different necrotic core sizes. A larger necrotic core means less heat removed in the entire GTV, while an equal amount of heat is added. The result is an increase in minimum temperature at the edge of the GTV. Even though the diameter of the necrotic core increases linearly between the tested cases, the area without blood perfusion increases with  $\frac{d^2}{4} \cdot \pi$ . This explains the larger increase in minimum temperature for larger necrotic diameters. Oppositely, Figure 4.4c shows a smaller increase in maximum temperature for larger diameter. The results suggest that the effect on the maximum temperature is smaller between necrotic cores of 3 and 4 cm, than on the maximum temperature between 2 and 3 cm. If close to the centre of a seed, heat is removed by blood perfusion, the temperature difference is larger than when the tissue surrounding the seed is necrotic. A larger temperature difference increases the amount of heat diffusing away from the seed, resulting in a lower maximum temperature. If the necrotic diameter increases, the influence of the blood perfusion on the maximum temperature decreases. This explains the smaller difference in maximum temperature for larger necrotic core diameters. The temperature over time graphs are supported by the temperature values given in Table 4.2 at 20 minutes. These results are sensible, because with a larger necrotic core there is less blood flow in the tumor, resulting in less heat being removed from the system. Figure 4.5a supports that the temperature increases with a larger necrotic core.

The second criterion that is investigated is the influence of necrotic tumor tissue on the distribution of the heat. The results in Figures 4.5a and 4.3 show that for different necrotic core diameters the temperature distribution is spread differently through the tissue. The distribution profiles are clearly show that for larger diameters the heat is contained inside the necrotic core, resulting in higher temperatures compared to smaller diameters. As a result of less removal of heat, the temperature in the viable tumor tissue surrounding the necrotic core is also higher for larger diameter. This is validated by the intersection profiles (Figure 4.5a).

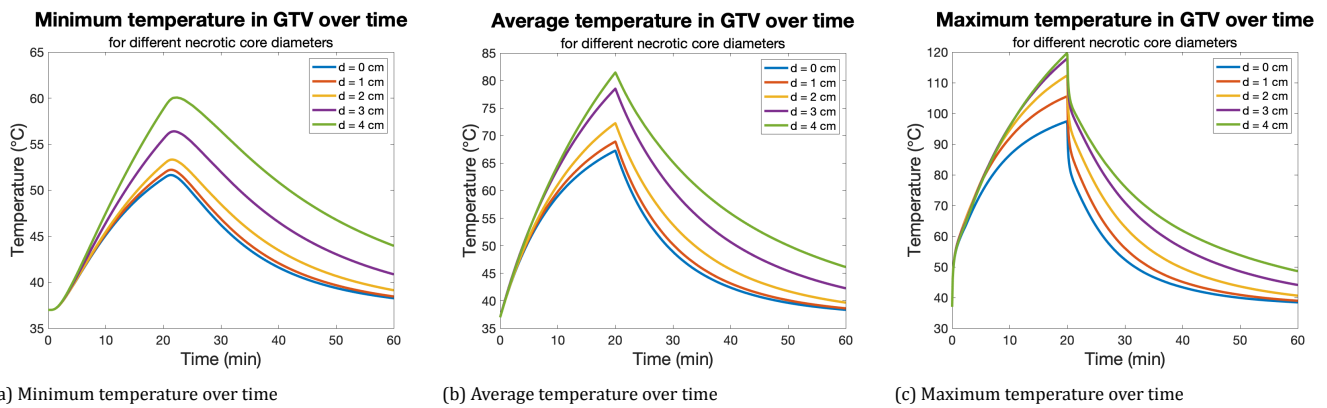
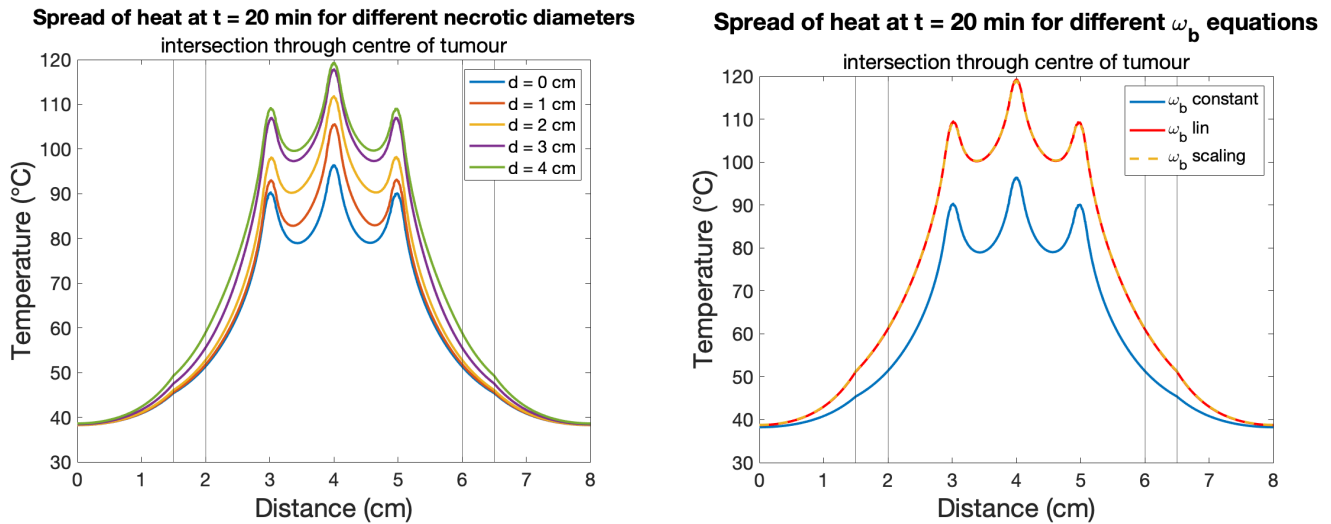


Figure 4.4: Temperature over time for different necrotic core diameters, being 0 cm, 1 cm, 2 cm, 3 cm and 4 cm. A larger necrotic core means a larger part of the tumor without blood perfusion and thus leads to a higher temperature and wider spread.



(a) Temperature through centre of tumors with different necrotic core diameters

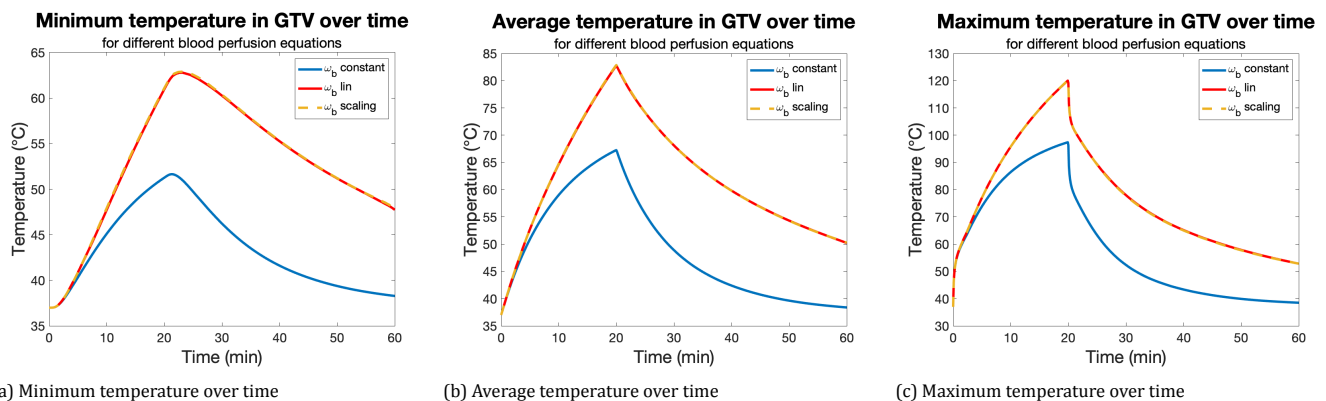
(b) Temperature through centre of tumor for different blood perfusion equations

Figure 4.5: The vertical lines indicate the outer shell of the GTV and PTV. (a) Overview of the intersection through the centre of the tumor for different necrotic core diameters (0 cm, 1 cm, 2 cm, 3 cm and 4 cm) after 20 minutes. It shows that higher temperatures are reached in the necrotic areas, where no heat is removed. (b) Overview of the intersection through the centre of the tumor for different blood perfusion relations. The linear relation (Equation 2.4; blue) and scaling function (Equation 2.5; yellow) give the same results. The default blood perfusion relation is constant (Equation 2.3; red)

### Blood perfusion rate: Temperature and time dependence

The blood perfusion rate is dependent on temperature too, because the vascular system gets damaged when heated above a certain temperature [2, 64]. The result is a lack of blood perfusion and no more heat will be removed from the system in that area by blood perfusion. Three different equations are tested to describe the effect of different blood perfusion relations depending on temperature. The first is the constant blood perfusion rate assumed in Pennes bioheat equation, Equation 2.3. The second equation includes the decrease in blood perfusion above a critical temperature  $T_{cr} = 45^{\circ}\text{C}$  to zero at  $48^{\circ}\text{C}$ , described in Equation 2.4. The third Equation is proposed by Stauffer *et al.*, who suggest that the blood perfusion rate is first increased for a small increase in temperature before the vascular system is damaged, after which the blood perfusion rate decreases to zero [2, 64]. These blood perfusion rates also depend on time, because the temperature is time dependent.

Figure 4.5b shows the temperature intersection through the centre of the tumor. The linear equation and the scaling function  $F(T)$  equation proposed by Stauffer *et al.* give almost the same temperature results after 20 minutes. This similar behaviour is confirmed by the temperature results in Table 4.2. This suggests that the blood perfusion increase for temperatures below  $45^{\circ}\text{C}$  has insignificant impact on the temperature during the first 20 minutes of the simulation. This can be explained by the fact that the average temperature in the GTV is increased to  $48^{\circ}\text{C}$  in approximately 3 minutes, Figure 4.6b. From this time on the temperature results deviate from the constant case, also in the minimum and maximum temperature graphs, Figures 4.6a and 4.6c respectively. This is noteworthy seeing that at  $t = 3$  min the minimum temperature has not reached  $48^{\circ}\text{C}$  yet.



(a) Minimum temperature over time

(b) Average temperature over time

(c) Maximum temperature over time

Figure 4.6: Temperature over time for different blood perfusion relations: constant (blue), linear (red) and scaling function  $F(T)$  (yellow). The temperature increases more strongly for the linear and  $F(T)$  functions, because after reaching  $48^{\circ}\text{C}$  there is no more blood perfusion. Also, after the AMF is switched off at  $t = 20$  min, the temperature decreases more slowly, because no heat is removed in the areas that have been heated above  $48^{\circ}\text{C}$ .

The temperature behaviour after the AMF is switched off is interesting as well. Figure 4.6a shows that the minimum temperature of the non-constant functions keeps increasing for a longer period than for the constant blood perfusion. This is explained by the fact that vascular system inside the GTV is destroyed and that the heat can only be removed in the area far outside the GTV. The minimum temperature in the GTV is increased for a longer time before the total temperature of the system is decreased. Also, the average and maximum temperatures decrease more slowly for the non-constant cases. This is sensible, seeing that the heat cannot be removed inside the GTV. To summarize: the effect of the blood perfusion equations related to the temperature over time is that it results in a higher overall temperature and a higher temperature distributed through the tumor. The results show that a different blood perfusion relation has significant impact on the temperature distribution.

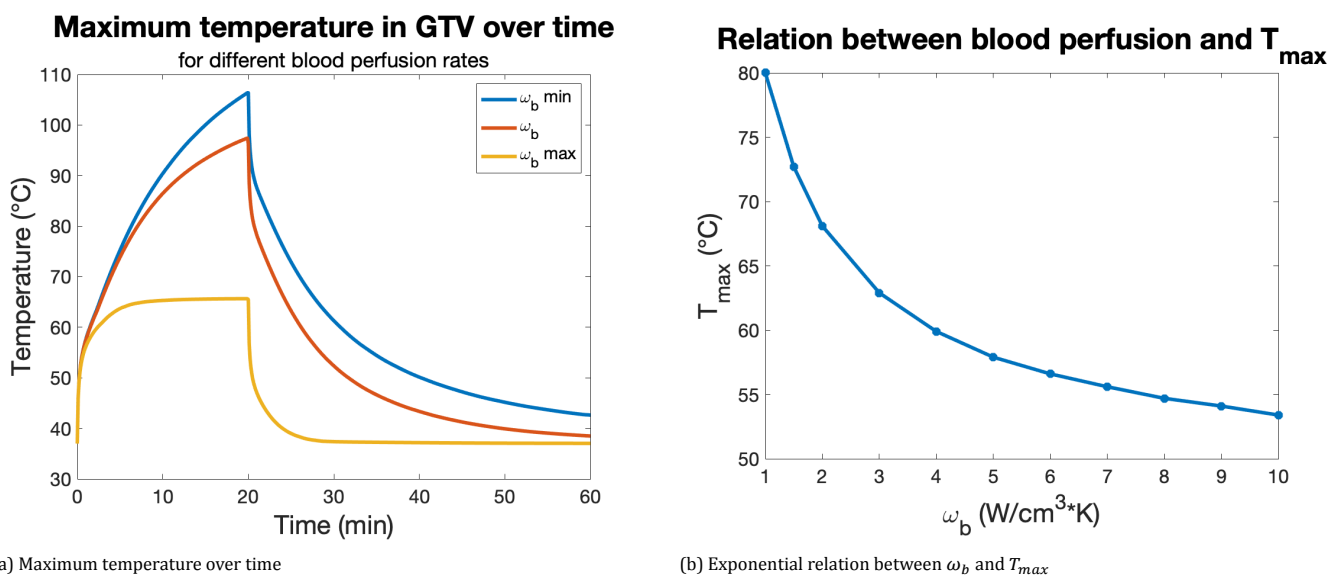
It should be noted that the different blood perfusion equations are also influenced by the SAR value and the tissue type. If for example the SAR value would be lower, less heat would be added by the nanoparticles, resulting in longer time to reach the higher temperatures. This will probably influence the effect of the blood perfusion relations and could make the difference between the linear and scaling function more significant. This is not investigated.

#### Blood perfusion rate: Minimum and maximum

Lastly, the effect of the blood perfusion rate is tested for a minimum and a maximum value found in literature. In Figure 4.8a the influence of the blood perfusion rate when assumed constant is visible. The overall temperature decreases with higher blood perfusion rate, because more heat is removed from the system. Also the spread of temperature is different. For a smaller  $\omega_b$  the heat is removed slowly and has more time to spread further from the seed centres than for large  $\omega_b$ . It is also worth noting that the centre seed generally has a higher temperature because it cannot lose its heat to its surroundings as easily as the seeds on the outside. For large blood perfusion rates, this is not the case, because the heat is removed faster from the system by blood perfusion than by conduction. The result is that the temperature difference between the seeds becomes smaller.

Figure 4.7a indicates that not only the maximum temperature of a system with a high  $\omega_b$  is lower, it also reaches steady state. The system finds a balance between the addition of heat by the nanoparticles and the removal of the same amount of heat by blood perfusion. Furthermore, the temperature decreases faster after the AMF is switched off for a larger blood perfusion rate than for a smaller blood perfusion rate. The anomaly in temperature decrease found for smaller blood perfusion rates caused by the inability of the centre seed to lose its heat to its surroundings is not present for larger blood perfusion rates. This can be explained by the same concept that the heat from the centre seed is removed primarily by blood perfusion rather than heat conduction.

Table 4.2 shows that the effect of the temperature in the GTV is stronger when the  $\omega_b$  is increased than when decreased. This non-linear effect is investigated and it seems that the temperature decreases exponentially with increasing blood perfusion rate (Figure 4.7b). All results regarding the blood perfusion rate value show that the impact of the blood perfusion rate to the temperature results is significant, seeing that the temperatures decrease exponentially and heat is less far distributed with increase blood perfusion rate.



(a) Maximum temperature over time

(b) Exponential relation between  $\omega_b$  and  $T_{max}$

Figure 4.7: (a) Temperature over time for different blood perfusion rates: minimum (red), default (blue) and maximum (yellow). For a smaller blood perfusion rate, higher temperatures are reached. Also, the temperature is removed slower from the system with smaller blood perfusion. (b) The investigated relation between temperature and blood perfusion rate suggests an exponential relation, where the maximum temperature decreases with increasing blood perfusion rate. The blood perfusion rate is assumed constant over temperature and time.

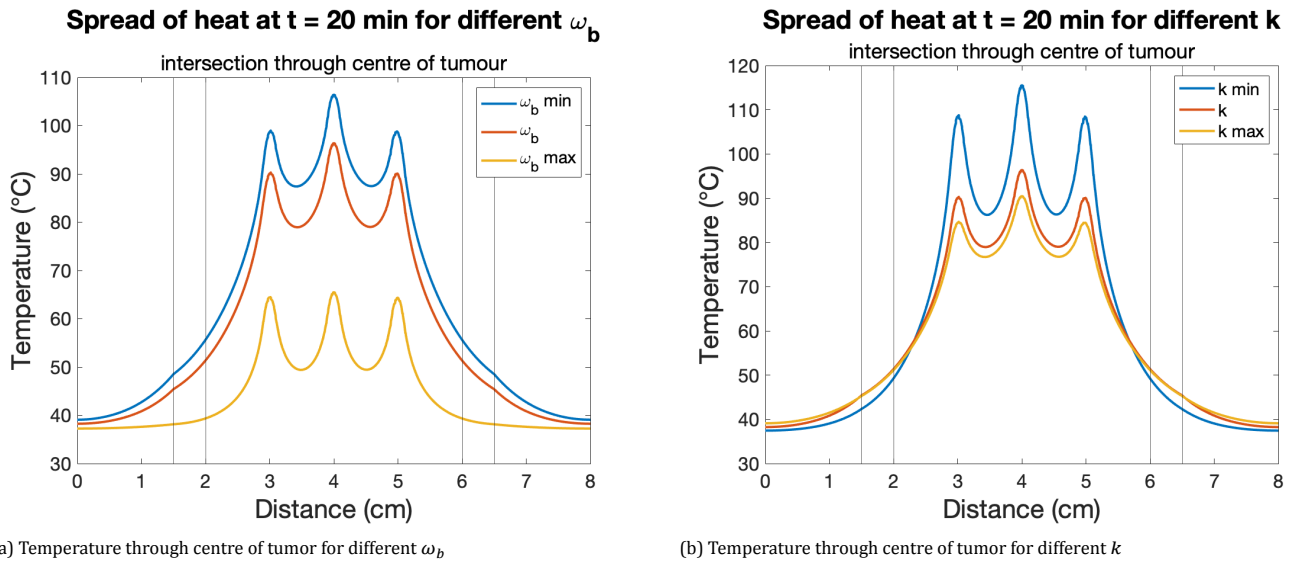
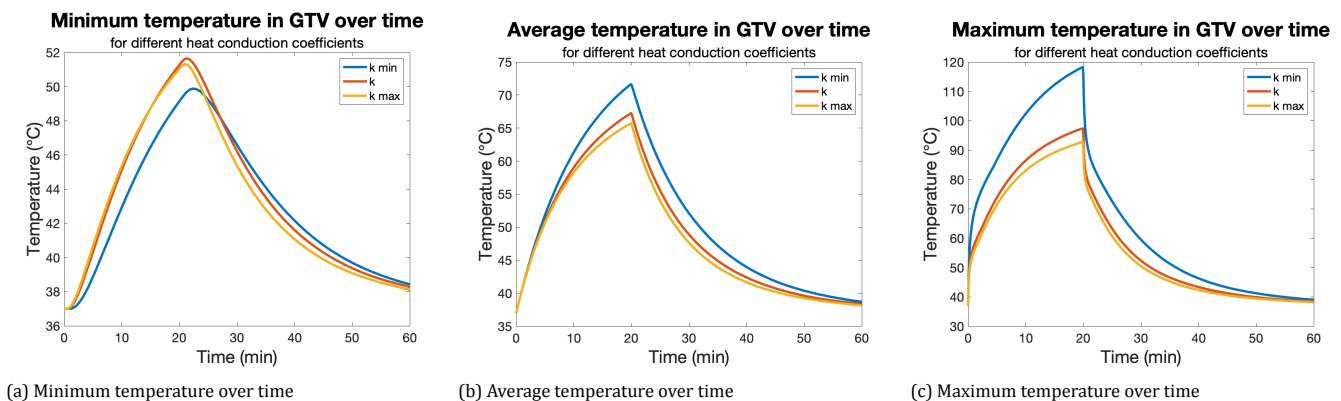
(a) Temperature through centre of tumor for different  $\omega_b$ (b) Temperature through centre of tumor for different  $k$ 

Figure 4.8: (a) Intersection through the centre of the tumor for different blood perfusion rates after 20 minutes of heating, showing wider temperature distribution for smaller blood perfusion rate. (b) Intersection through the centre of the tumor of different heat conduction rates. A smaller heat conduction coefficient means slower spread of heat. It results in higher local temperatures and a smaller distribution.

### Heat conduction

The rate of conduction is a material specific constant and has influence on the temperature distribution. For a higher conduction rate, heat spreads faster through a material. This leads to the hypothesis that for higher heat conduction coefficient the temperature profile has lower temperature peaks and is spread more homogeneously through the tumor. In Table 4.2 the results of changing the conduction rate to a minimum and maximum found in literature are shown. It is clearly visible that even though the heat conduction rate increase is smaller compared to the minimum tested value, the temperature increase is significantly larger. This is validated by the sensitivity index for the heat conduction coefficient in Table 4.3. Slower spread of heat increases the maximum temperature significantly, while returning a lower temperature in the PTV and outside it. Figure 4.8b shows the temperature of the intersection through the centre of the tumor. It is visible that for a small  $k$  the maximum temperature is higher, while further away from the seeds the temperature is lower, compared to the larger values of  $k$ . The maximum temperature in the GTV (Figure 4.9c) is higher for  $k_{min}$ , while the minimum temperature is lowest (Figure 4.9a), compared to the other values. All three Figures confirm the temperature results of the different areas of interest, found in Table 4.2.

Despite the influence of the heat conduction rate on the temperature, Figure 4.8b also shows that there is no significant difference in temperature profile through the GTV area. The maximum temperature does not determine the performance of the treatment, since it is the minimum temperature inside the GTV that determines whether the treatment worked. Considering this, the influence of the heat conduction rate on the first treatment goal could be assumed insignificant, within the range found in literature. However, the second requirement that formulates a maximum acceptable temperature outside the PTV is influenced strongly by the heat conduction, meaning that the results are far from accurate if the input heat conduction coefficient proves to differ strongly from its theoretical value. Therefore, information on the magnitude of the heat conduction coefficient is necessary to perform relevant temperature distribution simulations.



(a) Minimum temperature over time

(b) Average temperature over time

(c) Maximum temperature over time

Figure 4.9: Temperature over time for different heat conduction coefficients. A larger heat conduction coefficient leads to lower maximum temperatures and faster removal and results in a wider spread of heat, and thus a higher minimum temperature in the GTV.

### Magnetic nanoparticle heat source

The nanoparticle heat source  $Q_{NP}$  depends linearly on the Specific Absorption Rate (SAR) value of the nanoparticles, the concentration (mass%) of nanoparticles in the seed and the density of the tissue material, see Equation 2.6. The effect of the  $Q_{NP}$  on the temperature and distribution is tested by using the minimum and maximum  $SAR_{seed}$  ( $= SAR_{NP} \cdot \%mass$ ). The results are visible in Figure 4.10. In literature it is found that the SAR value is linearly related to temperature [74], which is confirmed with the sensitivity values of this model in Table 4.3. The difference in temperature is also visible in Figure 4.10c. Also, the peaks of the centre seeds are higher for high  $Q_{NP}$ . This is sensible, because even though the absolute temperature difference is bigger, the relative temperature difference between the centre and outer seeds is the same for the different  $Q_{NP}$  values.

The temperature spread distance is not affected by the change in  $Q_{NP}$ , which means that the  $Q_{NP}$  does not influence the temperature distribution. In Table 4.3 it is shown that the sensitivity of the treatment results to the  $Q_{NP}$  is very strong. It is verified that knowledge on the  $Q_{NP}$  is required for the treatment.

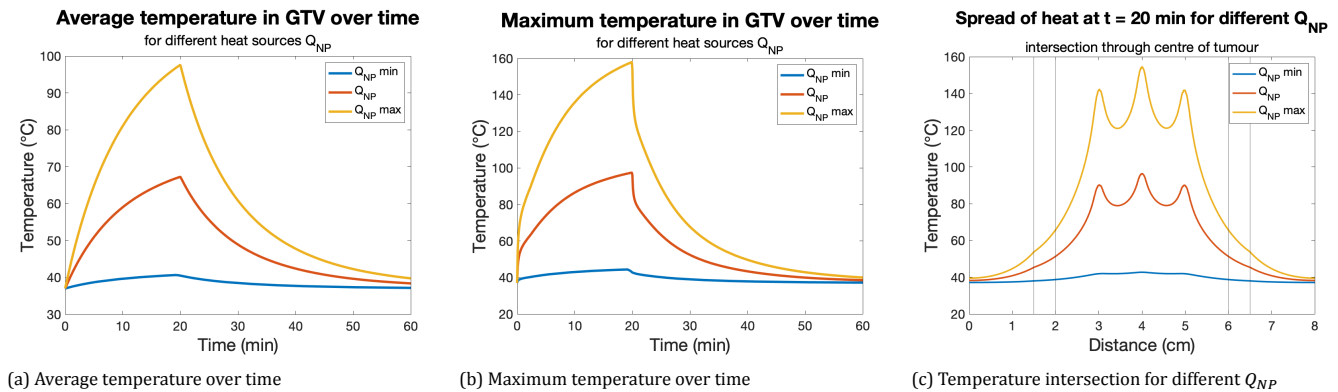


Figure 4.10: Different  $Q_{NP}$  values: minimum (blue), default (red) and maximum (yellow). A higher  $Q_{NP}$  leads to higher temperatures, with no change in profile.

The results of the sensitivity analysis are assembled in Table 4.2. It shows for each parameter of the model and system the direction of the change and whether the change is significant. The model is sensitive to the tumor tissue consistency, the blood perfusion rate and the nanoparticle heat source. These parameters influence the results strongly and their effect must be considered when interpreting the results using the model.

Table 4.2: Temperature results of sensitivity analysis of parameters evaluated using minimum, default and maximum values. For each parameter the maximum, minimum and average concentrations are found for the GTV, PTV area around the GTV and the area of 1 cm outside the PTV. [2, 4]

Variable	Unit	Value	GTV			PTV			PTV + 1 cm		
			$T_{max}$	$T_{av}$	$T_{min}$	$T_{max}$	$T_{av}$	$T_{min}$	$T_{max}$	$T_{av}$	$T_{min}$
<b>Necrotic core</b>											
$d_N = 0$ cm	cm	0	97.4	67.2	51.2	54.9	48.9	45.3	46.9	41.3	38.8
$d_N = 1$ cm	cm	1	105.5	68.9	51.7	55.5	49.2	45.6	47.1	41.4	38.8
$d_N = 2$ cm	cm	2	112.3	72.2	52.7	56.3	49.8	46.0	47.5	41.6	38.8
$d_N = 3$ cm	cm	3	117.8	78.4	55.5	59.1	51.8	47.5	49.0	42.2	39.1
$d_N = 4$ cm	cm	4	119.6	81.3	58.7	62.8	54.3	49.2	50.9	43.0	39.3
<b>Blood perfusion</b>											
constant	$W/cm^3 \cdot K$	-	97.4	67.2	51.2	54.9	48.9	45.3	46.9	41.3	38.8
linear	$W/cm^3 \cdot K$	-	120.5	83.4	61.9	66.2	57.9	52.6	54.6	45.5	40.7
scaling function	$W/cm^3 \cdot K$	-	120.5	83.4	61.9	66.2	57.9	52.6	54.6	45.5	40.7
$\omega_b$ min	$W/cm^3 \cdot K$	3.56E-3	106.4	73.5	55.5	59.4	52.5	48.4	50.2	43.3	39.8
$\omega_b$ max	$W/cm^3 \cdot K$	2.16E-2	65.7	46.3	39.3	41.5	39.0	38.1	38.8	37.8	37.3
<b>Conduction rate</b>											
$k_{eff}$ normal	$W/cm \cdot K$	5.11E-3	97.4	67.2	51.2	54.9	48.9	45.3	46.9	41.3	38.8
$k_{eff}$ min	$W/cm \cdot K$	2.80E-3	118.3	71.6	49.1	55.0	46.6	42.3	44.3	39.6	37.8
$k_{eff}$ max	$W/cm \cdot K$	5.94E-3	92.8	65.7	51.0	54.2	48.5	45.2	46.4	41.8	39.4
<b>Heat source NP</b>											
SAR seed normal	$W/g$	10	97.4	67.2	51.2	54.9	48.9	45.3	46.9	41.3	38.8
SAR seed min	$W/g$	1.25	43.0	40.5	38.7	39.1	38.4	38.0	38.2	37.5	37.2
SAR seed max	$W/g$	20	157.9	97.51	65.5	72.9	60.7	53.6	56.7	45.7	40.5

Table 4.3: Sensitivity index of every parameter in the temperature model. It shows the relation between the tested parameter and the effect on the minimum temperature in the GTV (left) and the maximum temperature in the area surrounding the PTV (right). These temperatures are the values of interest to check whether the temperature requirements are met. The parameters are ranked from large impact to small impact.

Parameter	SI		Parameter	SI	
	GTV	$T_{min}$		PTV + 1cm	$T_{max}$
$Q_{NP}$	min	0.28	$k_{eff}$	max	-0.34
$Q_{NP}$	max	0.28	$Q_{NP}$	min	0.21
$k_{eff}$	max	-0.26	$Q_{NP}$	max	0.21
$\omega_b$	min	0.18	$\omega_b$	min	0.15
$d_N$	4 cm	0.15	$d_N$	4 cm	0.085
$d_N$	3 cm	0.11	$d_N$	3 cm	0.059
$d_N$	2 cm	0.059	$\omega_b$	max	-0.034
$\omega_b$	max	-0.046	$d_N$	2 cm	0.027
$d_N$	1 cm	0.040	$d_N$	1 cm	0.022
$k_{eff}$	max	0.010	$k_{eff}$	min	0.022

#### 4.2.2. Sensitivity of Concentration and Dose Results to Model Parameters

As explained in Section 3.2.3, the concentration model is based on Equation 3.7, including solely the time dependent concentration term and the diffusion term. Since the dose calculations are based on the concentration results, these parameters can be of influence on the dose distribution. In this section the significance and sensitivity of the dose results to the diffusion coefficient  $D$  and the initial concentration  $c_i$  are evaluated.

The default breast tissue type used in the model is homogeneous glandular breast tissue, similar to the temperature model. The tumor tissue is assumed fully necrotic, as a result of the thermal ablation. When the tumor would be assumed fully viable, the convection terms could not be neglected, changing the PDE that described the system. This is expected to effect the concentration profile strongly, because then there would be another process having influence on the transport of the nanoparticles. The values for  $D$  and  $c_i$  used as default values (shown in Table 3.2) might vary due to assumptions made or due to the variety of values reported in literature. These differences can exist due to measurement inaccuracies, not perfectly comparable set-ups or properties being patient specific. The sensitivity of the model to these value ranges of the different properties is tested. The effects are evaluated on their dose distribution and influence on reaching the identified treatment goals. This is investigated by calculating the maximum, average and minimum delivered cumulative dose in different areas of the geometry, over time. The areas are defined as follows: the GTV core, the PTV surrounding it and in the area of 1 cm surrounding the PTV. Also the distribution profile in 2D, the intersection through the centre of the tumor and the dose over time are generated for the XZ plane. The relevant results are presented in this section.

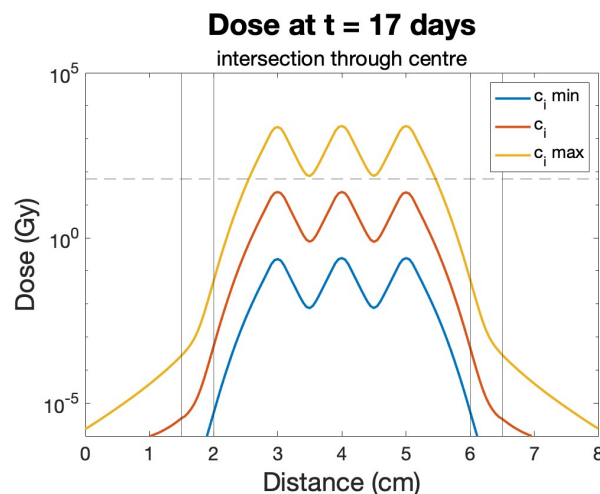


Figure 4.11: Intersection through the centre of the tumor after 17 days for different initial nanoparticle concentrations in the seeds. It shows a higher overall dose for higher initial concentration with no change in distribution. The tested initial concentrations were increased with a factor  $10^2$ . This exact difference is visible in the intersection graph.

#### Initial concentration

The initial concentration of nanoparticles in the seeds is determined by the total amount of nanoparticles in the seeds. The maximum concentration is limited by the synthesis of the seeds, which can for example differ due to uncertainties during synthesis. The initial concentration cannot exactly be determined afterwards. It has been found that for a different

initial concentration the relative nanoparticle distribution remains the same and only the total concentration changes. By using these concentration results to calculate the dose distribution, the same trend was found in the results of the dose model for different initial nanoparticle concentrations. The tested initial concentrations were increased and decreased with a factor  $10^2$ . This exact difference is found in the delivered dose results in Table 4.4. The figures representing the maximum, average and minimum delivered dose after 17 days in the GTV in Figure 4.13, prove that over time the dose distribution is the same for the three different cases. Only the colorbar values and the iso-dose lines change with different initial condition. It can therefore be said that the distribution of the dose is not influenced by a difference in initial concentration, while the total dose delivered is. The dose in the centre of the seeds is highest, because the highest concentration of nanoparticles is found at those locations. The emitted electrons do not travel far through tissue, resulting in high local dose at the centre of the seeds. The iso-dose lines and the results in Table 4.4 show that the dose level in the PTV is negligible for the default and minimum initial concentrations within 17 days.

Additionally, the intersection graph, Figure 4.11, and the dose over time graphs in Figure 4.13, give three identical representations of the dose. The only difference is a linear increase in value. The sensitivity values shown in Table 4.5 confirm that the change in dose distribution linearly depends on the change in initial concentration. These results show that the dose distribution is fairly sensitive to the initial concentration, as it ranks among the highest sensitivity indices.

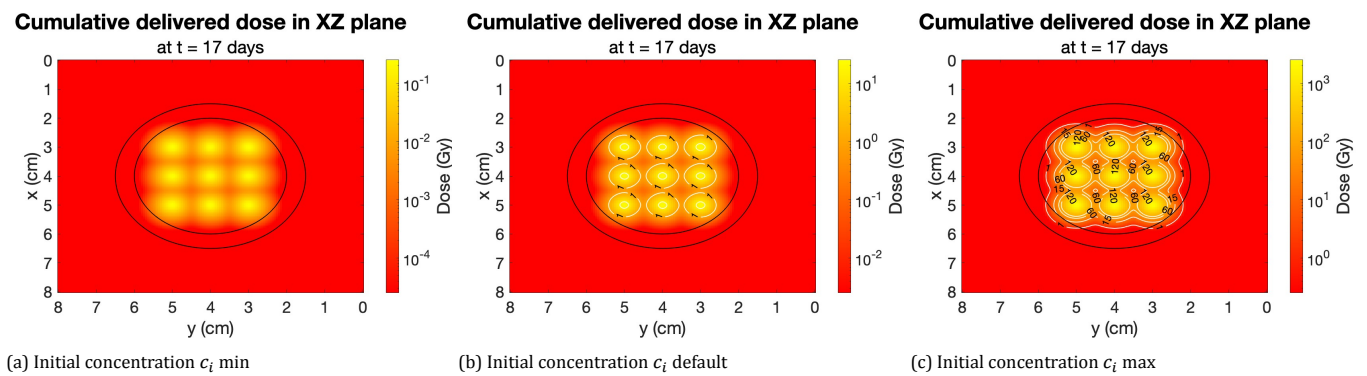


Figure 4.12: Dose distribution profiles in XZ plane after 17 days for different initial nanoparticle concentrations. The profiles show that the dose increases with increasing concentration, while the relative dose distribution remains the same.

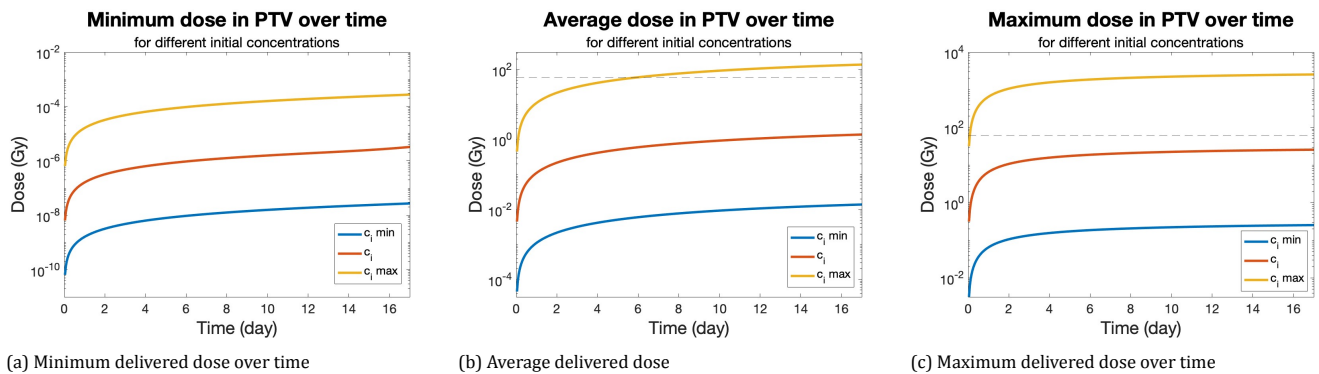


Figure 4.13: Concentration of nanoparticles over time for different initial concentration in the seeds: minimum (blue), default (red) and maximum (yellow). A higher initial condition leads to a higher concentration and thus a higher dose. The relation is linear and does not influence the dose distribution.

### Diffusion coefficient

The diffusion coefficient represents the rate at which a material is spread through a volume. For this study, it is expected that a larger diffusion coefficient means faster transport of the nanoparticles through the tumor, resulting in a more homogeneous spread of nanoparticles. This expected result is confirmed by intersection Figure 4.14a and the 2D distribution profiles of different  $D$  (Figure 4.15). The distribution profile strongly differs for changing diffusion coefficients. A larger  $D$  results in a wider distributed concentration profile, which means that the radiation is emitted from wider spread locations and thus the dose is more homogeneously spread. However, since the amount of dose delivered remains the same, the maximum dose at the seed locations decreases, visible in Figure 4.14. Figures 4.14b and 4.14c show that the minimum dose of the  $D_{\max}$  is highest compared to the other tested diffusion coefficients, while the maximum concentration is lowest.

Furthermore, in Figure 4.14b it is shown that for the zero, minimum and default  $D$  values, the minimum dose over time in the PTV area looks similar, while in the maximum dose over time graph different dose values over time are found. This

unexpected result can be explained when looking closely to Figure 4.14b and to the minimum dose results in Table 4.4. The minimum cumulative doses do differ, but only slightly due to the low absolute dose. Table 4.5 gives the sensitivity of the model to the diffusion coefficient. The results show that the model is more sensitive to an increase in diffusion coefficient than a decrease. Because the default diffusion coefficient is significantly small already, an even smaller  $D$  will not influence the spread within the 17 day time scale.

The diffusion coefficient of the nanoparticles described in this study through tumor and breast tissue is not yet verified. In previous research a diffusion rate of the order of magnitude  $10^{-8}$  was measured [5], however, for other experiments, the nanoparticles showed zero diffusive behaviour. Seeing that the diffusion coefficient is not yet known, the effect of non-diffusive nanoparticles on the dose distribution is studied as well. The results show that without diffusion of nanoparticles the dose spread is only slightly through the tissue. These results were expected and show that the dose requirements will not easily be met if the nanoparticles do not diffuse through tissue.

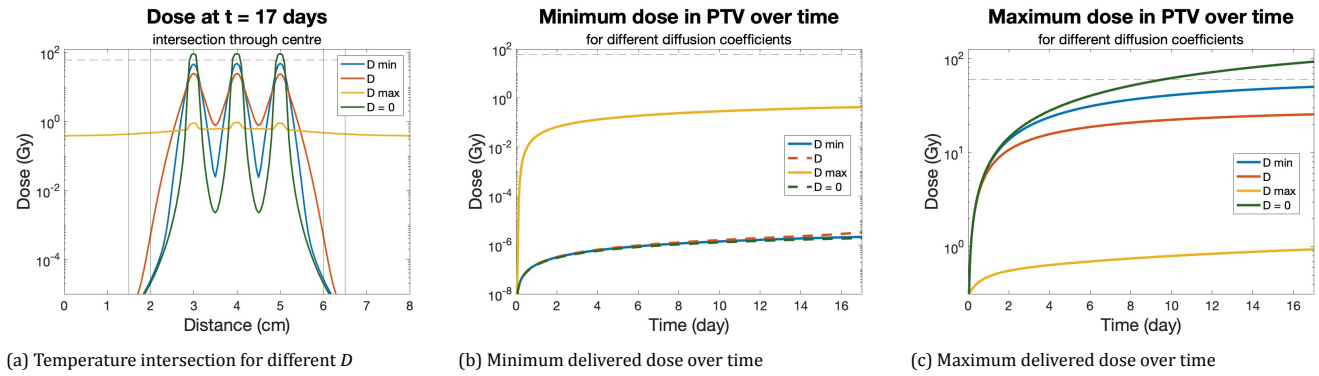


Figure 4.14: Effect of different diffusion coefficients: minimum (blue), default (red), maximum (yellow) and  $D$  is zero (green). (a) Intersection through the centre of the tumor after 17 days for different diffusion coefficients with logarithmic axis representing the cumulative dose; (b) Maximum dose over time; (c) Maximum dose over time. Higher diffusion coefficient leads to faster spread of nanoparticles through tissue, resulting in lower overall dose, but wider distribution.

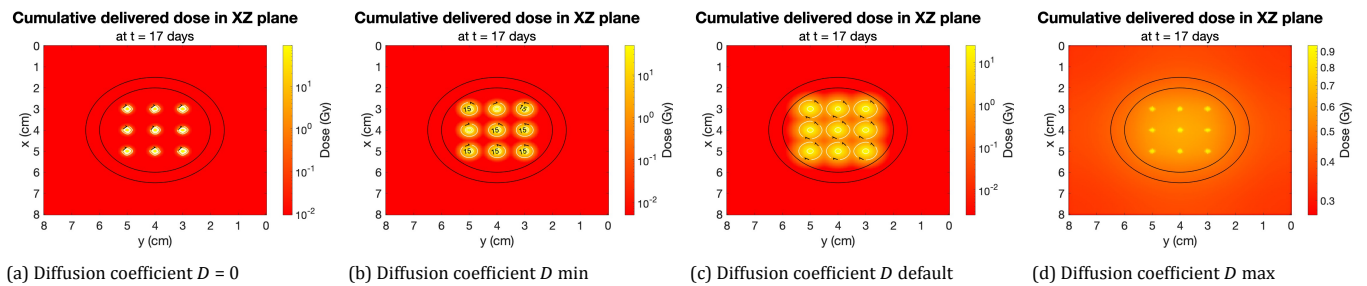


Figure 4.15: Dose distribution profiles in XZ plane after 17 days for different diffusion coefficients. The profiles show that the distributions differ strongly, especially for large  $D$ .

Table 4.4: Concentration results of sensitivity analysis of parameters evaluated using minimum, default and maximum values. For each parameter the maximum, minimum and average cumulative dose is found for the GTV, PTV area around the GTV and the area of 1 cm outside the PTV. [5, 6]

Variable	Unit	Value	GTV			PTV			PTV + 1 cm		
			Dose <sub>max</sub>	Dose <sub>av</sub>	Dose <sub>min</sub>	Dose <sub>max</sub>	Dose <sub>av</sub>	Dose <sub>min</sub>	Dose <sub>max</sub>	Dose <sub>av</sub>	Dose <sub>min</sub>
<b>Diffusion rate</b>											
$D_{\text{eff normal}}$	cm/s	2.20E-8	2.54E+1	3.67E-4	2.16E+0	1.36E-1	2.73E-6	5.14E-3	9.10E-5	7.13E-8	1.03E-5
$D_{\text{eff min}}$	cm/s	6.4E-9	5.00E+1	2.48E-5	2.16E+0	1.40E-3	2.14E-6	5.39E-5	1.28E-5	6.42E-8	1.19E-6
$D_{\text{eff max}}$	cm/s	1.5E-5	9.40E-1	4.69E-1	5.51E-1	4.81E-1	4.29E-1	4.50E-1	4.32E-1	3.80E-1	4.04E-1
$D_{\text{eff zero}}$	cm/s	0	9.24E+1	2.04E-5	2.07E+0	4.13E-4	1.90E-6	3.24E-5	1.07E-5	5.93E-8	1.04E-6
<b>Concentration of NPs</b>											
$c_i$	#NP/cm <sup>2</sup>	7.97E+9	2.54E+1	3.67E-4	2.16E+0	1.36E-1	2.73E-6	5.14E-3	9.10E-5	7.13E-8	1.03E-5
$c_i \text{ min}$	#NP/cm <sup>2</sup>	7.97E+7	2.54E-1	3.67E-6	2.16E-2	1.40E-3	2.73E-8	5.14E-5	9.12E-7	7.13E-10	3.25E-8
$c_i \text{ max}$	#NP/cm <sup>2</sup>	7.97E+11	2.54E+3	3.67E-2	2.16E+2	1.36E+1	2.73E-4	5.14E-1	9.10E-3	7.13E-6	3.25E-3

Table 4.5: Sensitivity index of every parameter in the concentration model to the cumulative delivered dose distribution. It shows the relation between the tested parameter and the effect on the minimum dose in the PTV and the maximum dose in the area surrounding the PTV. These delivered doses are the values of interest to check whether the delivered cumulative dose requirements are met. The parameters are ranked from large impact to small impact for both results of interest separately.

Parameter		SI Dose <sub>min</sub> PTV
$D$	max	230.3
$c_i$	max	1.0
$c_i$	min	1.0
$D$	min	0.3
$D$	0	0.3

Parameter		SI Dose <sub>max</sub> PTV + 1 cm
$D$	max	7.0
$D$	min	1.2
$c_i$	max	1.0
$c_i$	min	1.0
$D$	0	0.9

### 4.2.3. Sensitivity of Temperature and Dose to Optimization Variables

Most parameters in the models are physical properties or patient specific variables that cannot be influenced, but there are five adjustable variables that can be optimized during treatment planning. The first two are the seed concentration  $c_i$  and the seed location. These two have influence on the temperature and delivered dose. For the thermal part of the treatment, also the strength of the magnetic field  $H$  and the time  $t$  it is switched on can be changed. For the dose optimization, the activity of the nanoparticles  $A$  is the only adjustable variable. All other parameters within the model are physical properties or computational variables. The sensitivity of the models, and thus the treatment, to those adjustable variables is investigated by varying the default values 10% in positive and negative direction. The sensitivity indices resulting from this is given in Table 4.6. It distinguishes for each adjustable variable the effect on the temperature and dose, except for the seed location. The effect of this variable is explained in Section 4.3. The activity does not affect the temperature results, so the temperature is not sensitive to that adjustable variable. Similarly, the magnetic field strength and time do not affect the dose distribution, meaning the dose is not sensitive to these adjustable variables.

#### Temperature Optimization

First, the effect of the adjustable variables on the temperature are investigated, starting with the concentration of the nanoparticles in the seeds. The concentration of nanoparticles is related to the heat generated by the seeds, because  $Q_{seed}$  depends on the SAR of the nanoparticles and on the concentration of nanoparticles in the seed. The results will therefore have an equal sensitivity to the concentration of the nanoparticles as they have to the  $Q_{NP}$ . The sensitivity of  $Q_{NP}$  has been investigated already in Section 4.2.1 and has been confirmed by the sensitivity of the temperature to the nanoparticle concentration. For a lower concentration, the overall temperature decreases linearly.

The second variable is the alternating magnetic field strength,  $H$ . This variable is related to the  $Q_{NP}$  too. The  $SAR_{NP}$  increases with increasing magnetic field strength, according to the proportionality relation  $SAR \propto H^2$  [75, 76]. The  $SAR_{NP}$  value has proven to increase the temperature linearly (see Section 4.2.1), making the AMF strength a variable that can increase or decrease the temperature, without changing the distance the heat travels. The temperature results are more sensitive to a 10% change in magnetic field strength due to the quadratic relation, showing that the temperature is most sensitive to the magnetic field strength.

The third adjustable variable is the time  $t$  the AMF is switched on. Results are shown in Figures 4.16a, 4.16b and 4.16c. Over time, the heat spreads through the material, causing the temperature distribution to be spread more widely through the material if the AMF is switched on longer. Also, more time leads to more heat added to the system by the nanoparticles, resulting in higher temperatures. The sensitivity indices of the adjustable variables on the temperature distribution are shown in Table 4.6. The temperatures used to calculate these are the temperatures at the time the AMF is switched off, so at 18 min, 20 min and 22 min.

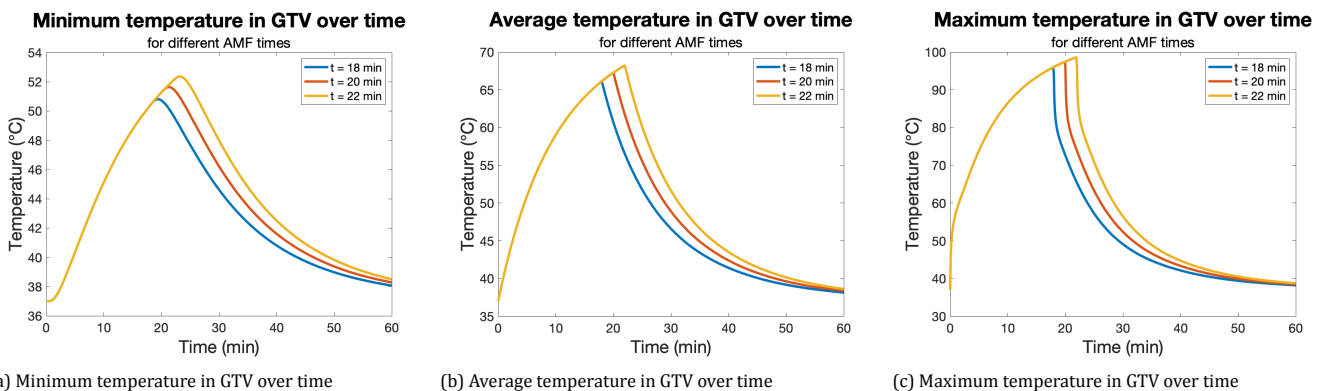


Figure 4.16: Temperature over time for different AMF times. The temperatures increase when the AMF is switched on for a longer time.

### Dose Optimization

To reach the treatment goals of the radiation part, the seed locations, the nanoparticle concentration and the nanoparticle activity are the only adjustable variables. The sensitivity of the dose distribution to the initial concentration of the nanoparticles in the seeds has already been investigated in section 4.2.2. The overall cumulative dose will increase linearly, while the distribution profile will remain the same, resulting in the same sensitivity indices for -10% and +10% concentration.

Secondly, the radioactivity of the nanoparticles is adjustable, even though it is not the preferred variable. This is because the Pd-103 radionuclides are delivered with a standard activity value. Changing this value would be either costly, if a customized activity is requested by the supplier, or a waste of radiation, when waiting for the activity to decrease over time if a lower activity is required. The relation between the activity and the delivered dose is proportional to the influence of the concentration to the delivered dose. This is, because having more nanoparticles to irradiate the tissue is the same as when the same number of nanoparticles have higher activity. From this relation it follows that the same sensitivity index is found for the activity as for the initial concentration. Nanoparticles with a lower radioactivity will have a lower dose rate, while keeping an equal dose distribution. The sensitivity indices of the adjustable variables on the dose distribution are shown in Table 4.6. It can be concluded that the delivered dose has equal sensitivity to the initial concentration as to the activity.

Table 4.6: Sensitivity index of adjustable variables for treatment optimization. It shows that only two variables influence the dose, with the same sensitivity index, and three variables affect the temperature. The nanoparticle concentration affects both temperature and dose distribution.

Parameter		Sensitivity Index			
		GTV $T_{\min}$	PTV + 1cm $T_{\max}$	PTV Dose <sub>min</sub>	PTV + 1cm Dose <sub>max</sub>
$c_i$	min	0.28	0.21	1.0	1.0
$c_i$	max	0.28	0.21	1.0	1.0
$A$	min	-	-	1.0	1.0
$A$	max	-	-	1.0	1.0
$H$	min	0.53	0.40	-	-
$H$	max	0.59	0.44	-	-
$t$	min	0.18	0.16	-	-
$t$	max	0.16	0.14	-	-

### 4.3. Treatment Planning Optimization

The purpose of treatment planning is to formulate a patient specific plan to help the patient to a healthier condition. As indicated in Figure 2.7, it is necessary to have knowledge of the state of the condition of the patient, before treatment planning is started. It includes everything to do with the diagnosis, such as images of the tumor. Also knowledge of the most sensitive parameters, identified in Section 4.2, is required. The treatment plan itself consists of a treatment proposal, based on the patient specific conditions and physical properties, to reach the goal of the therapy. It includes the selected parameter options for the adjustable treatment variables.

Apart from simulating the treatment, the goal is to ultimately use the built models for optimization of the treatment planning. In this section an approach for treatment optimization of both the XZ and YZ planes is described based on the results of the reference case in Section 4.1. The hypothetical tumor studied in this project is the spherical fully viable tumor ( $d_{GTV} = 4$  cm,  $d_{PTV} = 5$  cm) in Figure 3.4c with physical properties defined in Tables 3.1 and 3.2. Currently, the optimization is done by adjusting a single variable, checking the improvement and deciding the next step.

The optimization parameter that affects the temperature and dose distribution simultaneously is the seed location. This includes both the number of seeds and the location of those seeds in the tumor. More seeds would increase the overall temperature and dose, since there will be more nanoparticles to heat up or irradiate the tissue. Figure 3.6c shows the locations of the seeds in the 3D tumor volume, being 21 seeds in total. As stated in Chapter 2, the average number of seeds implanted is 100 during a LDR brachytherapy prostate tumor treatment of average size. This number is significantly higher than used in the reference case. Also, the location of the seeds has influence on how far the heat has spread or how deep the decay products will deposit their energy in the tissue. If the seeds are placed further away from the centre of the tumor, the heat and nanoparticles will spread further outside the GTV, resulting in a higher temperature and cumulative dose, respectively. Changing the location of the seeds is, however, limited by the brachytemplate distance. The distance between seeds in the XZ plane can be either 5 mm or 10 mm and in the YZ plane the seeds are separated by spacers, of 5 mm length. The location in the Y direction, depth into the tumor, is free of limits as the depth of the deepest seed is variable. Overall, a larger distance between the seeds is preferred if looking at patient comfort, but this must be possible when looking at the dose requirements. The seed location variable can be used to adjust the temperature and

dose differences between the XZ and YZ planes. The number of seeds can be changed to increase or decrease the total result, both temperature and cumulative dose. It is expected that adding seeds will significantly increase the temperature and delivered dose. To find the sensitivity of these results to the number of seeds, different seed location formations need to be compared. Also, because all tumors are patient specific, the tumor can differ in shape. Optimizing seed locations and number of seeds is then a good way to achieve the treatment goals. Furthermore, optimizing the seed location and number for the specific and unrealistic case in this study is not meaningful, as nothing general can be concluded from those results.

Despite the tumor specificity, a general optimization approach has been built that can be used as an optimization guideline. Based on the reference results, the temperature requirement of a minimum temperature of 48 °C in the GTV area is reached, but the temperature outside the PTV is too high. This means that the thermal ablation part reached too high temperatures, even though it successfully ablated the GTV. On the other hand, the dose requirements were not met, because the minimum dose in the PTV was below 60 Gy. Due to the large differences in achieving the treatment goals between temperature and cumulative dose, it is not recommended to change the seed number or location, as changing those variables will have impact on both treatment parts. Nevertheless, the seed locations can be changed between the XZ and YZ plane, to decrease the large difference in distribution between those planes for temperature and cumulative dose.

Because it is strongly preferred to not change the activity of the nanoparticles, the seed location, number and initial concentration are the only adjustable variables left to reach the cumulative delivered dose. Because the consequences of changes in these variables to the temperature distribution can be compensated by the  $H$  and  $t$ , the dose optimization should be done first. The preferred variable is the initial nanoparticle concentration, because the dose is more sensitive to that variable than temperature, as shown in Table 4.6. The results of the reference case suggest that the dose is not delivered far enough through the tumor, while the area close to the seeds receives high enough dose. Therefore, it might seem beneficial to place the seeds further away from the centre of the tumor, while lowering the initial concentration of nanoparticles in the outer seeds. This is, however, not a preferred solution, because it will be challenging to synthesise seeds with different concentration, so if possible, this option is to be avoided. Additionally, it is expected that there will be a maximum to the amount of nanoparticles that can be added to the seed as well.

The temperature distribution after increasing the nanoparticle concentration will be undesirably high. Consequently, the magnetic field strength  $H$  and the time  $t$  the field is turned on can compensate for this increase. Both variables are easily adjusted and can still be adjusted during the treatment in contrast to the activity, seed location and initial concentration. Those variables are fixed immediately after the start of the treatment. By decreasing the  $H$ , the dose optimization effects are compensated best, since the sensitivity index is highest. Additionally, if the time is decreased, not only the total temperature is decreased, also the distribution is altered. The heat will have had less time to spread through the tissue, which can be beneficial for achieving the goal of not reaching high temperatures outside the PTV. Table 4.7 gives an overview of the possible solutions to tackle a specific problem in meeting the requirements. It also describes the consequences of the solution.

Table 4.7: Overview of the possible solutions to tackle a specific optimization problem in an attempt to meet the requirements. It also describes the consequences of the solution to the results it affects.

Problem	Adjustable Variables	Result
Difference between XZ and YZ	Seed location Seed number	Better comparable results between XZ and YZ
Temperature and dose too high/low	Seed number Seed location NP concentration	Change of total temperature, total dose and distribution Effect on distribution of temperature and dose Increase/decrease of total temperature and dose
Dose too high/low	NP concentration Activity (not preferred)	Change in total dose, but also in temperature Increase/decrease of total dose
Temperature too high/low	NP concentration Magnetic field strength Time	Effect on total temperature, but also on dose Increase/decrease of total temperature Effect on total temperature and distribution
Temperature too high outside PTV	Time	Larger temperature decrease outside PTV than inside

## 4.4. Critical Notes

The complexity of the human body is a source of research inspiration, but also makes research in the medical field a difficult task. Every human body works differently making it impossible to find a single value for physical properties and mechanisms. This makes models simulating body processes uncertain. In addition to the physical uncertainties, multiple assumptions and simplifications have been made, leading to the results being less accurate. However, the models give an indication of the order of magnitude of the results and the sensitivity of the model and treatment to certain properties and variables. The variables to which the models are highly sensitive need to be known, to be able to simulate the therapy accurately. The temperature model is sensitive to all investigated variables, i.e. necrotic core diameter, blood perfusion relation and rate, heat conduction coefficient and nanoparticle heat. The necrotic core diameter is a physical property

that is patient specific and must be investigated during the diagnosis stage. These sensitivity results suggest that tumors with larger necrotic cores are heated up faster to higher temperatures and decrease in temperature more slowly than tumors with an active vascular structure. However, if a more realistic blood perfusion relation is included in the model, the sensitivity of the model to the necrotic core diameter would decrease. This is because the vascular system would be destroyed quickly, resulting in a lack of blood perfusion in the tumor, similar to necrotic tumor tissue. It is also discovered in the optimization part that the seed concentration and seed locations have a large impact on the temperature distribution. The concentration model is also sensitive to all investigated variables, i.e. initial concentration, diffusion coefficient and seed location.

Furthermore, the built models are basic 2D models, using a simple geometry. The 2D representation shows intersections in XZ and YZ directions through the centre of the unrealistically perfect spherical tumor. The 2D results do not show the temperature and dose distribution in the tumor in the outer layers off centre. It is expected that the results will be higher for other slices through the tumor, since the edge of the GTV is furthest away from a seed through the centre than through any other point. This means that the temperature will be higher and spread further outside the GTV than shown in Figure 4.1c. Also, the centre planes do not represent the slices where no seeds are placed. In these slices the temperature and dose are only increased by nearby seeds. Lastly, the 2D representation does not show the results in every angle. These limitations of the 2D models make it impossible to do proper treatment planning with the 2D model, which requires a 3D view of the results. Nevertheless, it does give a good indication on the processes happening during the treatment.

In Section 4.1 it is found that there is a large difference in temperature between the XZ and YZ plane. This is a result of the larger seed area in the YZ direction. The seeds contain more nanoparticles in the YZ direction than in the XZ direction, meaning more heat is generated in the YZ plane, resulting in higher temperatures. In 3D, however, the seed would be able to lose part of its heat in the X direction too, while in this model the heat can only spread in the YZ direction. In a 3D model, the temperature difference between XZ and YZ would decrease, to zero at the centre. Additionally, it must be noted that the maximum temperatures reached in the YZ plane are unrealistically high. Firstly, the temperatures reached are above the boiling point of tissue, 100 °C, taken equal to that of water. This phenomenon is not included in the temperature model, making the temperature results in tissue area heated above 100 °C inaccurate. Also, at higher temperatures than Curie temperature, the magnetic behaviour of the superparamagnetic nanoparticles can get compromised. Although this temperature is not known yet for the Pd-103 SPIO nanoparticles, values found in literature for pure iron-oxides or materials containing iron-oxide were above 227°C up to 650°C [77–79]. The temperature results obtained within this study do not go above 119°C, so it is not expected that the magnetic behaviour will be compromised during the treatment.

The results give an indication of the effect and the sensitivity of the model to the parameters, but the chosen moments of interest, 20 minutes of heating and after 17 days of diffusion, to evaluate the results are not the last moment of the treatment. It takes time for the temperature to decrease after switching off the AMF and the radioactivity after 17 days is only halved, resulting in higher cumulative dose before nanoparticles leave body. Moreover, since the

# Conclusion and Further Recommendations

This research aimed to simulate the temperature, concentration and dose distributions of the newly proposed combined thermo-brachytherapy for early-stage breast cancer using radio- and thermo-active  $^{103}\text{Pd}$  superparamagnetic iron-oxide nanoparticle implants. After building these models, the results were evaluated, showing that the dose distribution, thus the internal radiation part of the combined treatment is limiting compared to the thermal ablation. Subsequently, a qualitative analysis is done to identify the robustness of the models by performing a sensitivity analysis on all model parameters and optimization variables. For the temperature model, changes in the nanoparticle heat source value, an increased heat conduction coefficient and a decreased blood perfusion rate have the largest impact on the simulation outcomes. The concentration and dose model is sensitive to both the initial concentration and the diffusion coefficient, the latter having more impact on the results when decreased. It is concluded that these parameters are most important to increase the quality of the models. To ultimately be able to use the models for treatment optimization, the five optimization variables were identified after which the sensitivity of the results to these adjustable variables was tested. Both models are sensitive to the number of seeds and the location in the tumor where they are placed. Quantifying these variables is difficult, but it is useful to adjust them when the results are not equal in all directions or when both temperature and dose results need to be corrected in the same way. The dose distribution can be optimized by adjusting the nanoparticle concentration in the seeds and the activity of the nanoparticles, being equally sensitive to both variables. Temperature optimization is achieved by changing the nanoparticle concentration too, the strength of the magnetic field or the time the alternating magnetic field is switched on. The first two have the biggest impact on the temperature outcome.

The models do have limitations that influence the results strongly. Due to large uncertainties in properties and simplifications of physical processes, the simulation outcomes are less accurate. However, the models do provide information on the order of magnitude of the results. Further research should be done to determine properties, especially the diffusion coefficient, and to gain more understanding of the impact of the underlying physical processes to the results, e.g. blood perfusion. Also, the effect of the treatment to the physical properties and processes should be investigated too, to check whether the assumptions on properties being constant are accurate over time. Moreover, the simulation generates results in 2D, using only the cross sections through the centre of a simplified tumor. This does not provide complete information on the distribution since it does not include the interaction between the seed in different planes. These limitations make it impossible to do proper treatment planning, which requires a 3D view of the results. Therefore, it is recommended to convert the models to 3D, to better simulate the proposed treatment and to gain knowledge on the temperature and dose distribution in three dimensions. The proposed next steps to take are to further improve the models. This can be done by including more complex physical processes, such as adding convection in the concentration model. Also, a more accurate description of the blood perfusion and more complex geometries can be investigated in the future. Additionally, it is advised to improve the models by including the parts of the treatment that are currently neglected, such as diffusion during thermal ablation and heating up of the nanoparticles. Also, the dose model should more accurately include the dose delivered in the tumor after 17 days. The impact of these phases is currently assumed negligible, but this should be investigated too.

In order to achieve the goal of using the models for treatment optimization, after they have been translated to 3D, it should be possible to do the optimization automatically instead of manually. Also, a more quantitative investigation of the number of seeds and their location is required. If the models can be improved so that they are able to optimize the results automatically for the given geometry, the predictive models would become more suitable as a treatment optimization tool. Ultimately, it is desired to bring the combined therapy to the clinic. If this is achieved, research can be done to investigate if the treatment can be used for other cancer types, where the built models can aid in exploring the sensitivity and possibilities.

The research goal to gain more insight in the behaviour of the treatment material in tissue and to be able to predict if the treatment results are achieved, by identifying the effectiveness and limitations of the combined therapy and by analysing the sensitivity to the relevant physical properties and optimization parameters. Therefore, this study has contributed by providing basic knowledge of the state-of-the-art early stage breast cancer combined therapy, bringing it one step closer to clinical implementation.

# List of Abbreviations

**AMF** Alternating magnetic field.

**APBI** Accelerated partial breast irradiation.

**BC** Boundary condition.

**CTV** Clinical target volume.

**DCIS** Ductal carcinoma in situ.

**DNA** Deoxyribonucleic acid.

**FEM** Finite element method.

**GTV** Gross tumor volume.

**HDR** High dose rate.

**I-125** Iodine-125.

**IC** Initial condition.

**IDC** Invasive ductal carcinoma.

**ILC** Invasive lobular carcinoma.

**LDR** Low dose rate.

**MNP** Magnetic nanoparticle.

**NP** nanoparticle.

**Pd-103** Palladium-103.

**PDE** Partial differential equation.

**PTV** Planning target volume.

**RF** Radiofrequency.

**SAR** Specific absorption rate.

**SI** Sensitivity index.

**SPIO** Superparamagnetic iron-oxide.

**TA** Thermal Ablation.

**WBI** Whole breast irradiation.

# List of Symbols

Symbol	Unit	Description
$c$	#NP/m <sup>3</sup>	concentration
$c_i$	#NP/m <sup>3</sup>	initial concentration
$c_b$	J/(kg·°C)	specific heat of blood
$c_p$	J/(kg·°C)	specific heat
$d$	cm	diameter
$d_N$	cm	necrotic diameter
$D$	m <sup>2</sup> /s	diffusion coefficient
$\dot{D}$	Gy	dose distribution
$\vec{D}$	Gy	dose rate of a single nanoparticle
$h_{max}$	cm	maximum size length of mesh element
$J_L$	#NP/m <sup>3</sup>	transcapillary exchange through lymphatic vessels
$J_V$	#NP/m <sup>3</sup>	transcapillary exchange through blood vessels
$k/k_{eff}$	W/(m·°C)	thermal conductivity
$P$	m/s	permeability coefficient
$Pe$	-	Peclet number
SAR	W/g	specific absorption rate
$\frac{S}{V}$	1/m	surface area of microvessels per unit volume
$t$	s	time
$t_{1/2}$	s	half life
$T$	°C	temperature
$T_b$	°C	blood temperature
$T_i$	°C	initial temperature
$T_{cr}$	°C	critical temperature
$Q_m$	W/m <sup>3</sup>	metabolic heat
$Q_{NP}$	W/m <sup>3</sup>	heat flux of nanoparticle
$\vec{v}$	m/s	fluid velocity
$\lambda$	1/s	decay constant
$\rho$	kg/m <sup>3</sup>	density
$\phi_L$	1/s	transvascular fluid flow by lymphatic drainage
$\phi_V$	1/s	transvascular fluid flow by blood vessels
$\omega_b$	kg/(s·m <sup>3</sup> )	blood perfusion rate
$\omega_b^i$	kg/(s·m <sup>3</sup> )	initial blood perfusion rate
$\Omega$	m <sup>2</sup>	computational domain

# Reference list

- [1] Healthline, *What to know about different types of breast cancer*, <https://www.healthline.com/health/breast-cancer/types-of-breast-cancer#idc> (2021), accessed: 2022-07-01.
- [2] P. R. Stauffer, D. B. Rodrigues, R. Goldstein, T. Nguyen, Y. Yu, S. Wan, R. Woodward, M. Gibbs, I. L. Vasilchenko, A. M. Osintsev, V. Bar-Ad, D. B. Leeper, W. Shi, K. D. Judy, and M. D. Hurwitz, *Feasibility of removable balloon implant for simultaneous magnetic nanoparticle heating and HDR brachytherapy of brain tumor resection cavities*, *International Journal of Hyperthermia* **37**, 1189 (2020).
- [3] R. van Oossanen, J. Godart, J. M. Brown, A. Maier, J. P. Pignol, A. G. Denkova, K. Djanashvili, and G. C. van Rhoon, *Feasibility study on the radiation dose by radioactive magnetic core-shell nanoparticles for open-source brachytherapy*, "[Manuscript to be reviewed]" (2022).
- [4] J. S. Camilleri, L. Farrugia, S. Curto, D. B. Rodrigues, L. Farina, G. C. Dingli, J. Bonello, I. Farhat, and C. V. Sammut, *Review of thermal and physiological properties of human breast tissue*, *Sensors* **22**, 3894 (2022).
- [5] R. Willemse, *Determining the diffusion constant of nanoparticles in phantoms and tumour spheroids*, Ph.D. thesis, Delft University of Technology (2022).
- [6] S. Jeong and T. H. Kim, *Diffusion-weighted imaging of breast invasive lobular carcinoma: Comparison with invasive carcinoma of no special type using a histogram analysis*, *Quantitative Imaging in Medicine and Surgery* **12**, 95 (2022).
- [7] Breastcancer.org, *Breast cancer facts and statistics*, <https://www.breastcancer.org/facts-statistics> (2022), accessed: 2022-09-05.
- [8] World Cancer Research Fonds International, *Breast cancer statistics*, <https://www.wcrf.org/cancer-trends/breast-cancer-statistics/> (2022), accessed: 2022-09-05.
- [9] National Institute for Public Health and the Environment, *Breast cancer in the netherlands*, <https://www.rivm.nl/en/breast-cancer-screening-programme/breast-cancer-in-netherlands> (2018), accessed: 2022-09-05.
- [10] National Institute for Public Health and the Environment, *Breast cancer screening programme*, <https://www.rivm.nl/en/breast-cancer-screening-programme> (2022), accessed: 2022-09-05.
- [11] Eurostat Statistics Explained, *Archive:breast cancer screening statistics*, [https://ec.europa.eu/eurostat/statistics-explained/index.php?title=Archive:Breast\\_cancer\\_screening\\_statistics](https://ec.europa.eu/eurostat/statistics-explained/index.php?title=Archive:Breast_cancer_screening_statistics) (2011), accessed: 2022-09-05.
- [12] RIVM: Centre for Population Screening (CvB), *Breast cancer screening factsheet*, [https://www.rivm.nl/sites/default/files/2018-11/20150304%20Factsheet%20BK\\_EN%20%28definitief%29.pdf](https://www.rivm.nl/sites/default/files/2018-11/20150304%20Factsheet%20BK_EN%20%28definitief%29.pdf) (2015), accessed: 2022-09-05.
- [13] National Cancer Institute USA, *Definition of early-stage breast cancer*, <https://www.cancer.gov/publications/dictionaries/cancer-terms/def/early-stage-breast-cancer> (2021), accessed: 2022-03-22.
- [14] National Cancer Institute USA, *Cancer stat facts: Female breast cancer*, <https://seer.cancer.gov/statfacts/html/breast.html> (2022), accessed: 2022-09-05.
- [15] American Society of Clinical Oncology (ASCO), *Breast cancer: Types of treatment*, <https://www.cancer.net/cancer-types/breast-cancer/types-treatment> (2020-07), accessed: 2022-03-24.
- [16] S. Johnson, *Common treatment options available for early stage breast cancer*, <https://www.farnorthsurgery.com/about-us> (2021-04-26), accessed: 2022-03-24.
- [17] R. A. Revia and M. Zhang, *Magnetite nanoparticles for cancer diagnosis, treatment, and treatment monitoring: Recent advances*, *Materials Today* **19**, 157 (2016).
- [18] C. Brace, *Thermal tumor ablation in clinical use*, *IEEE Pulse* **2**, 28 (2011).
- [19] V. Strnad and C. Yashar, *Breast brachytherapy*, *Brachytherapy* **20**, 976 (2021).
- [20] C. Chargari, E. Deutsch, P. Blanchard, S. Gouy, H. Martelli, F. Guérin, I. Dumas, A. Bossi, P. Morice, A. N. Viswanathan, and C. Haie-Meder, *Brachytherapy: An overview for clinicians*, *CA: A Cancer Journal for Clinicians* **69**, 386 (2019).

- [21] R. van Oossanen, *Nanoparticles for image guided thermo-brachytherapy*, Phd thesis proposal, TU Delft (2017).
- [22] I.J. Das et al., *Patterns of dose variability in radiation prescription of breast cancer*, *Radiotherapy and Oncology* **44**, 83 (1997).
- [23] Y. Smith, *Radiation therapy dosage*, <https://www.news-medical.net/health/Radiation-Therapy-Dosage.aspx> (2021), accessed: 2022-08-11.
- [24] Canadian Cancer Society, *Stages of breast cancer*, <https://cancer.ca/en/cancer-information/cancer-types/breast/staging> (2022), accessed: 2022-03-22.
- [25] J. Sheng, *Types of breast cancer*, <https://www.breastcancer.org/types> (2022-02-10), accessed: 2022-03-22.
- [26] World Health Organization, *Breast cancer*, <https://www.who.int/news-room/fact-sheets/detail/breast-cancer> (2021-03-21), accessed: 2022-03-22.
- [27] J. L. Connolly, S. J. Schnitt, H. H. Wang, J. Longtine, A. Dvorak, and H. F. Dvorak, *Cancer Medicine* (BC Decker, 2003).
- [28] N. Mahesh, N. Singh, and P. Talukdar, *A mathematical model for understanding nanoparticle biodistribution after intratumoral injection in cancer tumors*, *Journal of Drug Delivery Science and Technology* **68** (2022), 10.1016/j.jddst.2021.103048.
- [29] S. Talukdar, P. Bhoopathi, L. Emdad, S. Das, D. Sarkar, and P. B. Fisher, *Chapter Two - Dormancy and cancer stem cells: An enigma for cancer therapeutic targeting*, Vol. 141 (Advances in Cancer Research, Academic Press, 2019) pp. 43–84.
- [30] N. Burnet, S. Thomas, K. Burton, and S. Jefferies, *Defining the tumour and target volumes for radiotherapy*, *Cancer Imaging* **4**, 153 (2004).
- [31] J. Y. Kim, H. B. Suh, H. J. Kang, J. K. Shin, K. S. Choo, K. J. Nam, S. W. Lee, Y. L. Jung, and Y. T. Bae, *Apparent diffusion coefficient of breast cancer and normal fibroglandular tissue in diffusion-weighted imaging: the effects of menstrual cycle and menopausal status*, *Breast Cancer Research and Treatment* **157**, 31 (2016).
- [32] G. D. Hugo, E. Weiss, A. Badawi, and M. Orton, *Localization accuracy of the clinical target volume during image-guided radiotherapy of lung cancer*, *International Journal of Radiation Oncology Biology Physics* **81**, 560 (2011).
- [33] A. M. Kirby, C. E. Coles, and J. R. Yarnold, *Target volume definition for external beam partial breast radiotherapy: Clinical, pathological and technical studies informing current approaches*, *Radiotherapy and Oncology* **94**, 255 (2010).
- [34] National Cancer Institute, *Radiation therapy to treat cancer*, <https://www.cancer.gov/about-cancer/treatment/types/radiation-therapy> (2019), accessed: 2022-09-05.
- [35] X. Mei, R. T. Cate, C. M. van Leeuwen, H. M. Rodermond, L. de Leeuw, D. Dimitrakopoulou, L. J. Stalpers, J. Crezee, H. P. Kok, N. A. Franken, and A. L. Oei, *Radiosensitization by hyperthermia: The effects of temperature, sequence, and time interval in cervical cell lines*, *Cancers* **12** (2020), 10.3390/cancers12030582.
- [36] C. L. Dennis and R. Ivkov, *Physics of heat generation using magnetic nanoparticles for hyperthermia*, *International Journal of Hyperthermia* **29**, 715 (2013).
- [37] O. Seror, *Ablative therapies: Advantages and disadvantages of radiofrequency, cryotherapy, microwave and electroporation methods, or how to choose the right method for an individual patient?* *Diagnostic and Interventional Imaging* **96**, 617 (2015).
- [38] C. H. Lineweaver, P. C. Davies, and M. D. Vincent, *Targeting cancer's weaknesses (not its strengths): Therapeutic strategies suggested by the atavistic model*, *BioEssays* **36**, 827 (2014).
- [39] by Christina Marie Li Hsu, M. L. Palmeri, J. Y. Lo, E. Samei, and J. A. Baker, *Three-dimensional computerized breast phantom based on empirical data*, (2010).
- [40] P. Lai, E. Lechtman, S. Mashouf, J. P. Pignol, and R. M. Reilly, *Depot system for controlled release of gold nanoparticles with precise intratumoral placement by permanent brachytherapy seed implantation (psi) techniques*, *International Journal of Pharmaceutics* **515**, 729 (2016).
- [41] Cleveland Clinic, *Permanent radioactive seed implants: What are they, how do they work?* <https://my.clevelandclinic.org/health/treatments/5566-permanent-radioactive-seed-implants-what-are-they-how-> (2020), accessed: 2022-09-05.
- [42] Dartmouth Cancer Centre, *Pd-103 seeds for prostate cancers*, <https://cancer.dartmouth.edu/radiation-oncology/pd-103-seeds-prostate-cancers> (2022), accessed: 2022-04-29.

- [43] M. Lu, W. Yao, T. Zhang, W. Fan, Z. Zhong, J. Li, and F. Zhang, *Feasibility and efficacy of microwave ablation combined with iodine-125 seed implantation in local control of recurrent retroperitoneal liposarcomas: Initial clinical experience*, *The Oncologist* **22**, 1500 (2017).
- [44] J. Rieke, P. Wust, A. Stohlmann, A. Beck, C. H. Cho, M. Pech, G. Wieners, B. Spors, M. Werk, C. Rosner, E. L. Hänninen, and R. Felix, *Ct-guided interstitial brachytherapy of liver malignancies alone or in combination with thermal ablation: Phase i-ii results of a novel technique*, *International Journal of Radiation Oncology Biology Physics* **58**, 1496 (2004).
- [45] L. E. Aguilar, R. G. Thomas, M. J. Moon, Y. Y. Jeong, C. H. Park, and C. S. Kim, *Implantable chemothermal brachytherapy seeds: A synergistic approach to brachytherapy using polymeric dual drug delivery and hyperthermia for malignant solid tumor ablation*, *European Journal of Pharmaceutics and Biopharmaceutics* **129**, 191 (2018).
- [46] M. Laprise-Pelletier, J. Lagueux, M. F. Côté, T. LaGrange, and M. A. Fortin, *Low-dose prostate cancer brachytherapy with radioactive palladium-gold nanoparticles*, *Advanced Healthcare Materials* **6** (2017), 10.1002/adhm.201601120.
- [47] S. Strohmaier and G. Zwierzchowski, *Comparison of 60co and 192ir sources in HDR brachytherapy*, *Journal of Contemporary Brachytherapy* **3**, 199 (2011).
- [48] L. Delclos, U. K. Dinshaw, I. A. Gerbault, F. T. Inoue, J. J. Pinilla, C. A. Tahir, and M. J. Uribe, *The role of long half-life isotopes for use in HDR brachytherapy 1w tata*, (2000).
- [49] J. P. Pignol, B. Keller, E. Rakovitch, R. Sankrecha, H. Easton, and W. Que, *First report of a permanent breast 103pd seed implant as adjuvant radiation treatment for early-stage breast cancer*, (2006) pp. 176–181.
- [50] D. Olofsson, L. Cheng, R. B. Fernández, M. Płodowska, M. L. Riego, P. Akuwudike, H. Lisowska, L. Lundholm, and A. Wojcik, *Biological effectiveness of very high gamma dose rate and its implication for radiological protection*, *Radiation and Environmental Biophysics* **59**, 451 (2020).
- [51] F. Y. Cheng, C. H. Su, Y. S. Yang, C. S. Yeh, C. Y. Tsai, C. L. Wu, M. T. Wu, and D. B. Shieh, *Characterization of aqueous dispersions of fe<sub>3</sub>o<sub>4</sub> nanoparticles and their biomedical applications*, *Biomaterials* **26**, 729 (2005).
- [52] P. Granitzer, K. Rumpf, R. Gonzalez, J. Coffey, and M. Reissner, *Magnetic properties of superparamagnetic nanoparticles loaded into silicon nanotubes*, (2014).
- [53] H. Fatima, T. Charinpanitkul, and K. S. Kim, *Fundamentals to apply magnetic nanoparticles for hyperthermia therapy*, *Nanomaterials* **11** (2021), 10.3390/nano11051203.
- [54] A. E. Deatsch and B. A. Evans, *Heating efficiency in magnetic nanoparticle hyperthermia*, *Journal of Magnetism and Magnetic Materials* **354**, 163 (2014).
- [55] Y. Kumar, *Hysteresis loss*, <https://circuitglobe.com/what-is-hysteresis-loss.html> (2018), accessed: 2022-09-05.
- [56] R. K. Titz, W. Weitschies, L. Trahms, and W. Semmler, *Investigation of brownian and neher relaxation in magnetic fluids*, *Journal of Magnetism and Magnetic Materials* **201**, 102 (1999).
- [57] H. H. Pennes, *Analysis of tissue and arterial blood temperatures in the resting human forearm*, *Journal of Applied Physiology*, 93 (1948).
- [58] N. Sinha, G. Cifter, E. Sajo, R. K. Phd, S. Sridhar, P. L. Nguyen, R. A. Cormack, G. M. Makrigiorgos, and W. Ngwa, *Brachytherapy application with in situ dose painting administered by gold nanoparticle eluters*, *International Journal of Radiation Oncology Biology Physics* **91**, 385 (2015).
- [59] L. Bianchi, F. Cavarzan, L. Ciampitti, M. Cremonesi, F. Grilli, and P. Saccomandi, *Thermophysical and mechanical properties of biological tissues as a function of temperature: a systematic literature review*, *International Journal of Hyperthermia* **39**, 297 (2022).
- [60] D. C. Shrestha, S. Acharya, and D. B. Gurung, *Modeling on metabolic rate and thermoregulation in three layered human skin during carpentering, swimming and marathon*, *Applied Mathematics* **11**, 753 (2020).
- [61] Song, M. Sumit, and R. G. René M., *Skin burn injuries and heat stress/fatalities* (Elsevier, 2017) pp. 17–26.
- [62] B. E. Lyons, T. V. Samulski, R. S. Cox, and P. Fessenden, *Heat loss and blood flow during hyperthermia in normal canine brain i: Empirical study and analysis*, *INT. J. HYPERTHERMIA* **5**, 225 (1989).
- [63] L. L. Ferrás, N. J. Ford, M. L. Morgado, J. M. Nóbrega, and M. Rebelo, *Fractional pennes' bioheat equation: Theoretical and numerical studies*, (2010).

- [64] S. K. Kandala, E. Liapi, L. L. Whitcomb, A. Attaluri, and R. Ivkov, *Temperature-controlled power modulation compensates for heterogeneous nanoparticle distributions: a computational optimization analysis for magnetic hyperthermia*, *International Journal of Hyperthermia* **36**, 115 (2019).
- [65] P. Prakash, *Theoretical modeling for hepatic microwave ablation*, *The Open Biomedical Engineering Journal* **4**, 27 (2010).
- [66] A. I. Jensen, F. Zhuravlev, G. Severin, C. B. Magnus, J. Fonslet, U. Köster, and M. Jensen, *A solid support generator of the auger electron emitter rhodium-103m from [103pd]palladium*, *Applied Radiation and Isotopes* **156** (2020), 10.1016/j.apradiso.2019.108985.
- [67] MathWorks, Inc., *Math. graphics. programming*. <https://nl.mathworks.com/products/matlab.html> (2022), accessed: 2022-08-01.
- [68] MathWorks, Inc., *Partial Differential Equation Toolbox, User's Guide* (2016).
- [69] J. van Kan, A. Segal, and F. Vermolen, *Numerical Methods in Scientific Computing* (VSSD, 2008).
- [70] S. Rotundo, D. Brizi, A. Flori, G. Giovannetti, L. Menichetti, and A. Monorchio, *Shaping and focusing magnetic field in the human body: State-of-the art and promising technologies*, *Sensors* **22** (2022), 10.3390/s22145132.
- [71] MedlinePlus, *Body temperature norms*, <https://medlineplus.gov/ency/article/001982.htm> (2022), accessed: 2022-08-08.
- [72] V. Darvishi, M. Navidbakhsh, and S. Amanpour, *Heat and mass transfer in the hyperthermia cancer treatment by magnetic nanoparticles*, *Heat and Mass Transfer/Waerme- und Stoffuebertragung* (2021), 10.1007/s00231-021-03161-3.
- [73] F. Boateng and W. Ngwa, *Modeling gold nanoparticle-eluting spacer degradation during brachytherapy application with in situ dose painting*, *British Journal of Radiology* **90** (2017), 10.1259/bjr.20170069.
- [74] Y. Yamamoto, T. Itoh, and T. Irieda, *A heat dissipation study of iron oxide nanoparticles embedded an agar phantom for the purpose of magnetic fluid hyperthermia*, *Journal of Nanoscience and Nanotechnology* **19**, 5469 (2019).
- [75] C. M. Collins and Z. Wang, *Calculation of radiofrequency electromagnetic fields and their effects in mri of human subjects*, *Magnetic Resonance in Medicine* **65**, 1470 (2011).
- [76] MRIquestions.com, *Specific absorption rate*, <https://mriquestions.com/what-is-sar.html> (2021), accessed: 2022-09-05.
- [77] J. López-Sánchez, G. McIntosh, M. L. Osete, A. del Campo, J. J. Villalaín, L. Pérez, M. Kovacheva, and O. R. de la Fuente, *Epsilon iron oxide: Origin of the high coercivity stable low curie temperature magnetic phase found in heated archeological materials*, *Geochemistry, Geophysics, Geosystems* **18**, 2646 (2017).
- [78] B. Santos, E. Loginova, A. Mascaraque, A. K. Schmid, K. F. Mccarty, and J. D. L. Figuera, *Structure and magnetism in ultra thin iron oxides characterized by low energy electron microscopy*, .
- [79] K. H. J. Buschow, M. Flemings, and R. Cahn, *The Encyclopedia of Materials: Science and Technology* (Pergamon Imprint, 2001).

# Appendices contents

<b>A</b>	<b>Minima, Maxima of Parameters and Model Variables</b>	<b>i</b>
<b>B</b>	<b>Additional Temperature Model Results</b>	<b>ii</b>
<b>C</b>	<b>Concentration Model Results</b>	<b>iii</b>

# A

## Minima, Maxima of Parameters and Model Variables

### Mimima and Maxima of Temperature and Concentration Parameters

Tables A.1 and A.2 give the minimum and maximum values used for the sensitivity analysis for each parameter included in the model. The values based on literature values include the corresponding reference.

Table A.1: Minimum and maximum values used during sensitivity analysis for parameters of temperature model. Values for bloodperfusion rate and conduction rate extracted from temperature properties review executed by *Camilleri et al.* [4] Other variables determined during project execution.

Variable	Unit	Value
<b>Necrotic core</b>		
necrotic diameter $d$	cm	1, 2, 3, 4
<b>Blood perfusion rate</b>		
$\omega_b$ min	W/cm <sup>3</sup> *K	3.56E-3
$\omega_b$ max	W/cm <sup>3</sup> *K	2.16E-2
<b>Conduction rate</b>		
$k_{\text{eff}}$ min	W/cm*K	2.80E-3
$k_{\text{eff}}$ max	W/cm*K	5.94E-3
<b>Heat source NP</b>		
SAR seed min	W/g	1.25
SAR seed max	W/g	20

Table A.2: Minimum and maximum values used during sensitivity analysis for parameters of concentration model. Diffusion coefficient range found in literature [5, 6] and initial concentration is determined within project.

Variable	Unit	Value
<b>Diffusion rate</b>		
$D_{\text{eff}}$ min	cm <sup>2</sup> /s	6.4E-9
$D_{\text{eff}}$ max	cm <sup>2</sup> /s	1.50E-5
<b>Concentration of NPs</b>		
$c_i$	#NP/cm <sup>3</sup>	7.97E+9
$c_i$ min	#NP/cm <sup>3</sup>	7.97E+7
$c_i$ max	#NP/cm <sup>3</sup>	7.97E+11

### Model Parameters

The input variables of the temperature and concentration models are included in table A.3.

Table A.3: Table includes the model specific variables that are used in both temperature and concentration PDE solving models.

MODEL VARIABLES	UNIT	VALUE	JUSTIFICATION
<b>GEOMETRY AND MESH</b>			
total volume	cm <sup>2</sup>	2D GTV and PTV tumor + part of breast	Used by model to mesh and calculate linear equations used to solve the 2D PDE
tumor shape	cm <sup>2</sup>	circle	Simplified 2D tumor
<b>NP seeds</b>			
- Geometry	-	XZ: circle, YZ: square	Cross sections through cylindrical seeds
- number of seeds	#	Total: 23, XZ: 9, YZ: 7	Number of seeds depending treatment goals
- location of seeds	[cm,cm]	X and Y coordinates	Locations of the seeds are pre-determined
- XZ: diameter seeds	cm	0.2	Diameter of the seeds
- YZ: size seed	cm	0.2x0.5	Length of the seeds
hmax	cm	0.05	Defines the maximum the mesh element side length. Smaller than seed diameter
<b>TEMPERATURE MODEL</b>			
<b>Boundary conditions</b>			
type	-	Neumann	Boundary condition between inside and outside the volume of interest. Neumann represents flux over the boundary
coefficients		$q = 0, g = 0$	Diffusion driven, convection neglected, source zero in breast
<b>Initial conditions</b>			
breast and tumor	°C	37	Body temperature
<b>PDE coefficients</b>			
c: conduction	W/cm K	$k_{breast}$ and $k_{tumor}$	Heat conduction coefficients found in literature
f: source	W/cm <sup>3</sup>	$\omega_b \Delta T$ and $Q_{NP}$	Bloodperfusion and NPs as heat source of NPs at seed locations
a: convection	W/cm <sup>3</sup>	0	Convection is not taken into account in the model, but it would represent the heat spread driven by convection
d: time derivative	J/cm <sup>3</sup> K	$\rho \cdot c_p$	First order time derivative coefficient. Models the treatment over time
<b>Time</b>			
total time	min	60	Total time over which the treatment is evaluated
step size	min	0.1	Step size determines time between calculation step of temperature for each mesh element
<b>CONCENTRATION MODEL</b>			
<b>Boundary conditions</b>			
type	-	Neumann	Boundary condition between inside and outside the volume of interest. Neumann represents flux over the boundary
coefficients		$q = 0, g = 0$	Diffusion driven, source and convection neglected
<b>Initial conditions</b>			
breast	#/cm <sup>3</sup>	0	Number of NPs present in breast tissue before treatment = 0
tumor	#/cm <sup>3</sup>	0 or NP $c_i$	Number of NPs present in tumor: at seeds: initial concentration per seed; Outside seed locations: zero
NP $c_i$	#/cm <sup>3</sup>	7.97E+9	Initial concentration of NPs per seed
<b>PDE coefficients</b>			
c: diffusion	cm <sup>2</sup> /s	$D_{breast}$ and $D_{tumor}$	Diffusion coefficient of NPs found in literature: area traveled per second by the NPs through breast or tumor tissue
f: source	#NP/cm <sup>3</sup> s	0	Source of NPs is zero, since no NPs are added after injection
a: convection	#NP/cm <sup>3</sup> s	0	Convection is not taken into account in the model, but it would represent the material spread driven by convection
d: time derivative	-	1	First order time derivative coefficient. Models the treatment over time
<b>Time</b>			
total time	h	24*17	Total time over which the treatment is evaluated
step size	h	1	Step size determines time between calculation step of NP concentration for each mesh element

# B

## Additional Temperature Model Results

### Temperature Distribution After Switching Off AMF

Figure B.1 shows the different intersection profiles of the tumor over time after the AMF is switched off. This figure explains the anomaly in the maximum temperature graphs over time between  $t = 20$  min and 21 min. It is visible that the centre seed first loses its heat to its surrounding, where after the temperature gradient between this seed and its neighbours becomes zero. The temperature cross section shows a parabolic shaped temperature distribution, resulting in a slower temperature decrease for the centre seed from that point on.

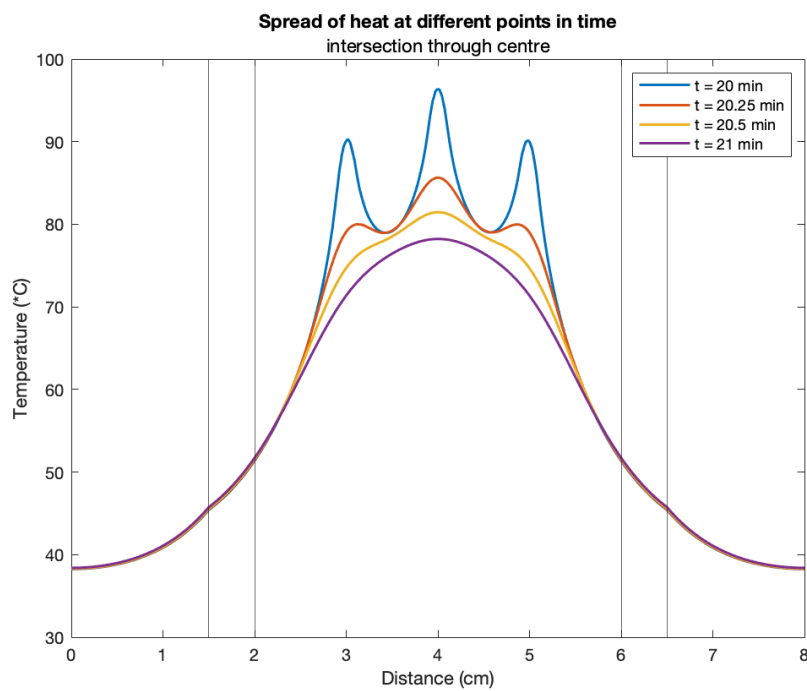


Figure B.1: Intersection through the centre of the tumor. Temperature taken over time right after switching off the AMF, showing that the temperature gradient between the centre seed and its neighbours decreases over time, resulting in a parabolic temperature distribution.

# C

## Concentration Model Results

### Reference nanoparticle concentration results

The results shown in Figure C.1 are the concentration distribution results after 17 days and are used for dose calculations.

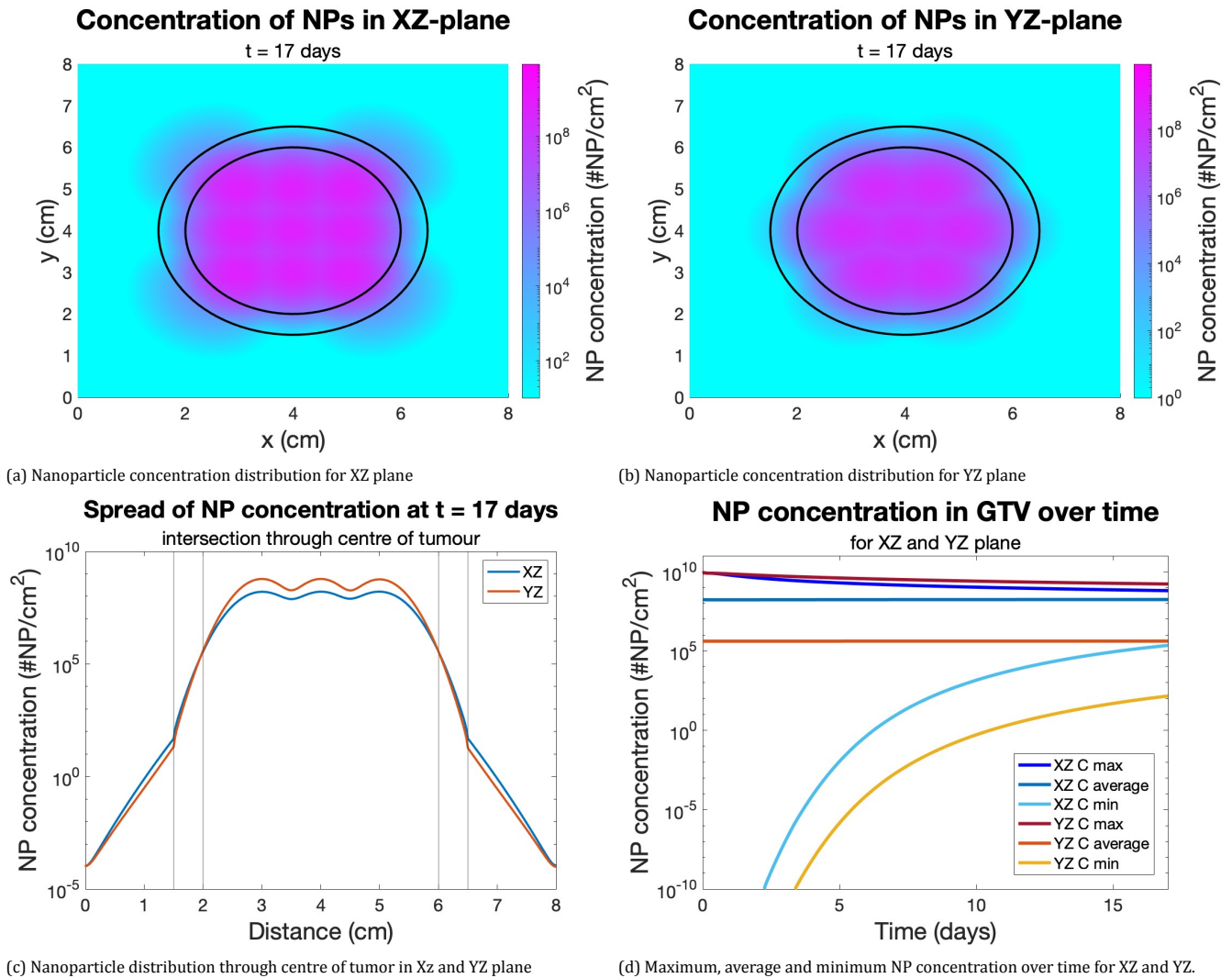


Figure C.1: Nanoparticle concentration results of default settings. Concentration profiles after 17 days (a) in XZ direction and (b) YZ direction. (c) Cumulative dose intersection profile through the centre of the tumor, for the XZ (blue) and YZ (orange) planes. The vertical lines indicate the outer shell of the GTV and PTV. (d) Maximum, minimum and average concentration in the GTV over time for both XZ and YZ planes. The maximum concentration represents the centre seed, the minimum the edge of the GTV furthest away from a seed and the average is taken over the whole GTV.

### Nanoparticle distribution after 60 minutes

Figure C.2b gives the nanoparticle concentration distribution after 60 minutes. Comparing this distribution with the distribution at  $t = 0$  (Figure C.2a), it is assumed that within the first 60 minutes, the nanoparticles have not spread outside the seeds. This means that during the thermal ablation the location of the heated up nanoparticles is assumed to remain the same, simplifying the heat problem.

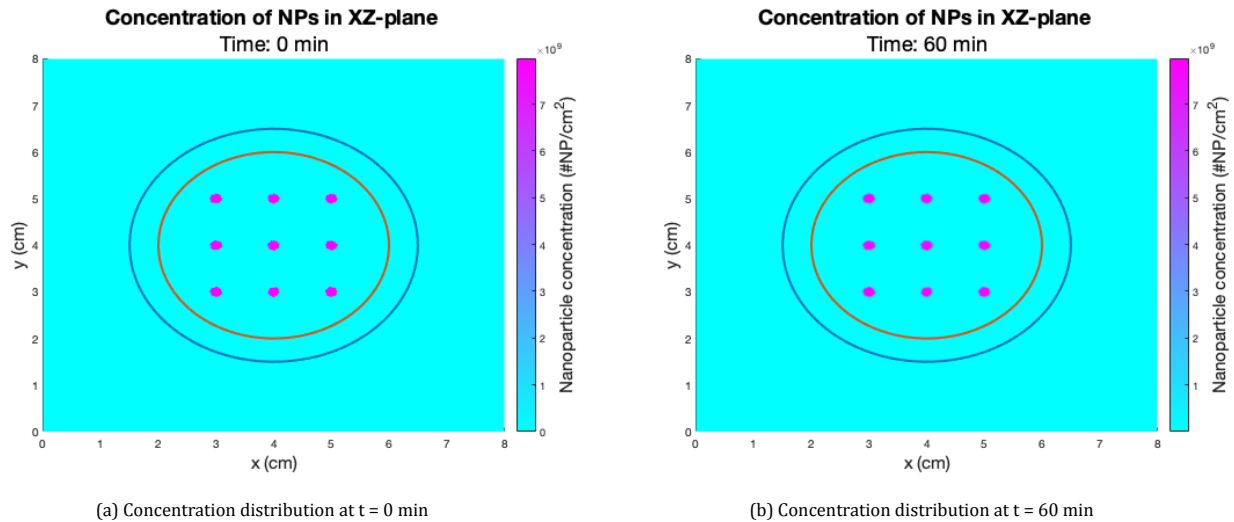


Figure C.2: Nanoparticle concentration distribution after 60 minutes. The NP concentration profile after 60 minutes shows a similar distribution as the profile at  $t = 0$  minutes. This suggests that the NP diffusion can be neglected for the thermal ablation part of the treatment.

### Concentration Results of Sensitivity Analysis using Minima and Maxima of Variables

The effects are evaluated on the travel distance and spread profile of NPs. This is investigated by calculating the maximum, average and minimum concentration in different areas of the geometry, over time. The areas are defined as follows: the GTV core, the PTV surrounding it and in the area of 1 cm surrounding the PTV. Also the distribution profile in 2D and the intersection through the centre of the tumor are generated for the XZ. The relevant results are presented in this section.

Table C.1: Concentration results of sensitivity analysis of parameters evaluated using minimum, default and maximum values. For each parameter the maximum, minimum and average concentrations are found the GTV, PTV area around the GTV and the area of 1 cm outside the PTV.

Variable	Unit	Value	GTV			PTV			PTV + 1 cm		
			$C_{max}$	$C_{min}$	$C_{av}$	$C_{max}$	$C_{min}$	$C_{av}$	$C_{max}$	$C_{min}$	$C_{av}$
<b>Diffusion rate</b>											
$D_{eff}$ normal	cm/s	2.20E-8	6.29E+8	2.40E+5	1.74E+8	5.12E+7	3.53E+2	3.28E+5	9.46E+2	3.10E+3	610.78
$D_{eff}$ min	cm/s	5.70E-9	2.18E+9	6.67E-4	1.71E+8	2.92E+5	1.22E-20	3.48E+2	5.41E-5	1.22E-20	2.38E-7
$D_{eff}$ max	cm/s	1.50E-5	3.56E+7	3.55E+7	3.55E+7	3.55E+7	3.55E+7	3.55E+7	3.55E+7	3.55E+7	3.55E+7
<b>Concentration of NPs</b>											
$c_i$	#NP/cm <sup>2</sup>	7.97E+9	6.35E+8	2.26E+5	1.74E+8	5.05E+7	3.53E-9	3.20E+5	5.09E+4	3.10E-8	6.82E+2
$c_i$ min	#NP/cm <sup>2</sup>	7.97E+7	6.35E+6	2.26E+3	1.74E+6	5.05E+5	3.53E-11	3.20E+3	5.09E+2	3.10E-10	6.82E+0
$c_i$ max	#NP/cm <sup>2</sup>	7.97E+11	6.35E+10	2.26E+7	1.74E+10	5.05E+9	3.53E-7	3.20E+7	5.09E+6	3.10E-6	6.82E+4

### Diffusion coefficient: Non-diffusive nanoparticles

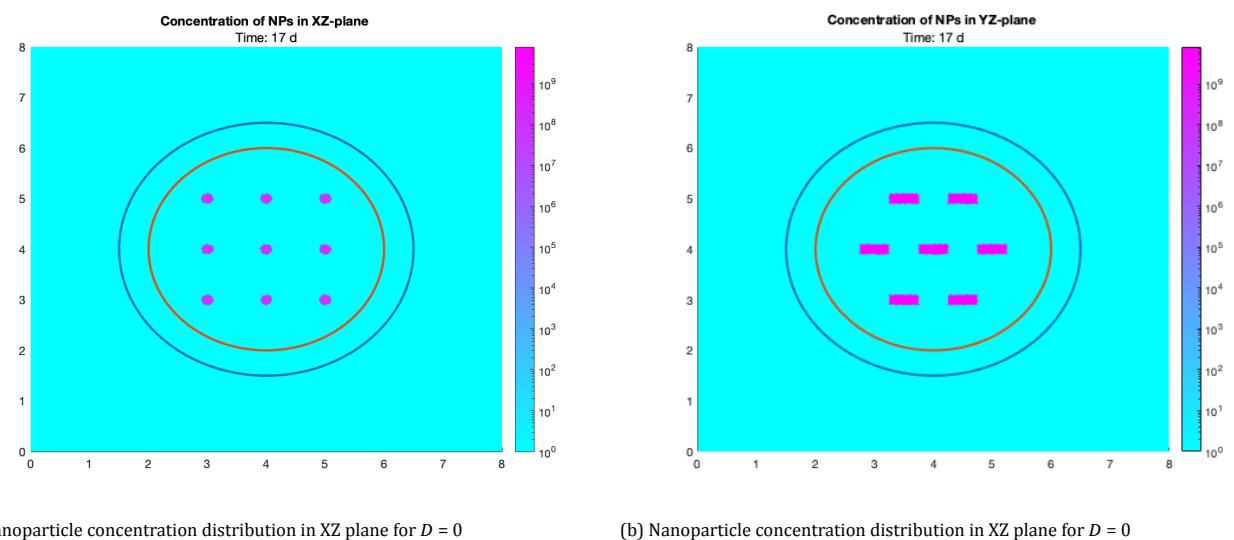


Figure C.3: Concentration and dose distribution profiles resulting from a diffusion coefficient of 0. If the NPs are unable to diffuse through the tumor tissue, the radioactive NPs still deliver radioactive dose to the tissue.